Brigham Young University
BYU ScholarsArchive

Theses and Dissertations

2022-08-09

Multiscale Modeling and Analysis of X-ray Windows, Microcantilevers, and Bioimpedance Microelectrodes

Kyle Grant Larsen
Brigham Young University

Follow this and additional works at: https://scholarsarchive.byu.edu/etd

Part of the Physical Sciences and Mathematics Commons

BYU ScholarsArchive Citation
Larsen, Kyle Grant, "Multiscale Modeling and Analysis of X-ray Windows, Microcantilevers, and Bioimpedance Microelectrodes" (2022). *Theses and Dissertations*. 9675.
https://scholarsarchive.byu.edu/etd/9675

This Dissertation is brought to you for free and open access by BYU ScholarsArchive. It has been accepted for inclusion in Theses and Dissertations by an authorized administrator of BYU ScholarsArchive. For more information, please contact ellen_amatangelo@byu.edu.

Multiscale Modeling and Analysis of X-ray Windows, Microcantilevers, and Bioimpedance Microelectrodes

Kyle Grant Larsen

A dissertation submitted to the faculty of
Brigham Young University
in partial fulfillment of the requirements for the degree of

Doctor of Philosophy

Robert C. Davis, Chair
Richard R. Vanfleet
David D. Allred
Brian D. Jensen
Eric R. Homer

Department of Physics and Astronomy

Brigham Young University

Copyright © 2022 Kyle Grant Larsen

All Rights Reserved

ABSTRACT

Multiscale Modeling and Analysis of X-ray Windows, Microcantilevers, and Bioimpedance Microelectrodes

Kyle Grant Larsen
Department of Physics and Astronomy, BYU
Doctor of Philosophy

X-ray detector windows must be thin enough to transmit sufficient low-energy x-rays, yet strong enough to withstand up to an atmosphere of differential pressure. Traditional low-energy x-ray windows consist of a support layer and pressure membrane spanning that support. Numerical modeling of several x-ray windows was used to show that both low- and high-energy x-ray transmission can be improved by adding a secondary support structure. The specific x-ray window models developed in this work may serve as a foundation for improving commercial windows, especially those geared toward low-energy transmission.

For local mechanical film testing, microcantilevers were cut in suspended many-layer graphene using a focused ion beam. Multipoint force-deflection mapping with an atomic force microscope was used to record the compliance of the cantilevers. These data were used to estimate the elastic modulus of the film by fitting the compliance at multiple locations along the cantilever to a fixed-free Euler-Bernoulli beam model. The breaking strength of the film was also found by deflecting cantilevers until fracture. The average modulus and strength of the many-layer graphene films are 300 GPa and 12 GPa, respectively. The multipoint force-deflection method is well suited to analyze films that are heterogeneous in thickness or wrinkled.

Bioimpedance can be measured by applying a known current to the tissue through two (current carrying) electrodes and recording the resulting voltage on two different (pickup) electrodes. A wrist-based wearable bioimpedance device can measure heart rate by detecting the minute impedance changes caused by the modulation of blood volume in the radial artery. Using finite element analysis, I modeled how electrode position affects sensitivity to pulsatile changes. The highest sensitivity was found to occur when the pickup electrodes were centered over the artery.

In this work, we used microfabricated carbon infiltrated-carbon nanotube electrodes to measure the change in skin-electrode impedance for dry electrodes, and identical electrodes with a wet electrolyte, on five human subjects in the range of 1 kHz to 100 kHz. We found that the acclimated skin-electrode impedance of the dry electrodes approached that of the wet electrodes, especially for electrodes with larger areas. We also found that the acclimation time does not appear to depend on electrode area or frequency. The skin-electrode impedance after acclimation does depend on electrode area and frequency, decreasing with both.

Keywords: x-ray window, hierarchical structure, material properties, Young's modulus, tensile strength, bioimpedance, pulsatile sensitivity, skin-electrode impedance, electrode acclimation, skin-electrode interface

ACKNOWLEDGMENTS

This dissertation is seven years in the making. Seven years of learning, of teaching, of investigating, of growing. During this tour of study, I have been directly taught, trained, and tutored by over thirty students, faculty, and staff. I cannot thank every *one* of you, so I will thank *all* of you: thank you, gracias, obrigado, merci beaucoup! Sincerely, from the bottom of my heart, thank you for these last seven years which have resulted in what is best described as the dendritic expansion of my mind into the topics of this dissertation and many more beyond. I would, of course, be remiss not to give a special acknowledgment of thanks to Dr. Rob Davis for his continued support, encouragement, advisement, and mentoring.

Of all the people that deserved to be acknowledged for their effort in helping me produce this work, my wife and life partner ranks first and foremost. She has been a constant source of support, motivation, encouragement, and reprieve. Thank you, Bethany! We are finally more than halfway there!

TABLE OF CONTENTS

LIST OF FIGURES

LIST OF TABLES

Chapter 1: Introduction

1.1 Foreword

This dissertation contains my contribution to two broadly separate fields of physics, connected mainly by the methods I employed in solving my disparate research problems. The first prong of my dissertation bident focuses on the development of improved x-ray detector windows. This led to the modeling and optimization of x-ray detector windows with hierarchical support structures, to the exploration of novel x-ray window materials (including many-layer graphene), and to a new method for characterizing suspended thin films with non-uniformities in thickness. The second prong of my dissertation had me take a leap into medical device physics, particularly bioimpedance for non-invasive health monitoring. As part of a multi-disciplinary team, I used computational modeling to determine sensitivity tradeoffs in electrode placement for bioimpedance plethysmography. I also designed an analog front-end to a commercial impedance analyzer that facilitated a safe human subjects study – in addition to actually writing the proposal to the institutional review board (IRB) to obtain permission to perform the study. The two prongs that make up this dissertation are related mainly by the multiscale nature of the modeling and analysis that I performed, with length scales ranging from the nanometer to the centimeter.

Perhaps the ideal dissertation – and definitely the traditional dissertation – takes one research question and dives down, exploring deeply rather than laterally. Due to funding constraints, I was not able to dive as deeply as might have been expected. Indeed, the funding for the research in Chapter 2 was cut before we could fabricate any x-ray windows with hierarchical support structures, and I took over the project that would ultimately become Chapter 3 *after* funding had already dried up. That is not to say that I was not able to make significant contributions. This dissertation is almost two dissertations in one, with Chapters 2 and 3 comprising one section and Chapters 4 and 5 comprising the other. Without funding difficulties, I would not have had the opportunity to learn how to write a funding proposal. (A proposal that was successfully funded, with several follow-on grants, and that has supported over a dozen students during the past four years.) After all is said and done, I am grateful to have been able to contribute in so many different ways and for everything I learned along the often meandering path to completing this dissertation.

1.2 Background and Motivation

Each chapter of this dissertation (except Chapter 4) is a research paper that has either been submitted or will be submitted shortly. As such, each stands independent, with its own introduction, background, and motivation. Here I will provide additional background and insight into motivation, along with a description of any threads that link the various chapters.

1.2.1 X-ray detector windows and many-layer graphene

Moxtek, Inc. (Orem, UT, USA) originally funded this research with the goal of improving the x-ray transmission of their x-ray detector windows. My original research question was, "How can low-energy x-ray transmission be improved by using hierarchical support structures?" That later transformed into an investigation of new high strength materials that would lend themselves well to x-ray detector window applications. We were particularly motivated to understand the material properties of many-layer graphene, which led to the improvement of a cantilever bending method for characterizing those properties.

1.2.1.1 X-ray detector windows

An x-ray detector window is a pressure barrier consisting of a membrane and support structure affixed between an x-ray detector and the sampling environment. It protects the detector, which is kept cold and under vacuum, from ice buildup, foreign contaminants, and extraneous light. The window must be strong enough to withstand 14.7 psi (1 atm) of differential pressure but thin enough to allow adequate transmission of x-rays. An example of this setup is energy dispersive x-ray spectroscopy (EDS), where the window and the detector form a device used for elemental analysis with an electron microscope[1]. The primary electron beam of the microscope hits the target, ejecting electrons from the inner orbitals of the sample atoms. Higher shell electrons emit x-rays as they fall down to a lower, vacant shell. The x-rays are characteristic of the atom from which they were emitted, ranging in energy from 54 eV (see lithium in Table 1-1) up to several tens of keV [2]. These x-rays are captured by a detector inserted into the electron microscope sample chamber.

Table 1-1
A listing of the characteristic x-ray energies of lithium through silicon[2].

Z	Element	Kα (eV)	Kβ (eV)
3	Li	54.3	
4	Be	108.5	
5	B	183.3	
6	C	277.0	
7	N	392.4	
8	O	524.9	
9	F	676.8	
10	Ne	848.6	
11	Na	1,040.98	1,071.1
12	Mg	1,253.60	1,302.2
13	Al	1,486.70	1,557.5
14	Si	1,739.98	1,835.9

By analyzing the energy of the x-rays emitted from a sample with EDS, it is possible to identify elements in the sample. The innermost electron orbital or shell is the K shell, then L, M, etc. (see Fig. 1-1). An electron falls from a source shell to an evacuated destination shell. It is convention when naming electron transitions to follow the scheme *[destination][source]*, such as

Kα. This indicates an electron that fell into the K shell from the next highest orbital (L to K). Source orbitals are labeled by Greek letters starting with α. As another example, the Lβ transition occurs as an electron falls from N to L. Since N is two orbitals higher than L it is labeled with β. These emissions have energies that are specific to each element. Table 1-1 lists the Kα and Kβ energies for lithium through silicon. It is important to note that current x-ray windows lack adequate transmission for the Kα emissions of lithium, beryllium, and boron, which range from 54 eV to 183 eV.

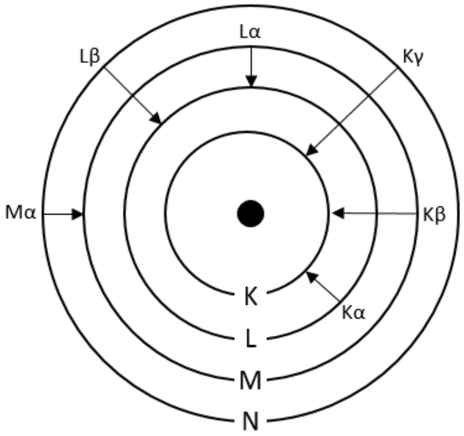

Fig. 1-1. Electron transition diagram.

In this work, I model x-ray windows with a primary support layer, secondary support layer, and a pressure membrane. The primary and secondary support layers form a hierarchical structure that should both increase low-energy and high-energy x-ray transmission. Improved low-energy transmission would make a hierarchical window useful for EDS of low-atomic number elements. Hierarchical x-ray detector windows are discussed in Chapter 2.

The material that forms the pressure barrier of the x-ray window was also a target of investigation. We looked at the performance of both polymer and silicon nitride windows. Carbon-based windows offer an attractive alternative to silicon nitride because carbon has a lower atomic number than both silicon and nitrogen. Graphene is an extremely strong material[3] that can be thin and span large distances[4]. We were able to fabricate suspended many-layer graphene films, but we had no method by which to effectively characterize their mechanical properties.

1.2.1.2 Characterization of many-layer graphene

Graphene is a single layer of sp^2 bonded carbon. Monolayer graphene has a tensile strength of up to 130 GPa[3], but it is much too thin to span the distances needed for an x-ray detector window. Stacking monolayers of graphene creates a new class of multilayer graphene. This is done by modifying the growth process rather than with mechanical exfoliation or cleavage[5]. With many stacked layers, the film begins to resemble graphite. However, it is still beneficial to refer to these films as many-layer graphene due to the manner in which these films are grown (being similar to that of monolayer graphene). Many-layer graphene is grown in a CVD process[4], [6]. The tensile properties of CVD many-layer graphene have yet to be reported in the literature. Before developing the multipoint force-deflection method, we first attempted to measure the tensile properties of many-layer graphene using a bulge test.

The bulge test is a measurement of the deflection of a thin film under various pressure differentials[7]. Bulge testing was introduced in 1959 by J. W. Beams as a way to determine properties of thin films[8]. The material's response under different pressures is controlled by its materials properties. As such, the bulge test can be used to determine film modulus, yield strength, fracture strength, and residual stress.

Analytical models exist for spherical, square, and rectangular membranes. These models are valid for linear elastic materials. It is assumed that the thickness of the film is much less than its radius, as bending stiffness is not taken into account. These models cannot account for slack or wrinkles in films, and as such tested films must have a residual tensile stress. It is this caveat that ultimately led us to seek a different method for determining the strength and modulus of many-layer graphene. Bulge testing is still useful in determining the pressure at which the film will burst, especially since the ultimate application of these films would be as a pressure barrier in x-ray detector windows.

Certain materials have an intrinsic compressive stress, meaning that slack is introduced to the film upon release from the substrate. This slack means the bulge test models do not describe the film. As such, another method for determining the strength of the material is required. By cutting or etching rectangular cantilevers in thin films (see Fig. 1-2) it is possible to determine Young's modulus and fracture strength [9]. A load is applied at several points along the cantilever with an AFM and multiple force-deflection curves are acquired. The slopes of these curves are fit to a fixed-free cantilever beam model and used to determine the properties of the material. Multipoint force-deflection is discussed further in Chapter 3.

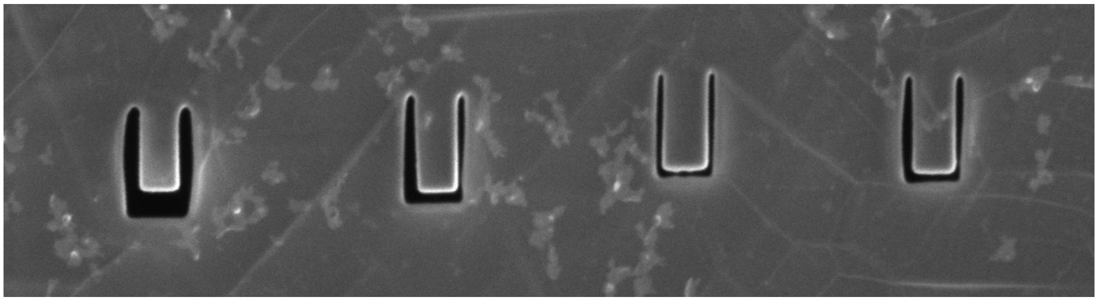

Fig. 1-2. Four cantilevers cut in a 150 nm many-layer graphene film. The cantilevers measure about 1 μm by 0.5 μm. These cantilevers were cut with a focused ion beam in a scanning electron microscope.

1.2.2 Bioimpedance for health monitoring

Wearable fitness trackers have increased in popularity over the past several years[10]. Bioimpedance is the electrical impedance of biological tissue, typically measured with either a two-electrode or four-electrode configuration. Bioimpedance is not yet a ubiquitous feature of fitness trackers, but it does offer the ability to measure many biological and physiological parameters. Bioimpedance can be used for detecting fluid overload[11], cancer[12]–[14], cardiac pulse[15], and blood glucose[16]. Tula Health (Farmington, UT, USA) has funded research at BYU to (in part) investigate the possibility of using bioimpedance in a wearable, non-invasive glucose monitor.

Bioimpedance has been used to non-invasively measure changes in blood glucose[16]–[19]. The system developed by Caduff *et al*. uses two electrodes in a fringing field configuration. This is a capacitive measurement where the capacitive fringe fields penetrate the skin and can detect changes in glucose in the interstitial fluid of the body. A more rapid and sensitive response to changes in glucose is desirable, since glucose in interstitial fluid lags behind glucose in the blood by up to 20 minutes. A bioimpedance system that can measure blood may be more sensitive to changes in glucose. We made no attempt in the work described here to measure glucose, but instead we lay the foundation for a future bioimpedance measurement system.

Bioimpedance spectroscopy and bioimpedance plethysmography are two aspects of a future bioimpedance system that we hope will enable non-invasive glucose measurements. Bioimpedance spectroscopy involves measuring the impedance of tissue at multiple frequencies. Bioimpedance plethysmography is a technique where changes in bioimpedance correspond to changes in some internal volume. Bioimpedance plethysmography can be used to determine cardiac pulse rate and respiration rate. It can also be used, in combination with bioimpedance spectroscopy, to non-invasively measure the impedance spectrum of blood.

A wearable bioimpedance system would require stable electrodes, which precludes using wet electrolytes to reduce skin-electrode impedance. When dry electrodes (electrodes lacking a wet electrolyte) are placed on the skin, the skin-electrode impedance will be very high before slowly dropping. This period of change is termed the acclimation period and its length may depend on electrode area and the measurement frequency. Understanding this acclimation period and the skin-electrode impedance after acclimation will help in designing future wearable bioimpedance devices. Modeling of electrode placement is discussed in Chapter 4 and skin-electrode acclimation is covered in Chapter 5.

1.3 Chapter Overviews

Chapter 2 is an article that will be submitted shortly. It focuses on modeling hierarchical x-ray detector windows. This article concludes that hierarchical support structures can be used to increase both the low-energy and high-energy transmission of x-ray detector windows. Hierarchical support structures are more useful for polymer-based windows and less useful for silicon nitride-based windows that can already be made ultra-thin. All the modeling, programming, and writing was performed by myself, with feedback, direction, and editing provided by the listed co-authors. I created all the figures, except Fig. 2-1a, which was produced by Bethany Larsen.

Chapter 3 is a submitted article (currently under peer review) about characterizing the mechanical properties of heterogeneous thin films using multipoint force-deflection mapping of microcantilevers. For films that have non-uniformities in thickness, or are wrinkled, a local characterization technique is needed. This chapter describes a method to measure local properties by cutting microcantilevers with a focused ion beam in a suspended film, and then using an atomic force microscope to map force-deflection curves at multiple points. These data are then fit to a cantilever model from which modulus is extracted. Film strength is found by deflecting the cantilever until fracture. All samples were fabricated by Stefan Lehnardt and Bryce Anderson. Original efforts in cantilever fabrication and testing were performed by Joseph Rowley. The AFM force-volume data was captured by Stefan, Bryce, and myself. I performed all the data analysis, programming, and modeling, with feedback from the other co-authors. I drafted the manuscript, with feedback and editing by Dr. Vanfleet and Dr. Davis.

Chapter 4 details an investigation into electrode placement for bioelectrical impedance plethysmography. Using this technique it is possible to measure the cardiac pulse of a human subject. This chapter focuses on a simplified model of the human wrist and how electrode placement affects the sensitivity of the impedance measurement. We make predictions that were tested by a later human subjects study. Unfortunately, the data in that study were not of sufficient quality to either confirm or falsify the model predictions. The modeling and programming work was performed by myself, with input from the interdisciplinary team funded by Tula Health. I wrote this chapter with feedback and editing help from Dr. Davis.

Chapter 5 is a soon-to-be submitted article investigating the time variation of the skin-electrode skin-electrode impedance of carbon nanotube-based composite electrodes. A human subjects study (approved by BYU's Institutional Review Board) found that the skin-electrode impedance dropped significantly over the first 15 to 30 minutes, after which the change gradually slowed. This acclimation period is most likely due to a change in skin/interface hydration near the electrodes. This work was an equal collaboration with Diego Leon. Diego and I, with feedback from Dr. Jensen and Dr. Davis (and others in the Tula research group), planned the human subjects study. I spearheaded and authored the majority of the proposal to the IRB committee for approval to do human subjects research. I designed and assembled the multiplexer/safety board that facilitated this work. Diego handled recruitment and execution of the experiment, with help from others (especially Nick Allen). Diego and I collaborated on the initial analysis of the data, which is available in his thesis[20]. Diego wrote the initial draft of the paper that would later become Chapter 5 after a re-write by myself, with editing and feedback from Dr. Jensen and Dr. Davis. Several of the figures in this paper were created by Diego.

Chapter 6 contains high-level conclusions and a discussion of possible future work. Detailed conclusions are contained in each chapter.

Chapter 2: Numerical Optimization of X-ray Detector Windows

Authors: Kyle G. Larsen, Joseph T. Rowley, Jonathan Abbott, Sterling Cornaby, Richard R. Vanfleet, and Robert C. Davis

2.1 Abstract

X-ray detector windows are used in applications such as energy dispersive x-ray spectroscopy, where the window serves as a barrier between the x-ray detector environment and the sampling environment. The window must be thin enough to transmit sufficient low-energy x-rays, yet strong enough to withstand up to an atmosphere of differential pressure. Traditional low-energy x-ray windows consist of a support layer and pressure membrane spanning that support. We perform numerical modeling of several x-ray windows to show that both low- and high-energy x-ray transmission can be improved by adding a secondary support structure. We optimize these windows over one or more parameters and compare the results against similar commercial windows. We use finite element analysis to model the x-ray windows under a typical applied pressure load and show that the resulting stress does not exceed the ultimate strength or yield strength of the respective materials. We published the x-ray transmission modeling and optimization software used in this analysis as open source software[21]. We have shown that the addition of a secondary support structure improves both low- and high-energy x-ray transmission. The specific x-ray window models developed in this work may serve as a foundation for improving commercial windows, especially those geared toward low-energy transmission.

2.2 Introduction

Energy-dispersive x-ray spectroscopy is often used for elemental analysis of samples in an electron microscope, where an x-ray detector window separates the x-ray detector environment from the sample environment. Some low atomic number elements have characteristic emissions that are significantly attenuated by the x-ray window before reaching the detector. Improving the soft, or low-energy, x-ray transmission of x-ray detector windows will both decrease the required sampling time and increase the range of materials that can be sampled. An x-ray detector window is a pressure barrier that protects the detector, which is often kept cold and under vacuum, from foreign contaminants and extraneous light. The window must be strong enough to withstand an atmosphere of differential pressure but thin enough to allow adequate transmission of x-rays. The window itself is typically mounted in an external support frame that can be attached to an x-ray detector. Some x-ray windows have no additional support, consisting of a relatively thick membrane spanning the external support frame. Other x-ray windows consist of a membrane on a support structure. In this work, we focus on support structures made from parallel silicon ribs; however, the techniques and results are generally applicable to other support types. Support structures tend to block all but the highest energy x-rays. However, windows with a support structure can have thinner membranes because a membrane's thickness (for a constant applied pressure) depends on the distance it must span. This means that windows with a support structure tend to have a lower overall transmission (due to the opaque support structure) but a higher low-energy x-ray transmission (due to the thinner membrane). We are interested in maximizing the open area between the primary support structure ribs and minimizing the membrane thickness; however, these two parameters are in direct competition because the membrane thickness must increase if the support spacing increases. The open area describes the area of the window not taken up by the support structure. The open area of the primary support structure can be increased by increasing the primary support spacing and adding a secondary support structure (see Fig. 2-1a). The thinner and more closely spaced secondary support structure can span the primary support and in turn support an even thinner pressure membrane. We call x-ray windows with multiple support structure geometries hierarchical windows.

We take a multi-step approach to modeling x-ray detector windows. The first steps involve the mechanical modeling of the window. For the optimization problem, this is performed analytically; however, certain configurations are checked with finite element analysis. The analytical mechanical model consists of a fixed-fixed Euler-Bernoulli beam model (for the supports) and a separate membrane model. The final steps involve estimating the transmission through the supports and membrane. This is done using x-ray transmission information from the Center for X-ray Optics (CXRO)[22], [23]. The optimization routine can select for the highest transmission at one or more arbitrary energies.

In this study, we analyze traditional and hierarchical x-ray detector windows. A hierarchical structure may alleviate the competition between open area and membrane thickness by spacing out the primary support structure and adding a secondary support structure that is thinner and more closely spaced than the primary. Focusing on ribbed support structures, we modeled both traditional and hierarchical x-ray detector windows in order to find optimal primary and secondary support spacings and the associated optimal membrane thickness. We modeled x-ray windows with silicon support structures and polymer or silicon nitride (Si–N) pressure membranes. We found that low-energy x-ray transmission can be improved by using a hierarchical support structure, which allows for the membrane to be made thinner. High-energy x-ray transmission is also improved, because of the larger open area in the primary support structure. However, using a hierarchical support structure does not have as significant an impact

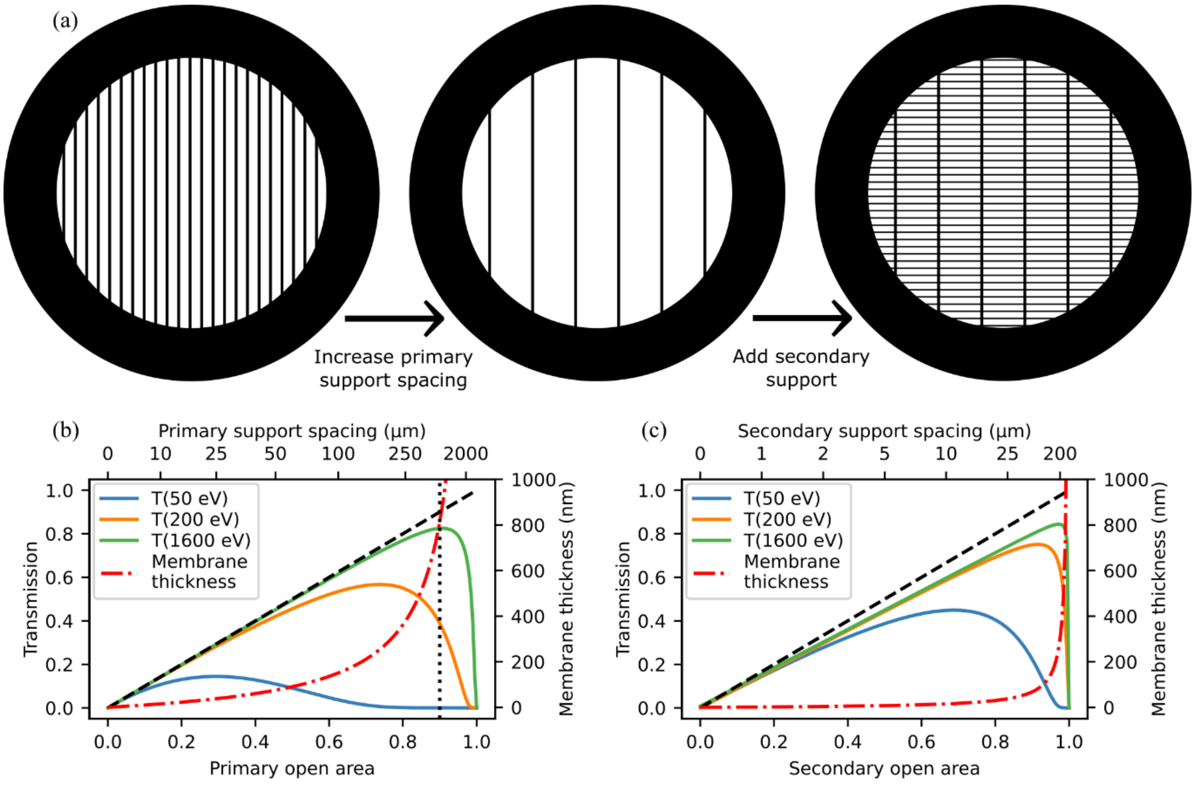

Fig. 2-1. X-ray window schematic representation and effects of varying open area. (a) The primary open area increases as the primary support (vertical lines) spacing increases. A secondary support (horizontal lines) can then be added to make a hierarchical support structure. (b) Shown here is the estimated transmission at specific energies through an x-ray window with only a primary silicon support and polymer membrane. As the primary open area increases, so too does the membrane thickness required to span the support structure. A larger open area (i.e. a thicker membrane) means fewer x-rays are blocked by the support structure, but also means lower-energy x-rays are attenuated in the membrane. The dotted vertical line represents the configuration used in (c). (c) The primary open area of the model in (b) was fixed at 90% and a secondary support was added. Because the secondary support spacing is smaller than the primary support spacing, the membrane thickness is also smaller, thereby increasing low-energy x-ray transmission. The dashed black line along $y=x$ in (b) and (c) indicates the maximum transmission due to open area for all but the highest-energy x-rays. The horizontal axis in (b) and (c) is labeled with both open area (bottom) and the equivalent support spacing (top), assuming the primary support width is 60 µm and the secondary support width is 5 µm.

with Si–N membranes as it does for polymer membranes, because ultra-thin Si–N can already span large distances. The hierarchical polymer window had a 5x improvement in transmission at 54 eV over the traditional polymer window, while in the case of Si–N that improvement was 30%. The hierarchical Si–N window did not benefit as much as its polymer counterpart because the optimization was limited by a constraint based on an estimate of the minimum manufacturable thickness of a gas-tight Si–N membrane[24]–[27]. These optimization results do not dictate a final x-ray window design, but rather should guide further design. The optimization tool we developed for this work is available as open source software[21]. This work demonstrates through computational modeling that improvements can be made to polymer-based x-ray detector windows by using a hierarchical support structure.

2.3 Traditional Supported X-ray Window Design

X-ray detector windows come in various shapes and sizes. At a minimum, the window must consist of a mounting frame and a pressure barrier, such as the beryllium windows offered by Moxtek (Orem, UT, USA) and Helmut Fischer (Sindelfingen, Germany) or the boron carbide windows offered by Amptek (Bedford, MA, USA). In order to decrease film thickness while maintaining a large window area, manufacturers have created windows with a support layer. Several support geometries exist including parallel ribs[28], [29], square grids[24], and hexagonal grids[30]. We have chosen to focus on modeling and optimizing windows with a ribbed support structure, but the methods described here are applicable to any type of support structure. The hierarchical windows that we modeled include a secondary support structure made from parallel ribs that are orthogonal to the primary support ribs (see Fig. 2-1a).

Fig. 2-1b shows how the transmission at three different energies (50 eV, 200 eV, and 1600 eV) for a window without a secondary support changes based on open. The transmission curves are limited on the left (low open area) by the thick support structure, hence the black dashed line. On the right (high open area), transmission is instead limited by the membrane thickness. In order to improve low-energy x-ray window transmission with a traditional window design, it is necessary to sacrifice overall efficiency. The maximum transmission at 50 eV for the window in Fig. 2-1b occurs at about 30% open area, but that also means the maximum transmission is 30% for all but the highest energy x-rays.

Current polymer-based x-ray detector windows have low transmission for energies below about 200 eV, which precludes efficient detection of boron, beryllium, and lithium. Unsupported beryllium windows perform even worse for low-energy x-ray detection. Improvements in low-energy transmission of polymer-based windows would enable the detection of lithium and increase the efficiency of detecting beryllium and boron.

Hierarchical support structures have been used in the past to improve the performance of x-ray detector windows[24]. Törmä *et al.* used a larger backside grid to effectively tile their ultra-thin silicon nitride x-ray window in order to increase the window area from 31 mm^2 to 760 mm^2. In this work we use hierarchical support structures to improve low-energy x-ray transmission instead of increasing the window area.

2.4 Hierarchical X-ray Window Design

The geometry of a hierarchical window is shown in Fig. 2-1a. The design of the primary support structure is reduced to several variables: rib length (L_p), rib width (w_p), rib thickness (t_p), and rib-to-rib spacing (d_p). The secondary support structure is described likewise: rib length (L_s), rib width (w_s), rib thickness (t_s), and rib-to-rib spacing (d_s). The pressure membrane is described by its thickness (t_m) and the distance it must span (w_m), which is either the primary rib-to-rib spacing ($w_m = d_p$), or for hierarchical support structures, the secondary rib-to-rib spacing ($w_m = d_s$). These parameters are described in Table 2-1. In addition to its geometry, each layer can be constructed from a different material. Fig. 2-1c shows how the transmission (for a window with a secondary support) changes based on secondary open area when the primary open area is fixed at 90%. The membrane is much thinner than the membrane in Fig. 2-1b, which leads to increased transmission, especially for lower-energy x-rays.

In this work, we will optimize four different x-ray window models: traditional (two-layer) and hierarchical (three-layer) for both a polymer and silicon nitride. These windows will have silicon supports (both primary and secondary). The modeled and optimized x-ray detector windows will be compared with models based on the polymer AP3[31] window from Moxtek (Orem, UT, USA) and the silicon nitride C2[32] window from Amptek (Bedford, MA, USA). The AP3 window is modeled with a support structure consisting of a series of parallel ribs etched into a 375 μm silicon wafer. The window has an open area of 77% and a window area of 82 mm^2. The membrane is a film stack consisting of a 300 nm thick high-strength polymer, 30 nm of aluminum for charge dissipation and a light barrier, and a gas and corrosion barrier modeled as 20 nm of boron. The C2 window is modeled with a support structure made from an 8 μm thick polysilicon grid with an open area of 80% and a window area of 31 mm^2[24]. The C2 membrane is a film stack consisting of 40 nm of low-stress silicon nitride and 30 nm of aluminum for charge dissipation. No gas barrier is needed because silicon nitride can be made gas-tight [24], [33], [34].

We did not attempt to fabricate any of the hierarchical window models discussed in this work. However, we did consider manufacturability when selecting values for the parameters in Table 2-1 as mentioned in the "Considerations" column. In particular, lower limits were set for the membrane thickness (150 nm for polymer and 20 nm for Si–N) and the support width (5 μm). The secondary support thickness was also fixed to the device layer thickness (45 μm) on a specific silicon-on-insulator (SOI) wafer, in anticipation of a potential fabrication method.

We have simplified the definition of open area by assuming all x-rays are normally incident and collimated, which allows us to ignore any angle dependence. However, open area is angle-dependent because the support structure is more likely to block x-rays with a non-normal incident vector. This is especially true for ribbed support structures with closely-spaced and high aspect ratio ribs. One benefit of hierarchical support structures is that the distance between the primary support members can be increased, thereby increasing the acceptance angle of the window.

Table 2-1
X-ray Window Transmission Optimization Parameters

Window type	Layer	Parameter	Free/fixed	Considerations
Traditional supported (two-layer) x-ray window	Primary support	L_p, Length	Fixed	Set by support frame inner diameter
		w_p,Width	Fixed	Same as AP3
		d_p, Spacing	Free	
		t_p, Thickness	Fixed	Set by wafer thickness
	Membrane	w_m,Width	Fixed	Same as primary support spacing
		t_m, Thickness	Fixed	Minimum thickness to span width
Hierarchical (three-layer) x-ray window	Primary support	L_p, Length	Fixed	Set by support frame inner diameter
		w_p,Width	Fixed	Same as AP3
		d_p, Spacing	Free	
		t_p, Thickness	Fixed	Set by wafer thickness
	Secondary support	L_s, Length	Fixed	Same as primary support spacing
		w_s,Width	Free	
		d_s, Spacing	Free	
		t_s, Thickness	Fixed	Set by SOI wafer device layer thickness
	Membrane	w_m,Width	Fixed	Same as secondary support spacing
		t_m, Thickness	Fixed	Minimum thickness to span width

2.5 Mechanical Modeling Methods

2.5.1 Analytical model

The hierarchical x-ray detector window was mechanically modeled in three parts: the pressure membrane, the secondary support structure, and the primary support structure. The pressure membrane was assumed to span the secondary support structure, which in turn spanned the primary support structure. The pressure membrane's width is the same as the secondary support spacing, and its length is the same as the secondary support length. Because the secondary support structure's length is always at least six times longer than its width, the following simplified membrane stress equation can be used[35, p. 84]:

$$\sigma_{mem} = \sqrt[3]{\frac{p^2 a^2 E}{6t_m^2(1-\nu^2)}}, \tag{2.1}$$

where E is Young's modulus, p is pressure, a is the membrane half-width ($a = w_m/2$), t_m is the membrane thickness, and ν is the Poisson ratio of the membrane. Although the x-ray windows modeled in this work have membranes consisting of multiple layers (e.g. gas barrier layer, light blocking layer, etc.), these other layers are ignored in the strength model. They are, however, considered in the x-ray transmission model.

The beams for the secondary and primary support structures were both modeled as fixed-fixed Euler beams. The maximum stress was determined by

$$\sigma_{beam} = -\frac{Mc}{I} = \frac{pL^2}{2wt^2}, \tag{2.2}$$

where L is the length of the beam, w is the width of the beam, and t is the beam thickness[36]. The maximum stress occurs at the top and bottom surface of the beam at the fixed ends where the moment is $M = pL^2/12$. The distance from the neutral axis to the top surface is $c = t/2$. The second moment of area for a beam with rectangular cross-section is $I = wt^3/12$.

The stress equation for a membrane can be rearranged to solve for the thickness of a membrane spanning a given distance and able withstand a certain pressure:

$$t_m = \sqrt{\frac{p^2 a^2 E}{6\sigma_{mem}^3(1-\nu^2)}} = pa\beta \tag{2.3}$$

where $\beta = \sqrt{E/6\sigma_{mem}^3(1-\nu^2)}$, which depends only on the material properties of the membrane. Lower β means a thinner membrane can span the same distance for a given pressure. The values of β for several materials are listed in Table 2-2. Equation (2.3) will be used during the optimization to find the minimum required thickness of the pressure barrier in order to span the support spacing.

Table 2-2
Common X-ray Window Materials

Material	E (GPa)	σ (GPa)	ν	β (GPa^{-1})
Aluminum	25	0.19	0.30	25.8
High strength polymer	9.0	0.20	0.22	14.0
Beryllium	320	1.0	0.10	7.34
Polysilicon	158	2.0	0.22	1.86
Boron	400	3.6	0.17	1.21
Silicon nitride	290	4.0	0.25	0.90
Silicon	150	7.0	0.17	0.27
Boron nitride	865	70	0.19	0.02
Graphene	1000	100	0.15	0.01

2.5.2 Finite element model

Finite element analysis with COMSOL Multiphysics 5.5 was used to model the stress and deflection at 1.2 atm for specific window configurations. The finite element model contains beams with lengths on the order of 10 mm and membranes that are as thin as 20 nm. COMSOL's membrane interface was used to avoid the challenge of meshing extremely thin volumes. Four different x-ray windows were modeled: traditional (two-layer) and hierarchical (three-layer) with either a polymer or silicon nitride membrane. Only a small section of each window was modeled, in order to speed up the simulation time. For the two-layer windows, a single membrane section bound by two primary supports was modeled. For the three-layer windows, the same section with the additional secondary supports was modeled. Each window had a pressure of 1.2 atm applied to the membrane. The stress was calculated and compared with the yield strength (for the polymer) and the ultimate tensile strength (for silicon nitride).

2.6 X-ray Transmission Modeling Methods

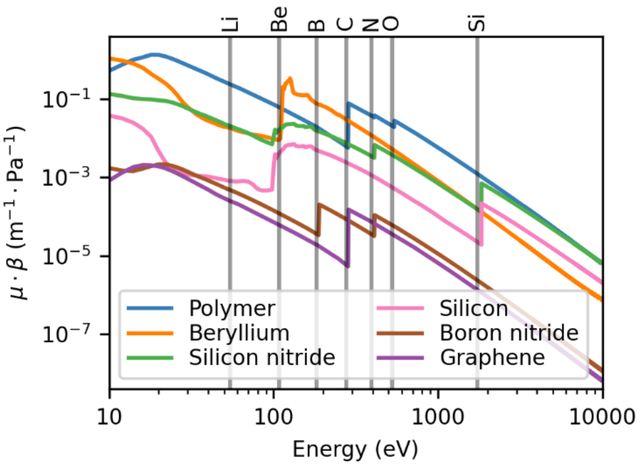

Fig. 2-2. Comparison of some potential x-ray window membrane materials from Table 2-1. The product $\mu \cdot \beta$ is the material-dependent portion of the transmission equation, $T = \exp(-\mu t) = \exp(-\mu p a \beta)$. A lower value means higher transmission for a membrane spanning the distance a with an applied pressure p. The Kα emission energies for several elements are indicated with vertical lines. Other important factors the $\mu \cdot \beta$ product does not take into account include manufacturing variability (especially anything that affects stress) and gas permeability.

X-ray transmission data for a certain thickness t of each material in the window (including the gas barrier and light blocking layers membrane layers) were taken from Lawrence Berkeley National Laboratory's Center for X-ray Optics (CXRO). These data, which consist of experimental and theoretical results, were referenced to build up the transmission model. X-ray transmission decreases exponentially as a function of material thickness, according to $T_1 = e^{-\mu t_1}$, where μ is the attenuation coefficient and t_1 is the thickness of the material[37]. The x-ray transmission for a material with thickness t_1 can be used to determine the transmission for the same material with a different thickness t_2, such that $T_2 = T_1^{t_2/t_1}$. Using (2.3), the maximum transmission for a membrane spanning $2a$ under pressure p is $T = e^{-\mu\beta p a}$. Materials with a smaller β will tend to have a higher transmission. The transmission also depends on the energy-dependent attenuation coefficient, μ. The multiplicative product $\mu \cdot \beta$ is shown in Fig. 2-2 from 10 eV to 10 keV. The value of μ was estimated from the semi-empirical x-ray transmission data from CXRO.

2.7 Optimization Methods

The analytical strength model and the x-ray transmission model were combined for the optimization routine. A differential evolution[38] method from SciPy 1.7[39] was used to maximize transmission at one or more arbitrary energies. The model parameters (see Table 2-1) include the support length, width, spacing, and thickness for both the primary and secondary support structures, along with the width and thickness of the membrane. Each layer had a selectable material, as well. However, not every parameter is free to vary. For example, the secondary support length is defined by the primary support structure spacing, since that is the distance it must span. Other parameters were fixed by the choice of material or the manufacturing process. Finally, some parameters (such as the primary support width) were fixed to simplify the model.

The optimization routine was performed on two types of x-ray windows, each with two different membrane materials. The first was a traditional (two-layer) window, containing only the primary silicon support structure and membrane. The second was a hierarchical (three-layer) window, which additionally contained a secondary silicon support layer. Parallel ribs were chosen as the geometry of the support structure, as mentioned previously. The two- and three-layer windows were optimized for both a polymer and a silicon nitride window. See Table 2-1 for a list of window parameters, including which were fixed by some internal or external consideration and which were free to vary during the optimization.

The optimization returned the parameter set yielding the highest x-ray transmission at the desired energies. The analytical strength model assured that the membrane and support structures were strong enough to withstand at least 1 atm of pressure. (All analytical strength simulations were done assuming a pressure of 2 atm in order to give a margin of error to the calculation, because some of the model assumptions might underestimate the resulting film or beam stress.) The resulting window parameters were used in the finite element model, as a sanity check on the analytical results. Only 1.2 atm was applied to the window in the finite element model, because it does not have some of the simplifying assumptions that the analytical model has.

The optimization routine can select for transmission at one or more arbitrary energies. It does this by either integrating the transmission between two energies, or summing the transmission at one or more arbitrary energies. We chose to optimize for transmission at the following energies (in eV): 54.3, 108.5, 183.3, 277, 392.4, 524.9, 676.8, 1041, and 1740. These are the Kα energies for several low-Z elements. By optimizing transmission at these energies, we hoped to improve low-energy transmission without sacrificing high-energy transmission.

2.8 Results

The x-ray transmission model matches closely to synchrotron transmission data of an AP3 film. In [40], x-ray transmission through AP3 x-ray windows (without supports) was measured at the Advanced Light Source (ALS) at Lawrence Berkeley National Laboratory. We created two models of an AP3 x-ray window (one with only the film and the other with the film and support structure) to compare the estimated transmission with the synchrotron data (see Fig. 2-3). The Kα energies of various elements are marked with vertical lines. Deviation between the film model and the synchrotron data is expected, especially near element absorption edges, such as with carbon's Kα line (~280 eV). The overall close

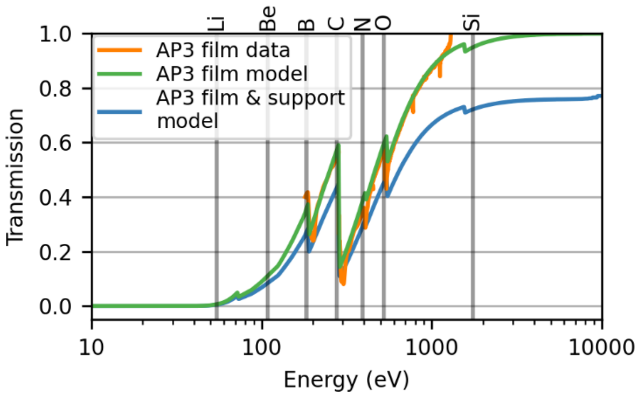

Fig. 2-3. Synchrotron x-ray transmission measurements of an unsupported x-ray window membrane compared to a model of the same window. The membrane is a layered composite film consisting of a polymer, an aluminum layer, and a gas barrier. The computed transmission for the membrane model, consisting of the above layers, matches closely to the membrane synchrotron data. The computed transmission for a model of the x-ray window membrane with a support structure is also shown. The Kα energies for some low-Z elements are indicated with vertical lines.

match between the model and the synchrotron data lends confidence to the x-ray transmission model for other films without synchrotron data.

The optimization routine (which selects for increased transmission) was performed on four different x-ray window models: traditional (two-layer) and hierarchical (three-layer) for both polymer and silicon nitride membranes. The output parameters of the optimization are listed in Table 2-3. The two-layer x-ray window models only had one free parameter: primary support spacing d_p. The pressure membrane thickness was calculated using Eq. (2.3) based on the support spacing. The three-layer x-ray window models had three parameters: primary support spacing d_p, secondary support spacing d_s, and secondary support width w_s. The optimization routine had constraints imposed on several parameters in order to remain in a region of manufacturability. Therefore, the optimization routine either finds an optimum within the specified region, or runs up against a constraint. The calculated thickness of the pressure membrane was at the lower limits imposed by the constraints (150 nm for polymer and 20 nm for Si–N). If thinner (but still robust) membranes could be fabricated, then transmission could be improved even further. The secondary support width was also at the lower limit (5 µm). Narrower beams can be fabricated, but it is necessary to avoid overly slender beams that are susceptible to buckling.

The estimated x-ray transmission for the optimized models can be seen in Fig. 2-4. The traditional (two-layer) polymer window has a transmission very similar to that of the commercial polymer-based AP3 (see Fig. 2-4a). Relative to AP3, the hierarchical (three-layer) polymer windows shows an increase in both low- and high-energy transmission. The added secondary support structure made it possible for the primary support structure open area to increase (thereby increasing high energy transmission) and for the pressure membrane thickness to decrease (thereby increasing low-energy transmission). Fig. 2-4b shows the transmission for the Si–N models compared to the commercial Si–N C2 window. At higher energies, the transmission of the C2 window surpasses the transmission for both models because the C2 window's support structure is much thinner (8 μm) compared to the models' support structure (375 μm). The transmission elsewhere is higher in both the traditional and hierarchical windows compared to C2, because both window models have thinner Si–N membranes than C2 (30 nm for traditional, 20 nm for hierarchical, and 40 nm for C2).

Finite element analysis was used to give additional support to the analytical strength model. The optimization results in Table 2-3 were used for the window geometry. Fig. 2-5 shows the stress and displacement finite element results for the relevant segments of each window. For each of the four modeled x-ray windows, the maximum stress for the support structures was less than the ultimate strength of silicon, indicating the support structures could withstand at least 1.2 atm of applied pressure. The maximum stress was 150 MPa (75% of yield strength) and 190 MPa (95% of yield strength) for the two- and three-layer polymer windows, respectively. For the two- and three-layer Si–N windows, the maximum stress was 2.6 GPa (65% of ultimate strength) and 3.6 GPa (90% of ultimate strength), respectively. For the three-layer windows, the maximum membrane stress occurs near the support frame (top left of Fig. 2-5b and d). In other areas, the membrane stress is similar to the two-layer window membrane stress. The stress near the support frame in the three-layer windows can be alleviated by increasing the width of the secondary support rib closest to the support frame. In all four cases, the stress in the finite element model does not exceed the yield/ultimate strength of the respective material. This is in good agreement with the analytical model.

Table 2-3
X-ray Window Parameter Optimization Results

Window type	Layer	Parameter	Polymer (µm)	Si–N (µm)
Traditional supported x-ray window	Primary support	d_p, Spacing	165	300
	Pressure membrane	t_m, Thickness	0.25	0.03
Hierarchical x-ray window	Primary support	d_p, Spacing	1800	1900
	Secondary support	d_s, Spacing	100	190
		w_s, Width	5	5
	Pressure membrane	t_m, Thickness	0.15	0.02

2.9 Discussion

The x-ray transmission model for AP3 matches closely to the synchrotron data, as seen in Fig. 2-3. This gives confidence to the other transmission models for windows that do not have matching synchrotron data. The transmission models are all built up using semi-empirical x-ray transmission information from the Center for X-ray Optics (CXRO). Despite these transmission models tending to break down near absorption edges (as can be seen near the carbon Kα line at 280 eV in Fig. 2-3), they are still sufficient for the purpose of comparing x-ray window models.

We modeled x-ray windows and optimized their parameters for low-energy x-ray transmission. The two-layer polymer window model and AP3 had similar primary support spacing (165 µm vs. 200 µm) and membrane thickness (250 nm vs. 300 nm), and therefore similar transmission. The optimized window had slightly increased low-energy transmission compared to AP3, because the optimization routine selected for low-energy transmission (see Fig. 2-4a). As a result of having increased low-energy transmission, the two-layer window's higher-energy transmission was reduced. This is the tradeoff inherent in traditional window designs, as shown in Fig. 2-1b.

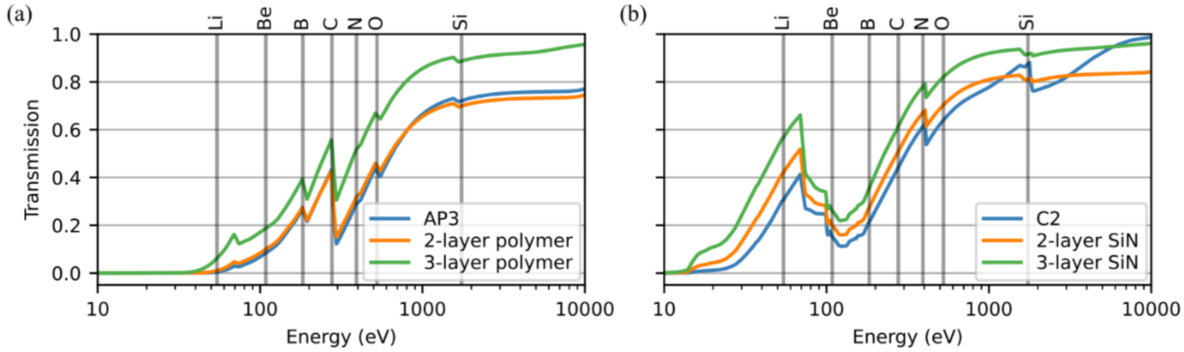

Fig. 2-4. X-ray window transmission gains achievable by adding a third layer in two different material systems. (a) The transmission of the optimized traditional (two-layer) polymer window matches closely to that of AP3. The optimized hierarchical (three-layer) polymer window shows improved low-energy and high-energy transmission performance. (b) The optimized Si–N windows are compared to the ultra-thin Si–N window C2. The two- and three-layer Si–N windows have improved low-energy transmission compared to C2 because their membranes are 30 nm and 20 nm, respectively. However, C2's high-energy transmission is greater because its polysilicon support is only 8 µm thick.

This tradeoff can be overcome by using a window with a hierarchical support structure. The optimized hierarchical (three-layer) polymer window has both increased low-energy and high-energy transmission. This was accomplished by greatly spacing out the primary support beams and adding a secondary support structure. This both increases the primary support structure open area (the main impediment to high-energy transmission) and decreases the membrane thickness. These benefits come with increased difficulty in manufacturability and with a possible loss in robustness. Unfortunately, it is difficult to create robust ultra-thin suspended polymer films. The thickness of the polymer membrane for the three-layer window is half of the AP3 polymer thickness and is the minimum thickness available in Moxtek's ProLINE windows. To get even thinner pressure membranes, it is necessary to move to a high strength material like silicon nitride.

Silicon nitride is about 20 times stronger than the polymer used in AP3, which means much thinner membranes can span the same (or greater) distance. Fig. 2-2 shows other possible membrane materials, including silicon, boron nitride and graphene. Though these other materials could theoretically perform better than silicon nitride in x-ray window applications, each has its drawbacks. For example, using silicon for both the support and the membrane poses etching selectivity challenges (i.e. how to etch the support without etching the much thinner membrane). In addition to having a high strength, these materials are potentially more chemically inert and able to withstand higher temperatures than polymer. Polymer still retains the significant benefit of its ductility, where stress concentrations are less likely to cause catastrophic failures. Further research into x-ray windows with these high strength materials could greatly improve transmission, especially in the low-energy regime.

The optimized traditional (two-layer) Si–N window has remarkably good low-energy and high-energy transmission (see Fig. 2-4b). Compared to the ultra-thin Si–N window C2, the low-energy transmission is higher, but the high-energy transmission is attenuated by the thick silicon ribs of the primary support structure. This performance comes because Si–N is able to span a support structure similar to AP3 while being much thinner than AP3's polymer membrane.

The optimized hierarchical (three-layer) Si–N window shows an even greater improvement in transmission. The membrane thickness was limited by the lower bound constraint of 20 nm. This was chosen as a reasonable limit for suspended Si–N, but thinner films have been made[26]. The gain in transmission over AP3 is significant, but the gain is less substantial when compared with the two-layer Si–N model. For high strength materials like Si–N, the benefits of using a hierarchical support structure may not outweigh the added complexity of fabricating a secondary support structure.

Our model and optimization routine did not take into account acceptance angle. Not only does decreasing the primary support spacing decrease the open area, it also decreases the acceptance angle of the window. That means that x-rays with a non-normal incidence will tend to be blocked by the support structure. For this reason, producing an x-ray window with a very

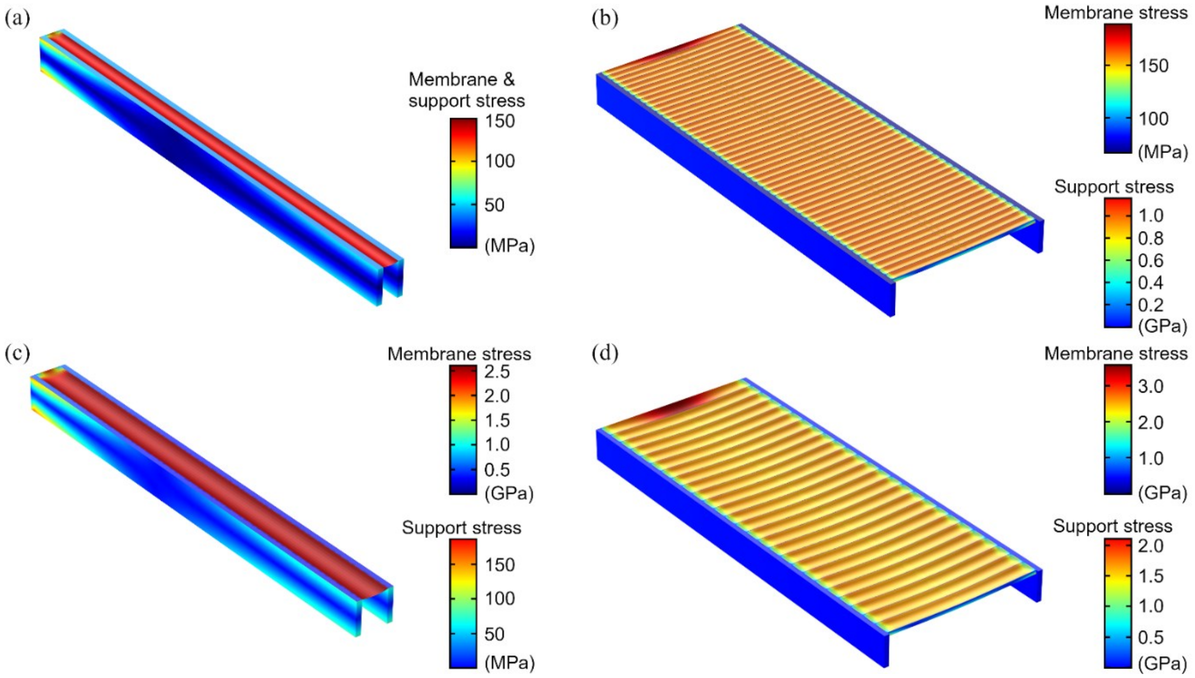

Fig. 2-5. Finite element modeling results of x-ray window support structure and membrane under 1.2 atm of pressure. Each model is attached to the fixed support frame (not pictured) at the top left, while the bottom right is a symmetry boundary condition. (a) A 250 nm polymer membrane is suspended between the two primary beams, which are spaced 165 µm apart. (b) A 150 nm polymer membrane is suspended between secondary supports that are 100 µm apart that in turn span the 1.8 mm gap between the primary supports. (c) A 30 nm Si–N membrane is suspended between the two primary beams, which are spaced 300 µm apart. (d) A 20 nm Si–N membrane is suspended between secondary supports that are 190 µm apart that in turn span the 1.9 mm gap between the primary supports. The maximum membrane stress was: (a) 150 MPa, (b) 190 MPa, (c) 2.6 GPa, and (d) 3.6 GPa. The stress in the supports in (b) and (d) is primarily in the secondary supports.

narrow spacing (and therefore very thin pressure membrane) is not a feasible way to increase low-energy transmission. In the future, our model and optimization routine could be expanded to include acceptance angle.

The finite element modeling results show that the simplifications used to make the analytical model are appropriate. Neither the membrane stress nor the support structure stress exceeded the yield or ultimate strength of the respective material. The highest membrane stress occurred in the three-layer windows near the support frame (top left of Fig. 2-5b and Fig. 2-5d). This stress, which was about 40% higher than the maximum stress elsewhere in the membrane, can be alleviated through careful design of the support structure. For example, if the first rib of the secondary support structure (nearest the support frame) were made wider, it would not deflect as much, leading to lower stress in the membrane. Indeed, these windows were optimized using simplified analytical methods. Although the stress calculations of the two methods seem to agree, the actual manufacturability of these windows requires further study.

2.10 Conclusion

We have created a combined strength and transmission model for analyzing x-ray detector windows. The model was used to optimize two traditional x-ray windows with a silicon support structure and either a polymer or a Si–N pressure membrane. It was also used to optimize two hierarchical x-ray windows each with two silicon support structures (one much thinner than the other) and either a polymer or a Si–N pressure membrane. We found that significant improvement in transmission (up to 5x) can be gained for polymer windows by adding a secondary support structure; however, the gains for hierarchical Si–N windows (about 30%) may not outweigh the added manufacturing complexity since traditional Si–N x-ray windows already have such high transmission. These results indicate that new x-ray windows with improved low-energy transmission can be created with the help of a hierarchical support structure.

Chapter 3: Multipoint Force-Deflection Mapping of Microcantilevers

Authors: Kyle Larsen, Stefan Lehnardt, Bryce Anderson, Joseph Rowley, Richard Vanfleet, Robert Davis

Submitted to Review of Scientific Instruments on March 23, 2022. Currently under review (as of July 5, 2022).

I hereby confirm that the use of this article is compliant with all publishing agreements.

3.1 Abstract

Estimating the elastic modulus and strength of heterogeneous films requires local measurement techniques. For local mechanical film testing, microcantilevers were cut in suspended many-layer graphene using a focused ion beam. An optical transmittance technique was used to map thickness near the cantilevers and multipoint force-deflection mapping with an atomic force microscope was used to record the compliance of the cantilevers. These data were used to estimate the elastic modulus of the film by fitting the compliance at multiple locations along the cantilever to a fixed-free Euler-Bernoulli beam model. This method resulted in a lower uncertainty than is possible from analyzing only a single force-deflection. The breaking strength of the film was also found by deflecting cantilevers until fracture. The average modulus and strength of the many-layer graphene films are 300 GPa and 12 GPa, respectively. The multipoint force-deflection method is well suited to analyze films that are heterogeneous in thickness or wrinkled.

3.2 Introduction

Here we will describe a method for characterizing the mechanical properties of heterogeneous thin films, which we call multipoint force-deflection (MFD). We will analyze the applicability of this method in characterizing many-layer graphene (MLG) films that are heterogeneous in thickness and contain wrinkles. Bulge testing is a common method for measuring the tensile strength and elastic modulus of suspended thin films[41]. With wrinkled or non-uniform films, the bulge test method can be used to determine deflection and burst pressure; however, it cannot quantitatively determine modulus or strength. The force-deflection or beam bending method is another established technique for determining material properties by applying a force to a microcantilever and measuring its deflection[42], which can be done using an atomic force microscope (AFM)[9], [43]. These small cantilevers make it possible to target specific locations on a film. For example, it is possible to measure over a distribution of thicknesses or to target areas devoid of wrinkles. Traditionally, the force-deflection method involves measuring the deflection from a known force at a single point along the cantilever. Euler-Bernoulli beam theory is then used to extract Young's modulus. A limitation of this technique is that an independent measurement of the distance from the applied force to the cantilever fixed end is required. Both the location of the applied force and the type of boundary condition at the cantilever fixed end can be difficult to determine. Here we introduce a modification to this technique that does not require an independent measurement of the distance from the applied force to the cantilever fixed end. This modification involves sequentially deflecting the cantilever at multiple locations along its length (see Fig. 3-1) and fitting both Young's modulus and the distance from the cantilever fixed end. Similar work has been reported previously on films suspended over circular holes[3], [44]–[46] and on fibers, modeled as doubly-clamped beams[47], [48]. All of these techniques require

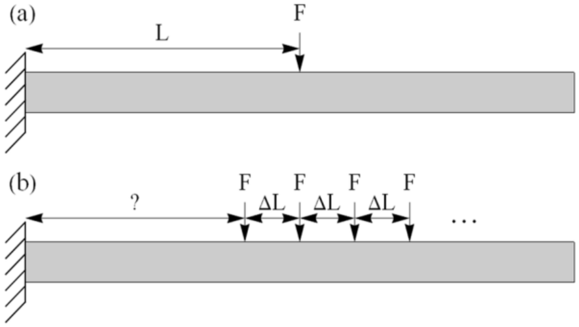

Fig. 3-1. Side-view schematic of cantilevers showing different force-deflection methods. (a) With single-point force-deflection, the location of the applied force relative to the fixed end must be known. (b) With multipoint force-deflection, the location of the applied forces to the fixed end is estimated through fitting.

knowing the thickness of the film, which is of critical importance in determining Young's modulus with cantilever bending because the modulus depends on the value of thickness to the third power. Various methods exist for measuring the thickness of thin films including ellipsometry, cross-sectional electron microscopy, and AFM step height measurement; however, these methods are all incompatible with the high-resolution thickness mapping necessary for local forced-deflection measurements. We use an optical transmittance mapping technique for determining MLG film thickness. We use finite element modeling to confirm the applicability of analytical Euler-Bernoulli beam theory to analyze MFD data.

Many-layer graphene is a thin film with tens to hundreds of graphitic layers. Graphitic carbon of this thickness is often called ultrathin graphite; however, we have chosen to use the term many-layer graphene because the films are grown using the same chemical vapor deposition (CVD) methods that produce monolayer, few-layer, or multilayer (up to 10 layers) graphene. Graphene has a reported Young's modulus of 1 TPa[3], [49], [50] and an ultimate tensile strength of up to 130 GPa [3]. Despite this high strength, monolayer to multilayer graphene films are too thin to be directly suitable for many microelectromechanical systems (MEMS) and larger-scale mechanical applications. MLG is an attractive mechanical material that has been used to demonstrate loudspeakers[6] and X-ray detector windows[4], [30], [51], [52]. However, characterization of the mechanical properties of MLG films has been limited. Characterization of MLG films can be complicated by large wrinkles and significant thickness heterogeneity. Both of these problems can be minimized with a local characterization method like MFD and with a local thickness measurement. In the case of MLG, thickness can be determined locally with optical transmittance[53], [54].

In this work, we show the applicability of the MFD method in analyzing wrinkled MLG films with thickness non-uniformity. Young's modulus was estimated from AFM force-volume mapping on ion-cut MLG microcantilevers. Additionally, several cantilevers were loaded until fracture to determine breaking strength. Thickness was measured using optical transmittance and AFM step height measurements. Our use of multipoint force-deflection shows improvements over single-point force-deflection and bulge testing by eliminating the need for an independent measurement of the fixed end location, by giving insight into the validity of the model and boundary condition assumptions, and by enabling the measurement of local film properties. Additionally, this technique is valuable for analysis of other suspended thin films, especially heterogeneous films that are traditionally difficult to characterize by bulge testing.

3.3 Materials and Methods

3.3.1 Finite element modeling of cantilever beams

The multipoint force-deflection method was explored with finite element modeling (FEM) using COMSOL Multiphysics. Three simple models were developed to test slightly different boundary conditions, as shown in Fig. 3-2. In the first model, the end was fixed as typical for a fixed-free cantilever beam. In the second model, the end was extended over a fixed surface, to represent well-adhered MLG over silicon. The third model, representing poorly adhered MLG over silicon combined the fixed end of the first model and a simple support at the edge of the silicon. In the second and third models, the

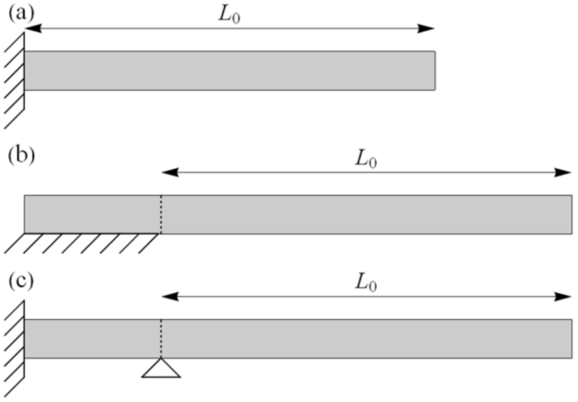

Fig. 3-2. Side-view schematic of three cantilever boundary conditions. (a) Cantilever with classically fixed end, referred to as BC 1. (b) Cantilever fixed to silicon support, referred to as BC 2. (c) Similar to (b), but not well adhered to silicon, referred to as BC 3. The length $\mathbf{L_0}$ is the same for all three cases.

region extending over the silicon is half the total cantilever length L_0. The first two models were expected to give similar force-deflection results. In fact, the expectation was that the second model would be close enough to the first to justify using the simpler fixed-free analytical model to analyze the collected force-deflection data. The third model was developed to show how different the deflection results could be when the fixed end boundary condition was not achieved. All three models used the same length, width, thickness, and materials properties. The modulus was defined as $E_{FEM} = 1$ TPa. To test the MFD method, each of these models had a series of equally spaced forces applied. The force-deflection results were then analyzed with the same technique that was used to analyze the AFM force-volume data. This technique is described later.

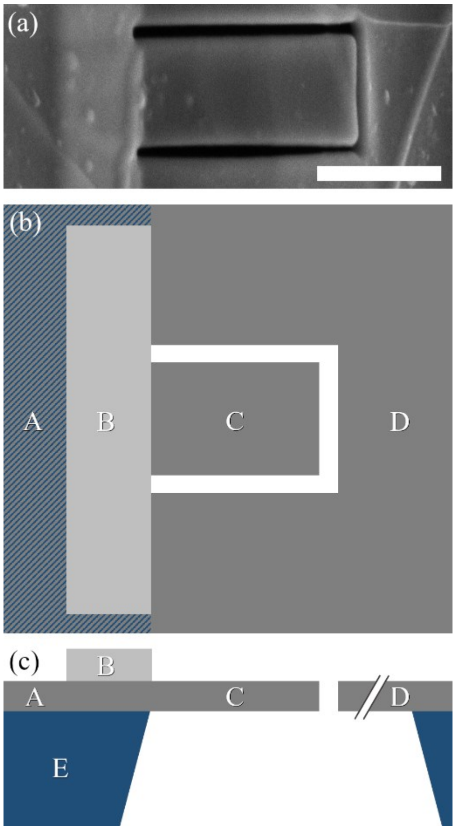

Fig. 3-3. Geometry of a many-layer graphene cantilever. (a) Scanning electron micrograph of a cantilever cut in suspended MLG, with the fixed end at the edge of the silicon support and stiffened by platinum. The scale bar is 1 µm long. (b) Top view schematic of a cantilever cut into suspended many-layer graphene. In region (A) the MLG is over the silicon support structure. Region (B) is the platinum bar that is e-beam deposited at the fixed end of the cantilever. The cantilever itself is region (C); it, along with region (D), are on the suspended MLG. (c) Side-view schematic of a cantilever cut into suspended MLG. The letters represent the same regions as in (b) with (E) indicating the silicon support frame. The opening in the silicon support frame is much larger than the length of the cantilever, hence the scale break mark near (D).

3.3.2 Sample preparation

The MLG films were formed using a low-pressure chemical vapor deposition (LPCVD) process on a nickel substrate[4], [6]. Each film was then transferred to a silicon chip with an etched rectangular hole using a polymer assisted transfer process, resulting in suspended MLG over the hole. The silicon support frame allows for the film to be suspended and for cantilevers to be cut in the suspended film. The etched rectangular holes ranged in width from 100 µm to 500 µm, with the length being six times the width. For details on the growth and transfer process, see the supplemental material for this paper.

A series of MLG cantilevers was formed by cutting the suspended MLG film with a focused ion beam (FIB) of gallium ions in a FEI Helios NanoLab 600 DualBeam scanning electron microscope (SEM). The cantilevers ranged in size from about 0.5 µm x 1 µm to 3 µm x 6 µm. Most of the cantilevers were aligned with their fixed end at the edge of the silicon and their free ends over the opening in the silicon support structure, as seen in Fig. 3-3. The first boundary condition from Fig. 3-2 was intended to model these cantilevers. Other cantilevers were formed by cutting past the edge of the silicon so that their fixed end was not at the edge of the silicon, but one or more microns back. The boundary condition for this second type of cantilever should be similar to the second or third case from Fig. 3-2, depending on how well adhered the MLG is to the silicon support structure. In both cases, this process results in cantilevers that can be freely deflected downward by AFM even to the large deflections needed for breaking (several hundred nanometers). However, the transfer process may not completely fix the end of the cantilever to the silicon because of incomplete adhesion of the film to the silicon support. In order to increase the stiffness of the fixed end so that the cantilever deflects more like a fixed-free cantilever, some cantilevers had platinum bars deposited on the MLG where the cantilever meets the silicon. This was done using electron beam induced deposition of platinum in the dual beam SEM where the FIB cutting was performed. The width of each cantilever was measured by both AFM and SEM.

3.3.3 Thickness measurements

Min and MacDonald [53] and Zhu et al. [54] showed that the optical transmittance through multilayer graphene can be approximated with $T = (1 + f(\omega)\, \pi\alpha\, N/2)^{-2}$ where α is the fine-structure constant and $N = t/t_0$ is the number of graphene layers. Zhu et al. determined $f(\omega)$ to be 1.13 for 550 nm light and concluded that this was a good value for the visible range. With each graphene layer having a thickness of $t_0 = 0.335$ nm, this equation can be solved for thickness (in nanometers) as a function of transmittance:

$$t = \frac{2t_0}{f(\omega)\pi\alpha}\left(\frac{1}{\sqrt{T}} - 1\right) = 25.86\,\left(\frac{1}{\sqrt{T}} - 1\right) \qquad (3.1)$$

An optical transmittance map of the film was measured as follows. Three-channel color images were taken using an Olympus BX60F5 microscope with a tungsten halogen lamp and a Sony α7II 14-bit digital camera with a linear response (RAW format). Linearity of the camera sensor was confirmed with a series of neutral density filters and a constant intensity light source. The digital camera's settings were fixed to ensure no saturated pixels before taking an image without the MLG to record the intensity of the incident light. A second image was taken to record the intensity of the transmitted light through the suspended MLG film. The intensity of the halogen lamp was not changed between images. Care was taken to minimize extraneous light by turning off the room lights and illuminating the sample through an aperture. The green channel of the second image (MLG transmission intensity) was divided by the green channel of the first image (incident intensity). The result was an image with pixel values representing transmittance according to $T = \Phi/\Phi_0$ where Φ is the intensity of the transmitted light and Φ_0 is the intensity of the incident light. The green channel was chosen because its peak sensitivity is closest to the 550 nm wavelength used by Zhu et al. A thickness map was created by applying (3.1) to each pixel in the transmittance image.

As an independent verification of film thickness, the film was also measured with a Bruker Dimension V atomic force microscope (AFM). With the MLG lying flat on the silicon substrate, an edge of the MLG film was found and the step height from the silicon to the film was measured in several places. This method can be used to estimate an average film thickness, but the measurement is always performed at the edge of the film, far away from the suspended area. Due to the non-uniformity of the films, the step height measurements alone are not sufficient in determining the thickness at the location of the cantilevers.

3.3.4 Mechanical testing

The force-deflection or beam bending method for determining the Young's modulus of a material is performed by measuring and analyzing the deflection of a cantilever versus applied force. The stiffness k of a cantilever with one fixed end and one free end is related to its geometry and the Young's modulus of the material according to Euler-Bernoulli beam theory[36].

$$k = \frac{Ewt^3}{4L^3} \tag{3.2}$$

where E is the Young's modulus, w is the cantilever width, t is the cantilever thickness, and L is the distance from the fixed end of the cantilever to the applied force. Breaking strength is found by increasing the applied force until the cantilever breaks. The maximum stress at breaking σ_{max} is given by

$$\sigma_{max} = \frac{6FL}{wt^2} \tag{3.3}$$

where F is the magnitude of the applied force[36]. A disadvantage of the standard force-deflection method is that an independent measurement of L is needed. This measurement can be difficult because of uncertainties in both the location of the fixed end and the location of the applied load. When using an AFM, the force is applied by the AFM cantilever tip, but there is no intrinsic measurement of where the tip contacts the sample relative to the fixed end of the cantilever. A modification to the standard force-deflection method involves deflecting the cantilever at multiple locations along its length and fitting both Young's modulus and an offset in the position of the applied force. As mentioned in the introduction, we call this the multipoint force-deflection (MFD) method. This modification alleviates the requirement of an independent measurement of L. MFD does require, however, multiple force-deflection ramps with known spacing along the cantilever. Conveniently, automated force-volume mapping with an AFM results in a two-dimensional array of evenly spaced force-deflection ramps. Force-volume mapping was used to measure Young's modulus, while single force-deflection ramps were used for measuring strength.

3.3.4.1 Force-volume measurement

On a Bruker Dimension V atomic force microscope, a force-volume (FV) measurement consists of capturing a square array of force-deflection ramps. After the region of interest is found using tapping mode imaging, the FV scan is set up with a specific trigger threshold for the force-deflection ramp. The ramp is engaged and, once that trigger value is reached, the ramp is reversed and the data for both the approach and retract ramps are saved. This is done for each point in the FV map. The stiffness of the AFM cantilever must be similar to that of the MLG cantilever. If it is too stiff, the AFM will not detect any displacement; and if it is too compliant, almost all of the displacement will be in the AFM cantilever and not the MLG cantilever. It is necessary to calibrate the force-ramp against a much stiffer surface, such as the silicon support structure. This can be done by taking a single force ramp measurement on a stiff surface either before or after the FV measurement. It is also possible to use some of the FV data for the calibration, as long as part of the MLG in the scan is in direct contact with the silicon support

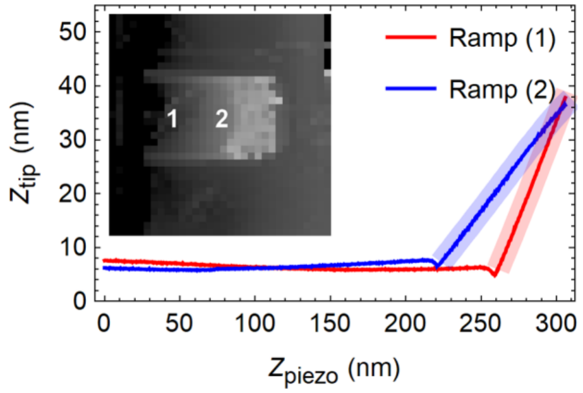

Fig. 3-4. Compliance map of an MLG cantilever and two different force-deflection ramps. The slope used in the analysis is taken from the light blue and pink highlighted linear regions of the force-deflection curves. (Inset) Force-volume compliance map where the intensity represents the local compliance of the film, which is inversely related to the slope of the force-deflection curve. Ramp (1) is closer to the fixed end than Ramp (2).

structure. The average slope of the force ramps on the MLG over the silicon was used as the calibration factor for the data presented in this study. The calibration factor converts the recorded tip deflection from volts to nanometers and is often called the tapping mode deflection sensitivity. To convert this to a force, the AFM cantilever stiffness must be determined as described in the next section. Most of the data in this work were captured in 64x64 pixel maps. With a fast scan setting enabled, each FV map took about 35 minutes to acquire. FV data can be represented as a two-dimensional image by using the slope of a certain region of each of the force-deflection curves to represent the image intensity. Such an image would be called a stiffness map and its inverse a compliance map. Fig. 3-4 shows a typical FV dataset represented as a compliance map, along with two force-deflection curves.

3.3.4.2 Analysis of force-volume data

The force-volume data consist of multiple force-deflection curves from which several are selected, converted to a compliance, and analyzed as a group to yield a Young's modulus. The force-deflection ramps along the centerline of the cantilever from the fixed end to the free end were selected for the analysis. The exact location of the fixed end is uncertain because of the poorly defined boundary between the cantilever and the silicon support; however, the MFD method does not require a priori knowledge of the fixed end location because an offset is fit. Each force-deflection ramp consists of three regions corresponding to pre-contact with the AFM cantilever, transition to contact, and contact. For an ideal force curve, the part corresponding to contact with the AFM cantilever will be linear, as seen in the highlighted regions of Fig. 3-4. The slope s of the linear portion can be related to the stiffness of the MLGC (many-layer graphene cantilever). This relationship is found by considering the interaction between the AFM cantilever and the MLGC as a system of two springs, as presented in Fig. 3-5. The total displacement $z_{piezo} = z_{tip} + z_G$ is the sum of the displacement of the AFM cantilever, z_{tip}, and the MLG cantilever, z_G. The force on the MLGC is equal to the force on the AFM cantilever, $F_G = k_G z_G = F_{tip} = k_{tip} z_{tip}$. Here, we work with compliance (the inverse of stiffness), in which case $k_G^{-1} = k_{tip}^{-1} z_G / z_{tip} = k_{tip}^{-1}(z_{piezo} - z_{tip}) / z_{tip}$ or

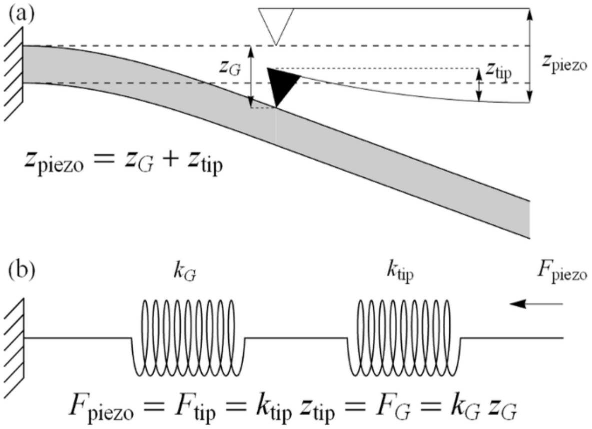

Fig. 3-5. Model of the interaction between the AFM cantilever and the MLG cantilever. (a) The deflection model shows that the deflection of the AFM piezo is the combined deflection of the AFM tip and the MLG cantilever. (b) The spring model allows for the transformation from the deflection model to the stiffness or compliance model.

$$\text{Compliance} = \frac{1}{k_G} = \frac{1}{k_{tip}}\left(\frac{1}{s} - 1\right) \tag{3.4}$$

where $s = z_{tip}/z_{piezo}$. Compliance is used to fit to the modified Euler-Bernoulli beam equation

$$\frac{1}{k_G} = \frac{4(L-c)^3}{Ewt^3}, \tag{3.5}$$

where $1/k_G$ is the compliance of the MLG at the measured loading point, L is the position of the applied load relative to some initial visual estimate, c is an offset in the applied load position, E is Young's modulus, w is the MLGC width, and t is the MLGC thickness. The data were fit to (3.5) using a weighted nonlinear fitting function in Mathematica 12.2. The weight for each

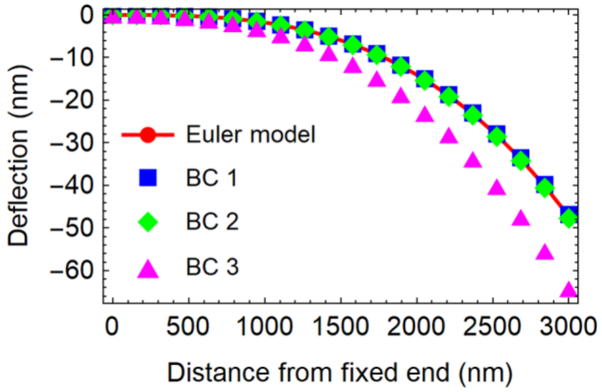

Fig. 3-6. Cantilever deflection results from finite element analysis. The three boundary conditions (BC 1-3) are introduced in Fig. 3-2. Both BC 1 and BC 2 match the analytical results of the Euler-Bernoulli beam model. BC 3 diverges significantly, as expected.

measurement point was calculated from the uncertainty in both k_G and L as $\delta = \sqrt{\delta k_G^{-2} + \delta L^{-2}}$. Eq. (3.5) can also be fit with a linear regression by taking the cube root of both sides before fitting.

The stiffness of the AFM cantilever, k_{tip}, can be estimated in multiple ways. One method is to use vibrometry to measure the resonance of the AFM cantilever, but thickness must be known. AFM cantilever thickness is variable, and measuring the thickness of each fragile tip requires handling that could damage the tip. A method was developed by Sader et al.[55] that simplifies estimating the stiffness of an AFM cantilever. Sader et al. classified the same type of tip that we used (NanoWorld NCHR); because of this, we can use their model if we know tip length, tip width, tip resonant frequency and quality factor, the air density, and the air shear viscosity. We used $\rho = 1.018\ kg/m^3$ and $\mu = 1.813 * 10^{-5}\ Pa \cdot s$ for density and shear viscosity, respectively. Tip resonant frequency and quality factor were measured with the AFM before each force-volume measurement. The tip length and width were measured with an optical microscope for each AFM cantilever.

3.3.5 Raman spectroscopy of suspended MLG before and after FIB cutting

Raman spectroscopy was used to characterize the many-layer graphene films[56], [57]. In the analysis of graphene by Raman spectroscopy, the three main peaks of interest are called D, G, and 2D and are located at Raman shifts of 1350 cm^{-1}, 1580 cm^{-1}, and 2700 cm^{-1}, respectively. The D peak indicates disorder in the graphene crystal. The lower the intensity of this peak, the higher the quality of graphene. The ratio of intensities of the G peak to the 2D peak gives an indication of the number of graphene layers in the film. For monolayer graphene, the G peak is smaller than the 2D peak. Conversely, for multilayer graphene and high quality graphite, the G peak is larger than the 2D peak. In this study, Raman spectroscopy was used to characterize the quality of the MLG films. Using a Renishaw inVia Raman spectroscopy microscope, Raman spectra were measured for MLG both before and after cutting the cantilevers with the focused ion beam. A 532 nm laser (Renishaw RL532C50) and a 50x objective resulted in a laser spot size approximately 1 µm in diameter. A diffraction grating for visible light with 1800 lines per millimeter was used.

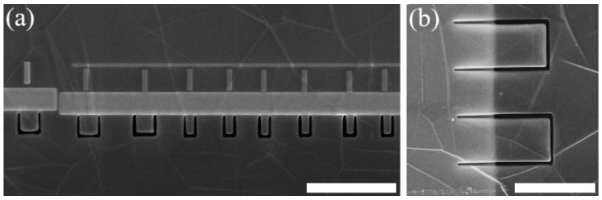

Fig. 3-7. Scanning electron micrographs of MLG with cantilevers. (a) Cantilevers from Sample A with platinum bar stiffener, going from 1 µm x 1 µm on the left to 0.5 µm x 1 µm on the right. The thicker horizontal bar above the cantilevers is the platinum stiffener. The thinner vertical and horizontal bars are navigation markers for AFM. (b) The two cantilevers from Sample B, which lack a platinum stiffener. The lighter tone in the left half of the image is from the silicon underneath the MLG. The cut forming the cantilever extends back onto the silicon, resulting in a cantilever that is significantly shorter than the total cut length, if the cantilever hits the silicon edge while deflecting downwards. The cuts form a cantilever that

3.4 Results

Finite element modeling of a cantilever with the three different boundary conditions described in Fig. 3-2 shows agreement between the first two boundary conditions and the analytical Euler-Bernoulli model. As expected, the third boundary condition does not match the analytical model. Two suspended MLG films were prepared with FIB cut cantilevers. Local thickness was measured near the cantilevers to be about 72 nm for one film and 160 nm for the other. The average Young’s modulus was about 300 GPa with a breaking strength of about 12 GPa. The focused ion beam used to create the cantilevers caused changes in the films, as evidenced by the formation of a strong D peak in the Raman spectra after ion-cutting.

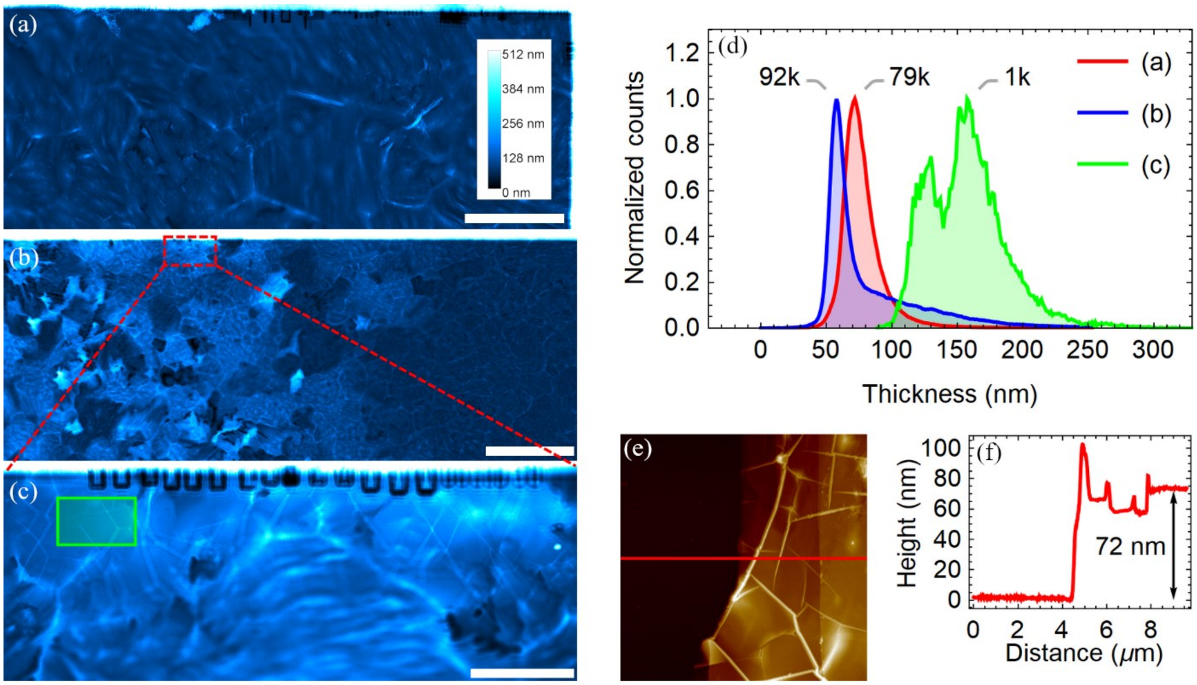

Fig. 3-8. Thickness results for Sample A and Sample B. (a) Thickness map of Sample A at 50x, with cantilevers visible near the top of the image. Scale bar is 25 μm. (b) Thickness map of Sample B at 5x. Scale bar is 200 μm. (c) Thickness map of Sample B at 50x with cantilevers visible near the top of the image. Scale bar is 25 μm. (d) Thickness distribution of (a), (b), and the region highlighted in green of (c). The peaks are marked with their original count values, which were used for normalization. (e) AFM step height scan of Sample A. The scan is 10 μm square. (f) Height profile from scan in (e) showing 72 nm thickness.

3.4.1 Finite element modeling

Finite element modeling (FEM) results of cantilevers with the three different boundary conditions were compared, as described in the Methods (see Fig. 3-2). Deflection as a function of applied force is shown in Fig. 3-6 for the finite element solutions of all three models and the analytical (Euler-Bernoulli) solution. For the first two models, the calculated modulus was $E_{FEM} = 1.01$ TPa, which is within 1% of the value used for the FEM analysis. However, for the third boundary condition, the calculated modulus was $E_{FEM} = 0.89$ TPa. This method also returns an offset in the fixed end location. The offset for each boundary condition was -0.01 μm, -0.02 μm, and -0.2 μm, respectively and relative to the start of L_0 in Fig. 3-2. The negative value indicates that the MFD method estimates the fixed end to be to the left of the given origin, using the orientation of the cantilever extending to the right.

3.4.2 Suspended many-layer graphene film fabrication and preparation

Films were grown on two separate nickel foils that were then transferred onto silicon support structures, resulting in two samples: Sample A and Sample B. Platinum bars were deposited as stiffeners at the edge of the silicon on Sample A. The platinum thickness was around 200 nm. Micrographs of the two films (after FIB cutting) are shown in Fig. 3-7. Sample A was placed on a silicon support structure with an open area of 120 µm x 620 µm, while the silicon support structure for Sample B had a larger open area of 530 µm x 3020 µm.

A gallium ion beam was used to cut cantilevers in the MLG films, as shown in Fig. 3-7. A 1 µm x 1 µm cantilever could be cut in about 5 seconds with an accelerating voltage of 30 kV and a beam current of 0.44 nA. In order to find the desired location for cutting the cantilevers, at least one rastered ion beam image was taken. The number of exposures and the exposure time were limited to minimize damage to the surrounding film. Exposing cantilevers to sufficient ion radiation would cause them to curl up. Cantilevers with significant curl were not included in the study. Several dozen cantilevers were cut into both samples; however, not all of the cantilevers were used in the study. Cantilevers that were not included did not cut cleanly or were not well aligned with the edge of the silicon.

3.4.3 Thickness

MLG film thickness was measured with both an optical transmittance technique and by AFM step height. Fig. 3-8 shows the thickness results for the two samples in the study. Fig. 3-8(a-c) shows the thickness maps for Sample A (a) and Sample B (b, c). Fig. 3-8(d) shows the thickness distributions for all of (a) in red, all of (b) in blue, and the highlighted part of (c) in green. Gaussian functions were fit to the distributions in Fig. 3-8(d). The location of the peak of the Gaussian and its standard deviation were taken to be the thickness and uncertainty, respectively.

For Sample A (red curve in Fig. 3-8(d)), which was relatively uniform in thickness, the result of the optical transmittance measurement was (72 ± 7) nm. Additionally, step height measurements with the AFM ranged from 68 nm to 73 nm. One such step height scan is shown in Fig. 3-8(e-f). Sample B has two distinct thickness regions, as seen in the left and right halves of Fig. 3-8(b). The blue curve in Fig. 3-8(d) is the thickness distribution for both regions and the green curve is the distribution of just the region near the cantilevers (as highlighted in Fig. 3-8(c)). The thickness distribution of all of Sample B (Fig. 3-8(b)) peaked at 55 nm. Two Gaussians were fit to the distribution from Fig. 3-8(c) resulting in thicknesses of (120 ± 10) nm and (160 ± 20) nm. The 160 nm peak was chosen for the analysis because it was more prominent. The AFM step height measurements for Sample B ranged from 80 nm to 105 nm. These step heights were taken at the edge of the film, far from the cantilevers.

3.4.4 Young’s modulus

Young’s modulus was determined using 30 force-volume scans of 20 unique cantilevers from Sample A. The average Young’s modulus was (300 ± 20) GPa, where the uncertainty is the standard error (standard deviation divided by the square root of the number of samples). See the supplemental material of this paper for details on repeated measurements. Representative force-volume compliance maps from Sample A and Sample B are shown in the insets of Fig. 3-9(a) and (b), respectively. Also shown are graphs of the compliance as a function of position along the cantilever, as well as the fitted line (blue) from which Young’s modulus was extracted. The compliance map in Fig. 3-9(b) shows a jump in compliance near the middle of the cantilever. This is one of several non-ideal features in the cantilevers of Sample B that are important to understand and will be address in the discussion.

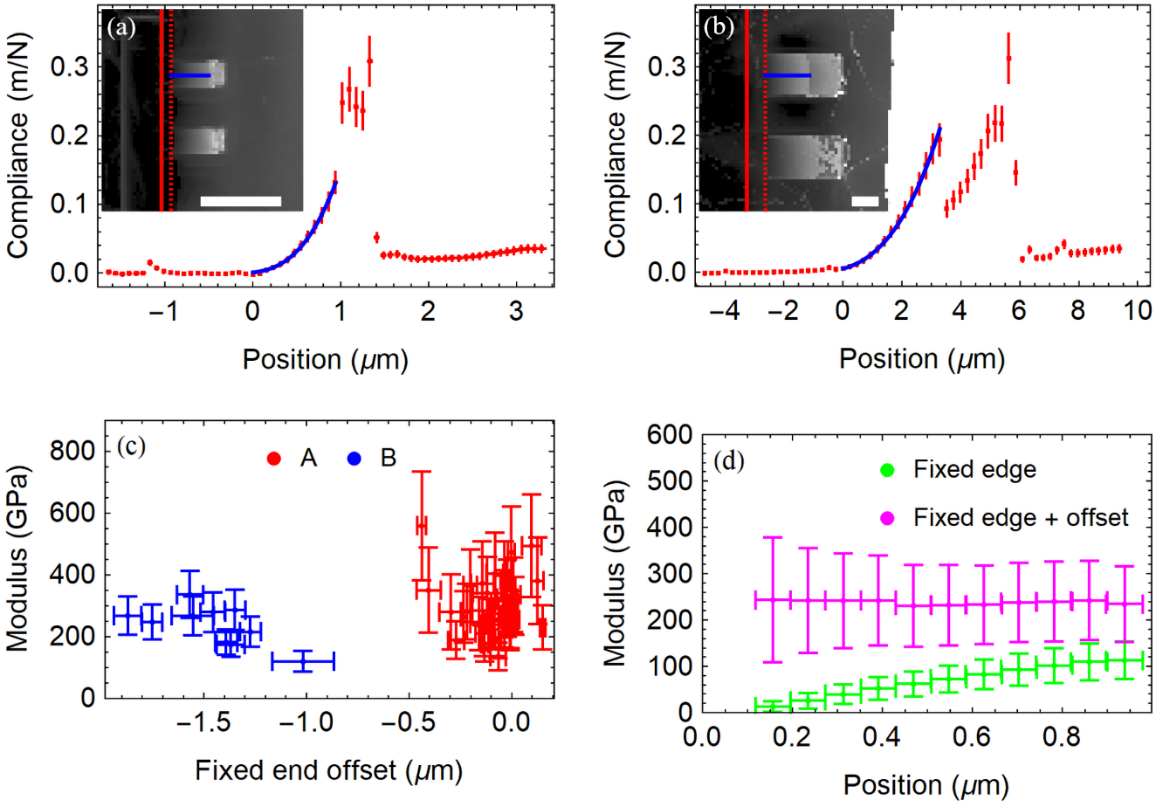

Fig. 3-9. Results of Young’s modulus measurements and calculations. (a) Inset shows compliance map with two cantilevers from Sample A. Lighter areas are more compliant. The horizontal blue line across the center of the top cantilever marks the location used for the MFD analysis and covers the same region as the blue line in the compliance plot. The solid vertical red line shows the position of the cantilever fixed end estimated by fitting, while the dashed red line shows the visual estimate of the cantilever fixed end. (b) Compliance map and plot from Sample B (see (a) for description of each). A jump in compliance immediately to the right of the blue line can be seen in both the map and the plot. The force-deflection curves (from which compliance is extracted) near the free end of the cantilevers and near the right edge of the map were often too noisy to extract meaningful data, hence the white pixels. (c) Each crosshair is the fitted Young’s modulus plotted against the fitted fixed end offset of a single cantilever. The offset is the distance from the visual fixed end of the cantilever to the fixed end determined by fitting. (d) The single-point force-deflection method at each point along the cantilever from (a) using the visual estimate of the fixed edge (green) and the fixed edge with the offset (magenta) found in (c). Without the offset, the value of the calculated modulus changes as a function of position along the cantilever. With the offset, the value of the modulus is independent of position along the cantilever, highlighting one of the benefits of the multipoint force-deflection method. The scale bars for the compliance maps in the inset of (a) and (b) are 2 μm long.

The offset in the fixed end position was significantly different between Sample A and Sample B, as seen in Fig. 3-9(c). A fixed end offset closer to zero means that the visual estimate for the location of the fixed end more closely matched the value from fitting. A negative offset means that the fit value was estimated to be to the left of the cantilever’s fixed end, according to the orientation in the compliance maps of Fig. 3-9(a,b).

Fig. 3-9(d) shows the results of using the single-point force-deflection method independently at each loading position. This method uses only a single loading to estimate Young’s modulus and so has no way to estimate the offset in the cantilever fixed end position. Two different cases are shown. In the first case (green), Young’s modulus is underestimated because our visual estimate for the fixed end location is not correct and an offset is not used. This also leads to the determined Young’s modulus changing at different positions along the cantilever. In the second case (magenta), the offset estimated from the MFD method is used, resulting in a position independent estimate of Young’s modulus. The range in moduli for the first case is 100 GPa, while it is only 10 GPa for the second case. The largest relative error in modulus for any of the points in Fig. 3-9(d) by the single-point method is 60%. The same sample analyzed with the MFD method returned a relative error of 20%.

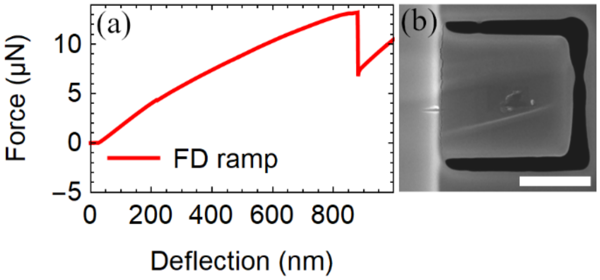

Fig. 3-10. Representative force-deflection ramp until failure and fractured cantilever. (a) Force-deflection ramp of cantilever that was loaded until fracture. (b) SEM image of cantilever and small crack that formed at the fixed end. Markings from the AFM tip are visible near the center of the cantilever and at the fixed end. The scale bar is 0.5 μm long.

3.4.5 Strength

To measure the strength of the films, five cantilevers from Sample A were deflected until fracture. The forces required to break the cantilevers ranged from 11 μN to 25 μN. According to (3.3), the resulting strength is (12 ± 2) GPa, with the uncertainty being the standard error. Fig. 3-10(a) shows the force-deflection ramp of a cantilever that broke at about 13 μN, with the broken cantilever pictured in Fig. 3-10(b). A fracture is visible at the fixed edge of the cantilever along the platinum bar. The force required to break the cantilever is far past its region of linear response, as seen by the changing slope in the force-deflection ramp. Each cantilever deflected several hundred nanometers before fracturing. With such high deflection, the angle between the cantilever and the AFM tip was large, facilitating tip slippage. We did not include nonlinear effects or tip slippage in our analysis because we did not have a method to quantify the position of the AFM tip after slipping.

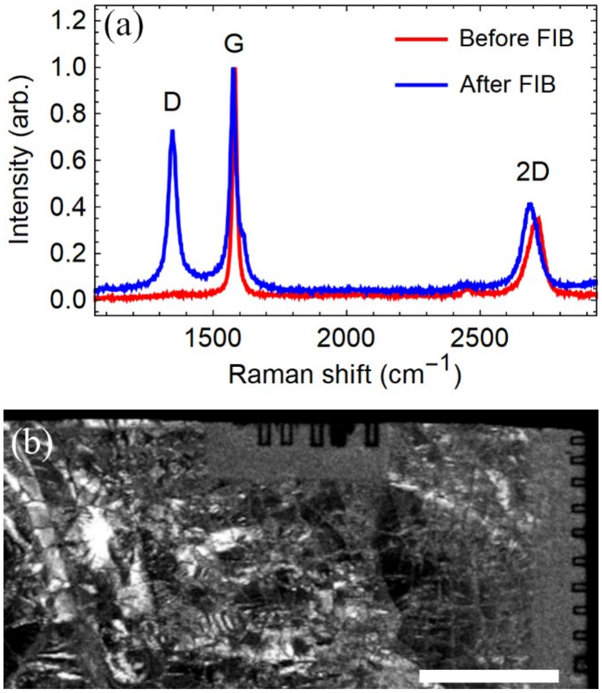

Fig. 3-11. Ion beam induced changes to MLG film. (a) Raman spectra before (red) and after (blue) processing with the focused ion beam. The spectra were normalized to their respective G peaks. Before ion beam processing, there is little to no observable D peak. A large D peak is present after processing. The D peak is indicative of graphitic disorder. (b) Scanning transmission electron microscopy dark-field image with 10-µm scale bar. The film near the cantilevers exhibits greater uniformity than the film farther away, indicating that the ion beam had a transformative effect on the MLG near the cantilevers.

3.4.6 Focused ion beam induced changes in film

Raman spectroscopy was used to characterize the quality of the CVD films, as shown in Fig. 3-11(a). There is little evidence for the D peak (1350 cm^{-1}) in films before FIB cutting or in areas of the film far from the FIB cutting. However, a strong D peak does form in areas near the MLG cut by the FIB. Fig. 3-11(b) shows a scanning transmission electron microscope (STEM) annular ring dark-field image taken with a FEI Verios G4 SEM. The contrast of the image is representative of the angle at which electrons scattered through the film. Near the cantilevers (top and right), the contrast is more uniform. It is clear that the topology of the film is different in these regions than in the rest of the film. These areas were exposed to ion beam imaging during FIB cutting.

3.5 Discussion

The finite element modeling results highlight the importance of understanding the cantilever boundary conditions and justify the use of a simple Euler-Bernoulli cantilever beam model for samples with a well-defined fixed end. The modeling results show only a small difference in deflection between the Euler-Bernoulli analytical model and the first two boundary conditions of the FEM (see Fig. 3-6), leading us to conclude that MFD can be used to extract Young's modulus for a cantilever with a well-defined fixed end. The third boundary condition from the FEM was used to illustrate how changes from the fixed end boundary condition can lead to large differences in deflection and therefore in the analysis of Young's modulus. The first two boundary conditions yielded a Young's modulus that was within 1% of the actual value, where the third boundary condition resulted in a difference of about 10%.

A significant benefit of the multipoint force-deflection method is that it allows for an independent determination of the location of the cantilever fixed end. Not only do the compliance maps provide a visual estimate of the fixed end location, but the MFD analysis itself returns a fixed end offset along with the estimate of Young's modulus (see the insets to Fig. 3-4 and Fig. 3-9). If the location of the fixed end is known with some confidence, then MFD's fixed end offset can be used to justify or reject the chosen model, as described in the following two paragraphs.

The cantilevers in Sample A had a platinum bar stiffener deposited at their fixed end. The stiffeners were an attempt to create a more ideal fixed end to enable MFD analysis using a simple fixed-free Euler-Bernoulli beam model. The results show that cantilevers with a stiffener had a smaller fixed end offset than cantilevers without a stiffener (see Fig. 3-9(c)). The fixed end offset and the visual estimate of the cantilever fixed end location were similar, indicating that the base of the cantilever acted like a fixed end, justifying in practice the use of the simple Euler-Bernoulli beam model which enables MFD analysis.

Analysis by MFD of the cantilevers in Sample B is complicated by their geometry and their lack of stiffeners. Fig. 3-7(b) shows that about half of the cut length is past the edge of the silicon. We expected the cut part of the MLG film over the silicon to have little compliance based on the assumption that the film and silicon would be in contact. However, it was clear from the force-volume map that the entire cut portion of the cantilever was compliant and was not in direct contact with the silicon (see Fig. 3-9(b)). A jump in compliance was observed when the cantilever finally deflected enough to contact the silicon (about halfway down the cantilever). This jump indicates that the cantilever was lifted up off the silicon, a condition not accounted for in the analytical model or in the finite element model. Also, the cantilevers in Sample B had a fairly large discrepancy between our best visual guess at the location of their fixed end and the fixed end predicted by the MFD analysis. Despite a good fit to (3.5), the estimated location of the fixed end would indicate a cantilever much longer than the cut cantilever (see Fig. 3-7(b)), leading us to conclude that the actual boundary condition is more complicated than any of our models. Lack of a good model for the cantilevers in Sample B precludes MFD analysis for the determination of Young's modulus.

When MFD data can be fit using the Euler-Bernoulli model, it can further reduce experimental uncertainties. With single-point force-deflection, any error in the location of the applied load is propagated to Young's modulus (see (3.2)). However, with MFD analysis, an error in location (i.e. an offset) affecting all loading points equally is removed by the fixed end offset (see (3.5)). An error affecting loading points differently, such as an error in the force-volume step size ΔL (see Fig. 3-1(b)), will still affect the modulus.

The fixed-free cantilever beam is not the only geometry where MFD is possible. Other authors have previously reported a similar technique that uses a doubly-clamped beam model[47], [48], [58]. Fixed-free cantilever beams were easier to fabricate than doubly-clamped beams in our samples because they only require one fixed edge and our silicon support structures had very large openings. The fixed-free beam model also has an advantage over a doubly-clamped beam because it depends solely on bending instead of on bending and tension.

MFD is a technique for local measurements of Young's modulus that requires a complementary technique for locally measuring thickness. To take advantage of the local nature of the MFD method, it is necessary to know the thickness at the site of the cantilever. For example, the average thickness of Sample B was about 55 nm. However, the cantilevers we tested were in a much thicker region of the film, which we were able to measure with an optical transmittance technique to be about 160 nm (see Fig. 3-8). Uncertainty in thickness is the largest source of error in these measurements. With Young's modulus $E \propto t^{-3}$, the uncertainty from thickness is $\delta E = 3|E|\,\delta t/|t|$. Using relevant magnitudes and errors as an example, if $E = 500$ GPa, $t = 70$ nm, and $\delta t = 5\ nm$ then the uncertainty is $\delta E = 100$ GPa, giving a relative uncertainty of 20%. Other sources of uncertainty (and their relative errors) include cantilever width (1%), AFM tip stiffness (5%), AFM tapping mode deflection sensitivity (5%), and AFM lateral resolution (<1%).

The optical transmittance technique for estimating thickness of a MLG film is useful up to the resolution limit of the optical imaging system. With small cantilevers and sharp lines from wrinkles, diffraction plays a role and makes measuring the transmittance near the cantilevers or wrinkles difficult. Fig. 3-8(c) suffers slightly from these effects. For thicker films, the transmittance is very low and can be buried in the background noise (i.e. from extraneous light).

It is important to maximize the light transmitted through the film by ensuring that the intensity of the incident light is near the saturation limit of the detector. With a 14-bit sensor, the maximum measurable film thickness is $t = 25.856(1/\sqrt{1/2^{14}} - 1) \ = 3300\ nm$. Background noise effectively decreases the bit depth of the sensor. The average background noise for our images (approximately 380 ADC counts) decreased the maximum measurable thickness by just over 1%. This decrease is negligible because the measured thickness of our films was less than 200 nm. Other measurement techniques, such as spectroscopic ellipsometry and AFM step height measurements, are not feasible for measuring films thickness near the cantilevers.

The ion beam used to cut the cantilevers also caused changes to the surrounding film. This is evidenced by the large Raman D peak in the post-cut sample and by the lower contrast of the MLG near the cantilevers in the dark-field transmission images, both shown in Fig. 3-11. FIB cutting also requires careful alignment between the sample, the ion beam, and the electron beam. It is not possible to see through the MLG film with ion beam imaging in order to align the fixed edge of the cantilever to the silicon support edge, which is why alignment with the electron beam is necessary. Several samples had cantilevers that were too poorly aligned to be tested. It may be possible to protect the MLG film during FIB cutting by postponing the PMMA removal step until after the FIB process. PMMA is not electrically conductive, so a thin conductive layer, such as thermally evaporated carbon, could be deposited before processing in the electron microscope. Other methods for creating cantilevers in suspended thin films (or before the films are released) may reduce or eliminate both the challenge of alignment and of undesirable film modification. Optical or electron beam (e-beam) lithography are two such methods. Lithographically patterned films can be etched with wet or dry processes. Other work has shown that wet[59] and dry[43] etching methods can negatively impact graphene films, but not to the extent that we have seen with ion bombardment.

The multipoint force-deflection method for determining Young's modulus has several advantages over other techniques such as the single-point force-deflection method and bulge testing. First, by using multiple data points and fitting to a model, an independent measurement of the distance from the fixed end of the cantilever to the applied force is not necessary. This can simplify the measurement and remove one source of error. Second, MFD results give information about the boundary condition that can be used to justify or reject the model. MFD allowed us to differentiate between cantilevers with a well-defined fixed end and those without. Third, using MFD with microcantilevers allows for the measurement of local film properties in heterogeneous films, something that is not possible with bulge testing. We used the MFD method to determine the Young's modulus of many-layer graphene films with a large thickness non-uniformity to be (300 ± 20) GPa. This is approximately 30% of the Young's modulus reported for pristine graphene and pyrolytic graphite[49], which may be explained by ion-induced modification to the film during cantilever fabrication. The strength was also estimated to be (12 ± 2) GPa. The multipoint force-deflection method was shown to be well suited for measuring these non-uniform films.

3.6 Supplemental Material

See the supplemental material [in Appendix A] for a description of the many-layer graphene fabrication process, a brief discussion on the repeatability of MFD measurements, and information on exporting force-volume data from the NanoScope Analysis software.

3.7 Acknowledgments

We thank Paul Minson and Michael Standing of the BYU Microscopy Facility for their technical help with electron microscopy imaging and FIB cutting. We thank Brian Jensen for the discussion about beam equations and nonlinearity. We also thank Moxtek for initial project funding and for allowing us to use their facilities for fabrication of the many-layer graphene samples.

3.8 Author Declarations

3.8.1 Conflict of Interest

The authors declare no conflicts of interest.

3.9 Data availability statement

The data that support the findings of this study are available from the corresponding author upon reasonable request.

Chapter 4: Bioimpedance Plethysmography Sensitivity Modeling

4.1 Introduction

Plethysmography is used to measure the change in volume of some part or organ of the body. Photoplethysmography (PPG), where differences in transmitted or transflected light correspond to changes in blood volume, is a near ubiquitous feature of fitness trackers and many smartphones[60]. Impedance plethysmography (IPG)[15], [61], [62] correlates changes in bioimpedance to changes in blood volume, since blood has a different conductivity to surrounding tissue. During the cardiac cycle, an artery expands and contracts. This change is isolated near the artery, meaning plethysmography can be used to ignore the effect of tissue away from the artery. The ability of IPG to detect changes in blood volume depends on the location of the electrodes relative to the changing volume.

The ultimate goal of the bioimpedance research discussed in Chapters 4 and 5 is to develop the bioimpedance portion of a wearable non-invasive glucose monitor for the wrist. If IPG proves capable of being able to measure changes in blood, it will be possible to isolate those changes and measure only blood (and the tissue very near the artery). This could increase the sensitivity of any future impedance-based glucose monitor to arterial blood glucose, as opposed to glucose in the interstitial fluid. This may allow for more rapid detection of changes in glucose. In this chapter, I use finite element modeling to examine how shifting electrodes relative to the radial artery changes the sensitivity of the IPG. This modeling was performed in order to make predictions about sensitivity that were later tested during a human subjects study. Although the results of the human subjects study were inconclusive, the results of the modeling show that the IPG sensitivity to changes near the artery is greatly dependent on the location of the electrodes. The results in this chapter can guide future studies and electrode array design.

4.2 Methods

4.2.1 Four-electrode measurement

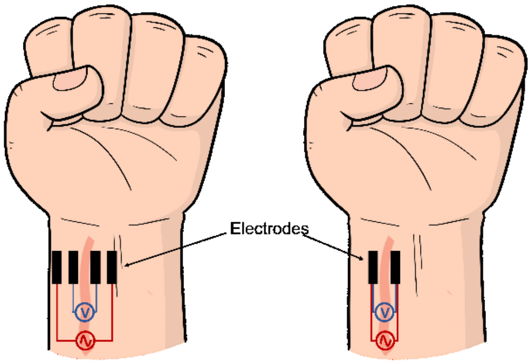

Fig. 4-1. Four-electrode versus two-electrode measurement system. The four-electrode system uses a dedicated pair of pickup (PU) electrodes, which can help reduce the effect of skin-electrode impedance on the measurement.

Bioimpedance is simply the ratio of voltage to current in biological tissue. Measuring bioimpedance requires at least two electrodes, but is commonly done with four electrodes. The two current carrying electrodes (called CC+ and CC-) are used to inject a known current (or apply a known voltage while current is measured elsewhere) while the two voltage pickup electrodes (called PU+ and PU-) are used to measure voltage (see Fig. 4-1). Because a voltmeter has a high input impedance, very little current flows through the voltage pickup electrodes. The skin-electrode impedance, or the impedance at the skin-electrode interface, is typically much higher than the internal tissue – especially for electrodes without a wet electrolyte (see Chapter 5). If very little current flows through the voltage pickup electrodes, then the impact of the skin-electrode impedance on that measurement will be minimal. We did not model skin-electrode impedance, so the values of impedance reported here will be much smaller than those reported in Chapter 5. However, we did use a four-electrode setup in the finite element model.

A four-electrode bioimpedance system can be considered a four-terminal or two-port network, where one port carries current and the other senses voltage (see Fig. 4-2). There are multiple impedances related to the two-port network, including the impedance looking into Port 1, the impedance looking into Port 2, and the transimpedance from Port 1 to Port 2. The transimpedance is defined as the ratio of the output voltage to the input current, or $Z = v/i$. When discussing bioimpedance from a four-electrode system, the transimpedance is often the impedance of interest. Transimpedance and bioimpedance (or just impedance) are frequently used interchangeably. We are interested in the plethysmographic, or pulsatile, nature of the transimpedance. The small change in impedance caused by the cardiac cycle is the pulsatile transimpedance and the baseline impedance is the static transimpedance. A practical measurement system would need to distinguish between the pulsatile transimpedance and the much larger static transimpedance.

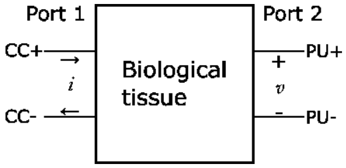

Fig. 4-2. Two-port (or four-terminal) network. Port 1 is for sourcing and sinking current and Port 2 is for measuring voltage. The transimpedance is defined as the ratio of the output voltage to the input current, $Z = v/i$.

4.2.2 Electrode array

In order to make predictions and compare results, the electrodes simulated here are modeled on the physical electrode array used in the human subjects study[20]. Fig. 4-3 shows the geometry of the electrode array and its orientation relative to the radial artery. The electrodes were 2 mm x 10 mm with a center-to-center distance (or pitch) of 2.5 mm. The electrode array was placed across the radial artery. The other direction (along the artery) typically has better sensitivity to the artery[63], but it is also less practical from a wearable standpoint. Although only four electrodes are needed to perform a four-electrode impedance measurements, an array of 16 electrodes allows for greater flexibility. With 16 electrodes and a method for electronically switching active electrodes, it is possible to shift the active electrodes without physically moving the electrode array. In the physical experiment, this helps alleviate the time-dependent skin-electrode impedance effects from physically shifting the electrode array. (See Chapter 5 for information on acclimation, or time-varying skin-electrode impedance.) The results reported here are with electrodes that have the same geometry as the physical electrode array; however, the results are applicable to more than just this one experiment.

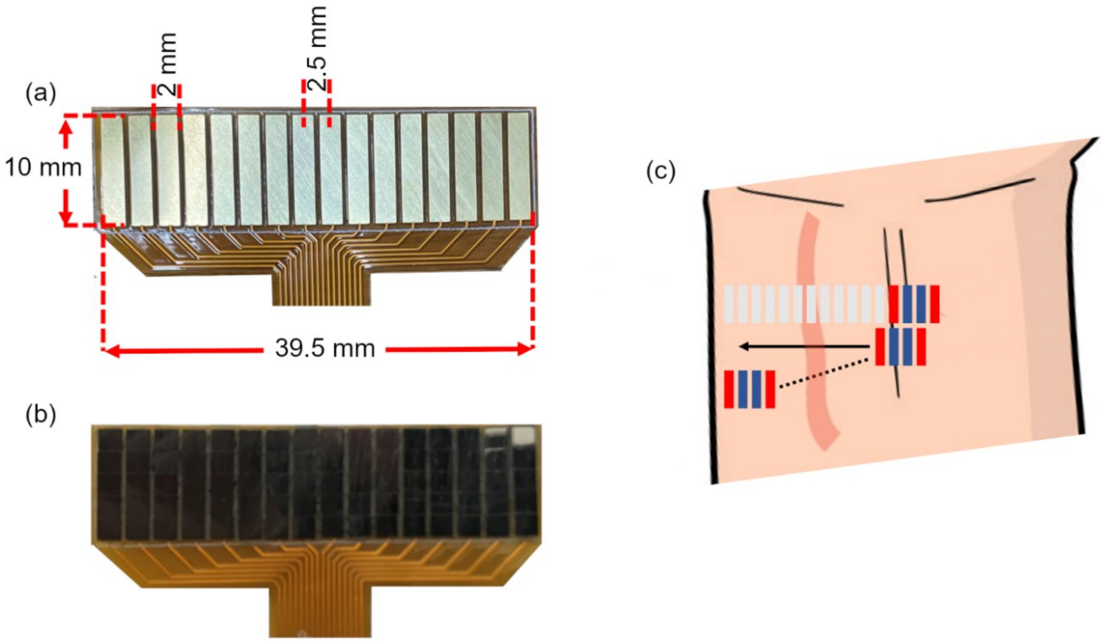

Fig. 4-3. The electrode array and its orientation on the wrist. (a) The manufactured electrode array consists of a flexible printed circuit board with gold-coated copper pads. (b) Carbon-infiltrated carbon nanotube electrodes attached to the gold pads with a conductive adhesive. (c) The orientation of the electrode array relative to the radial artery. The red are the current carrying electrodes and the blue are the voltage pickup electrodes. The active electrodes are shifted across the array (from right to left) without actually moving the array.

The selection of four electrodes (from the possible 16) limits the number of possible shifts. All electrode configurations in this study are in the form (order) of CC+, PU+, PU-, and CC- (see Fig. 4-3c, where the red electrodes are CC+/CC- and the blue electrodes are PU+/PU-). The electrode configuration is described by the current-to-voltage spacing (CV_s) and the voltage-to-voltage spacing (VV_s). This is CV_s $= 0$ and VV_s $= 0$ for Fig. 4-3c, where the zero indicates that there are no unused electrodes between the current and voltage electrodes or between the two voltage electrodes. Table 4-1 shows the total number of shifts ($n = 13$) and which electrodes are active during each shift for this same configuration. The shifts are numbered so that a shift of zero corresponds to the configuration being centered over the radial artery. Table

4-2 shows the total number of shifts ($n = 8$) for the configuration where CV_s = 1 and VV_s = 3.

Table 4-1
Active electrodes at all shift positions for the configuration where CV_s = 0 and VV_s = 0. Pink column is artery location.

	Electrode #															
Shift position	1	2	3	4	5	6	7	8	9	10	11	12	13	14	15	16
-5	CC+	PU+	PU-	CC-												
-4		CC+	PU+	PU-	CC-											
-3			CC+	PU+	PU-	CC-										
-2				CC+	PU+	PU-	CC-									
-1					CC+	PU+	PU-	CC-								
0						CC+	PU+	PU-	CC-							
1							CC+	PU+	PU-	CC-						
2								CC+	PU+	PU-	CC-					
3									CC+	PU+	PU-	CC-				
4										CC+	PU+	PU-	CC-			
5											CC+	PU+	PU-	CC-		
6												CC+	PU+	PU-	CC-	
7													CC+	PU+	PU-	CC-

Table 4-2
Active electrodes at all shift positions for the configuration where CV_s = 1 and VV_s = 3. Pink column is artery location.

	Electrode #															
Shift position	1	2	3	4	5	6	7	8	9	10	11	12	13	14	15	16
-3	CC+		PU+				PU-		CC-							
-2		CC+		PU+				PU-		CC-						
-1			CC+		PU+				PU-		CC-					
0				CC+		PU+				PU-		CC-				
1					CC+		PU+				PU-		CC-			
2						CC+		PU+				PU-		CC-		
3							CC+		PU+				PU-		CC-	
4								CC+		PU+				PU-		CC-

4.2.3 *Bioimpedance sensitivity field*

The sensitivity of a bioimpedance measurement is its ability to distinguish features in volumes of interest, while ignoring features elsewhere. Here, feature means either a static impedance or a dynamically changing impedance. A change in impedance will have a larger effect on the pickup voltage in a region of higher sensitivity. The sensitivity field can mathematically be defined using the volume under test and the placement/size of the electrodes. Specifically, it is the dot product of two current density fields[64, p. 166]:

$$S = \boldsymbol{J}'_{reci} \cdot \boldsymbol{J}'_{CC} \tag{4.1}$$

The reciprocal lead field ($\boldsymbol{J}'_{reci}$) and the current carrying lead field ($\boldsymbol{J}'_{CC}$) are the current densities that result from a unit current applied to the voltage pickup electrodes (for the reciprocal field) and the current carrying electrodes (for the current carrying field). The sensitivity field is highest when the two lead fields are parallel and lowest when they are orthogonal. With a two-electrode measurement, the two lead fields are identical, meaning they are always parallel. Therefore, the highest sensitivity occurs at the skin-electrode interface where the current density is highest. This is another reason why four-electrode measurements are preferred. With a four-electrode system, it may be possible to arrange the electrodes in such a way as to minimize the impact of undesired impedance, while maximizing the impact of the arterial impedance. The sensitivity is related to impedance by the general transfer impedance equation:

$$Z = \iiint \rho\, S\, dv = \iiint \rho\, \boldsymbol{J}'_{reci} \cdot \boldsymbol{J}'_{CC}\, dv. \tag{4.2}$$

There are two important consequence of (4.2) to keep in mind. First, regions with higher sensitivity will contribute more to impedance. Second, regions with negative sensitivity will contribute to impedance with an opposite sign. This means that there may be some configurations where a positive and negative sensitivity effectively cancel each other.

4.2.4 Finite element model

A finite element model (FEM) was created and analyzed using COMSOL Multiphysics 5.4. The model is a simplified two-dimensional cross-section of a circular wrist (see Fig. 4-4). One goal of this study was to determine how simple models could inform us of general trends in sensitivity to electrode placement. The model consists of multiple layers including skin, fat (adipose tissue), muscle, and bone. The artery is either embedded in the muscle layer (as pictured in Fig. 4-4) or in the fat layer (as pictured in Fig. 4-12). The relative permittivity and conductivity of tissue at various frequencies are taken from [64, p. 88] and [65] and are listed in Appendix B. Fig. 4-5 shows the conductivity (left axis; blue) and relative permittivity (right axis; orange) from 10 Hz to 10 GHz.

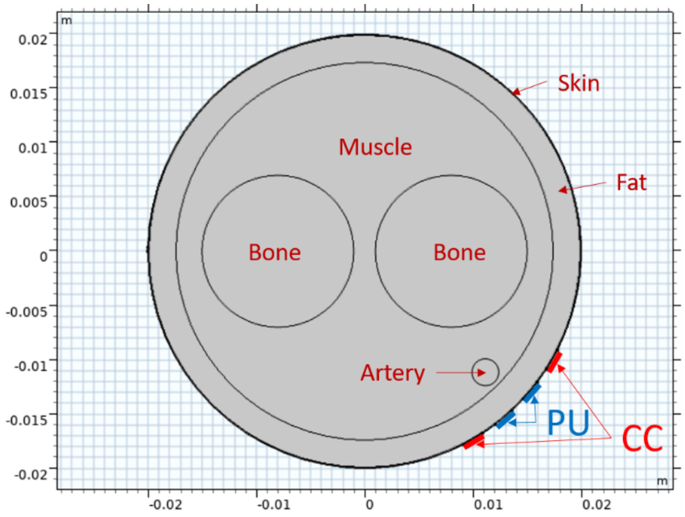

Fig. 4-4. Labeled description of the finite element model. The PU and CC electrodes are shifted along the circumference of the wrist and sensitivity to changes in the artery are recorded. This model was not developed for complex accuracy but instead for simplicity. The overall diameter of the wrist was 4 cm, with a skin thickness of 100 μm and a fat layer thickness of 2.5 mm. The artery had a diameter of 2.35 mm with a total pulsatile change of 10%.

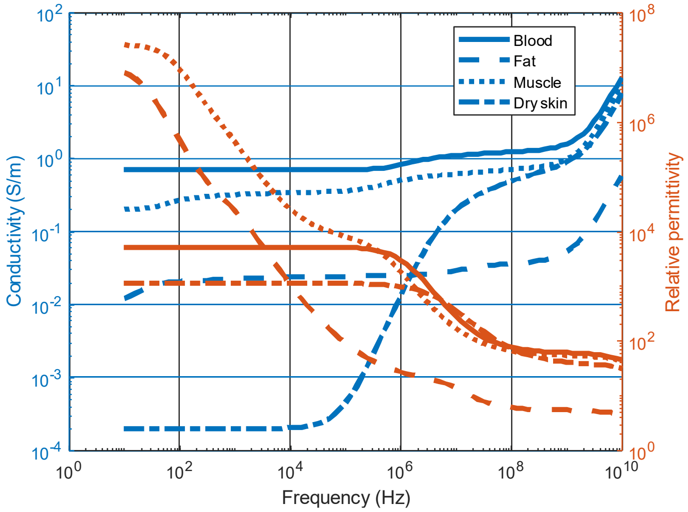

Fig. 4-5. Frequency dependence of conductivity (left axis; blue) and relative permittivity (right axis; orange). Of particular note is the conductivity of dry skin, which increases drastically with frequency. Figure produced with data from [65].

To model the pulsatile change, the finite element model was solved twice for each electrode configuration/placement (and frequency), with the artery diameter being the only difference. This represents a plethysmographic measurement where bioimpedance was measured during the systolic phase (larger artery diameter) and again during the diastolic phase (smaller artery diameter). A current (100 μA) was sourced from one CC electrode and sinked to the other. The pickup voltage, V_{PU}, was recorded as the potential difference from one PU electrode to the other. The pulsatile pickup voltage, or the difference between the pickup voltages for each artery diameter solution, is a proxy for sensitivity (not the sensitivity field):

$$\Delta V_{PU} = |V_{PU,sys} - V_{PU,dia}|. \tag{4.3}$$

By examining the sensitivity field and ΔV_{PU} for various electrode placements, it is possible to determine where (relative to the artery) the electrodes will be most sensitive to changes in the artery. Even though the sensitivity field gives insight into the interior of the wrist, the pulsatile pickup voltage, ΔV_{PU}, is convenient because it is the actual value that a practical measurement system would measure. (To be precise, a practical system measures $V_{PU,sys}$ and $V_{PU,dia}$.)

4.3 Results

4.3.1 Sensitivity

The sensitivity field, which is the dot product of the current density field (see Fig. 4-6) and the reciprocal current density field (see Fig. 4-7), highlights regions of greater sensitivity. The current densities are highest near the electrodes in Fig. 4-6 and Fig. 4-7. The sensitivity field falls off rapidly with distance from the electrodes as the current density spreads through the tissue. In Fig. 4-8, the sensitivity throughout the majority of the circular wrist is zero. Only near the electrodes is there a non-zero sensitivity. Both the current density field and the reciprocal current density field align near the artery, producing a region of higher sensitivity near the center of the electrodes. Fig. 4-8 also shows that there are regions of positive sensitivity and other regions of negative sensitivity. Negative sensitivity occurs when the angle between the current density and reciprocal current density fields is greater than 90°. With the pictured configuration of electrodes, this only occurs between the CC+ and PU+ electrodes and again between the PU- and CC- electrodes. Regions with negative sensitivity contribute to the transfer impedance with an opposite sign, which means we do not want the region of interest to have both positive and negative sensitivities.

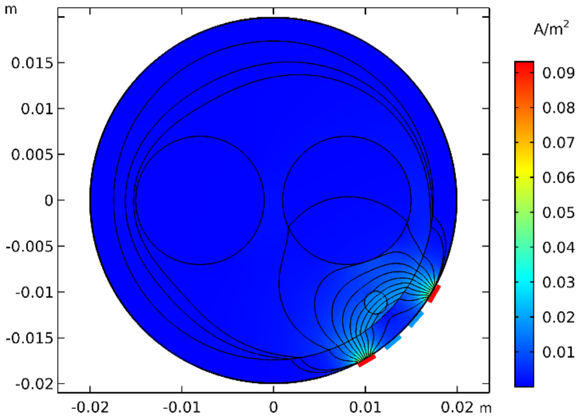

Fig. 4-6. Current density field (also called lead field). The current carrying electrodes are red and the voltage pickup electrodes are blue.

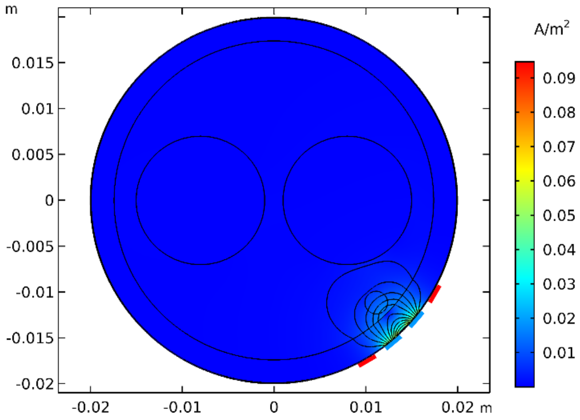

Fig. 4-7. Reciprocal current density field (also called reciprocal lead field).

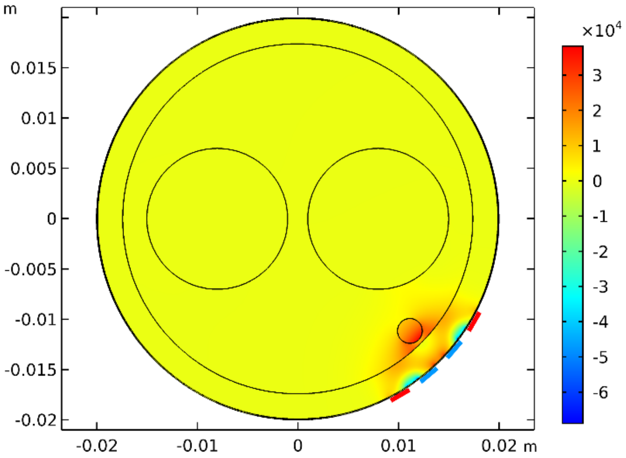

Fig. 4-8. Sensitivity field. The sensitivity field is the dot product of the fields in Fig. 4-6 and Fig. 4-7. The units are $1/\mathrm{m}^4$. The majority of the circular wrist has near-zero sensitivity, meaning it would contribute very little to the measured impedance with the present configuration of electrodes.

4.3.2 Shifting electrodes

The finite element model (FEM) was solved for many different electrode configurations. Each configuration was shifted along the skin relative to the artery. Fig. 4-3c shows how the electrode array with configuration $\mathrm{CV\_s} = 0$ and $\mathrm{VV\_s} = 0$ shifts from the right to the left. This is again shown in Table 4-1 (though this time from left to right). Fig. 4-9 shows the finite element results of the current density for this same configuration as it shifts relative to the artery. At each position, the FEM was solved for both the systolic and diastolic phases. As described previously in (4.3), $\Delta\mathrm{V}_{PU}$ is the difference in pickup voltage between these two phases. Fig. 4-10 shows the $\Delta\mathrm{V}_{PU}$ at each of the shift positions for all of the configurations.

The highest sensitivity to changes in the artery (which is ΔV_{PU}) occurs near the centerline of each electrode configuration (see Fig. 4-10). The shifts are numbered so that a shift of zero corresponds to the configuration being centered over the radial artery. Each configuration has a different number of total shifts that are available, depending on the total number of electrodes between CC+ and CC-. For a practical application such as a wearable, the most desirable configuration would not only have the highest ΔV_{PU}, but it would also have the widest range of high sensitivity. It would be undesirable for the sensitivity to drop drastically for small movements, as a wristband slides and shifts on the wrist. The top right panel in Fig. 4-10 has the broadest and second highest ΔV_{PU} profile. The maximum ΔV_{PU} is about 2 µV. This results in a pulsatile transimpedance of $Z = 2\ \mu\text{V}/100\ \mu\text{A} = 20\ \text{m}\Omega$. From (4.3), ΔV_{PU} is the difference of the pickup voltages during the systole and the diastole. Both $V_{PU,sys}$ and $V_{PU,dia}$ are approximately 2 mV, which is three orders of magnitude larger than their difference. The static transimpedance is then $Z = 2\ \text{mV}/100\ \mu\text{A} = 20\ \Omega$.

Each configuration was also solved for multiple frequencies from 1 kHz to 10 MHz. The results indicate that ΔV_{PU} is lower for higher frequencies (see Fig. 4-10). In the best case (top right panel), the sensitivity drops from about 2 µV for 1 kHz to about 0.5 µV for 10 MHz. This may be caused by more current flowing through the skin as opposed to the rest of the tissue, since the conductivity of dry skin increases with frequency. Further modeling needs to be done to determine if this is indeed the case.

We also explored how changing the fat layer thickness might affect ΔV_{PU}. Fig. 4-11 shows that when the fat layer is large enough to encompass the artery (“large fat layer”), not only is ΔV_{PU} much higher, but it also has a different shape. The 16 electrode array was not large enough to capture the full profile of ΔV_{PU} for all configurations, but two peaks are visible in most panels of Fig. 4-11. It appears that the sensitivity is highest when either CC electrode is under the artery, resulting in the two distinctive peaks. Fig. 4-12 and Fig. 4-13 show that the sensitivity with the electrode array centered under the artery is less than the sensitivity when the CC electrode is under the artery. This is contrary to Fig. 4-8, where the highest sensitivity at the artery occurs when the electrode array is centered under the artery. The current density plots of Fig. 4-14 and Fig. 4-15 show why this is the case. The current through the artery when the electrode array is centered over the artery is much less in Fig. 4-14 than in Fig. 4-6. The conductivity of fat is much less than that of muscle, so the current does not tend to spread in the fat layer. This keeps the current concentrated above the current carrying electrodes.

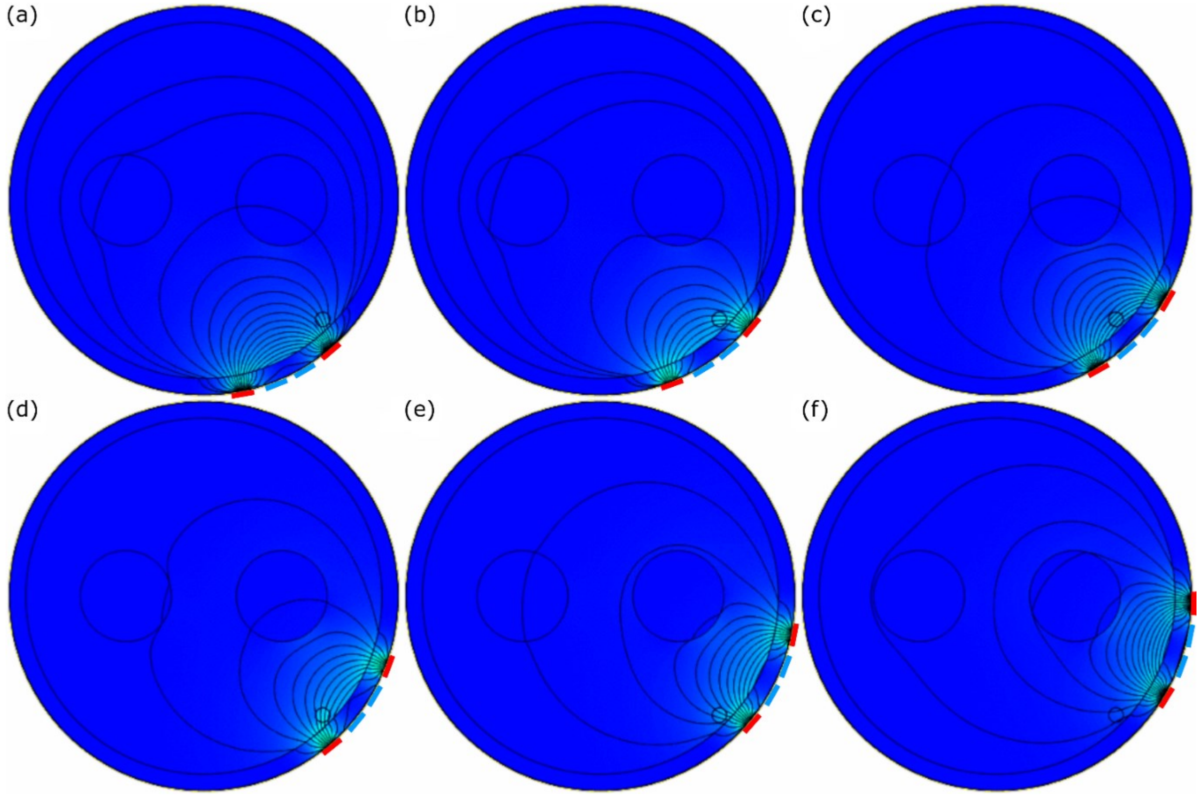

Fig. 4-9. Stills from an animation showing current density as the electrodes are shifted relative to the artery. The diameter of the circular wrist in this figure is not the same used elsewhere; however, the purpose of this figure is to show how the electrodes shift relative to the artery so the exact geometry is less important.

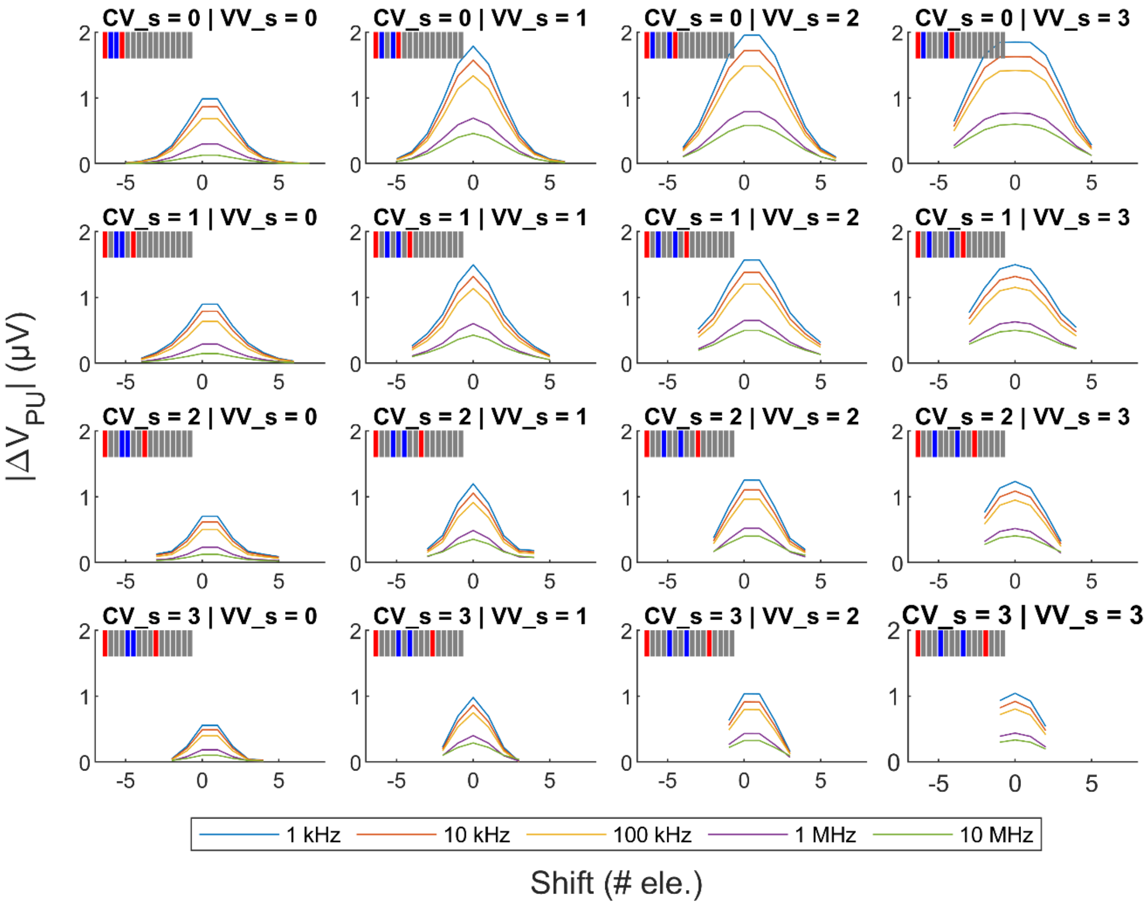

Fig. 4-10. The pickup voltage (ΔV_{PU}) at multiple frequencies for several electrode configurations as the electrodes are shifted relative to the artery. Higher values of ΔV_{PU} indicate a higher sensitivity to changes in the radial artery. The ideal profile would be broad and high, such as the top right corner. Each panel also shows which of the 16 electrodes are used (with red for CC and blue for PU). The pictured active electrodes correspond to the left most shifted position. The profile is built up by shifting the active electrodes until the rightmost active electrode is at the rightmost electrode position. In general, higher frequencies have a lower ΔV_{PU}.

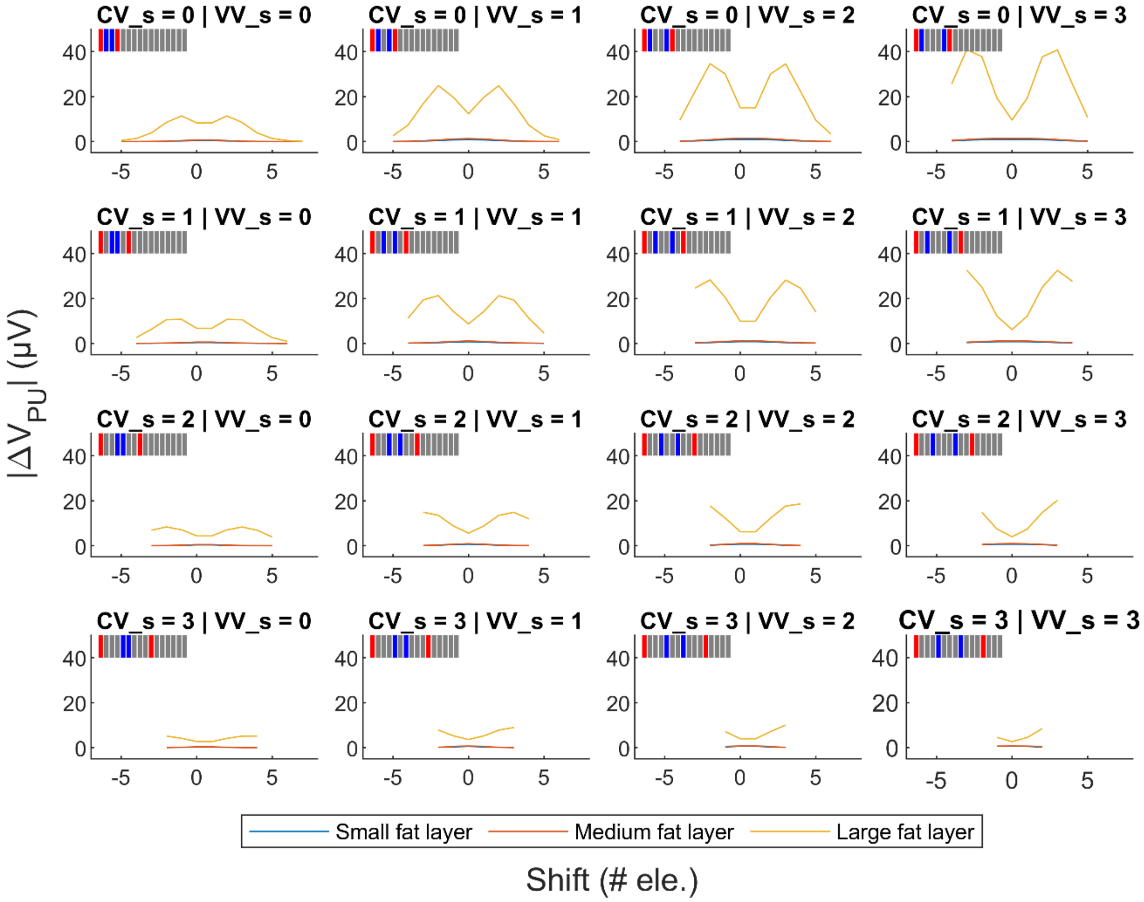

Fig. 4-11. The pickup voltage (ΔV_{PU}) for three different fat layer thicknesses and several electrode configurations as the electrodes are shifted relative to the artery. The medium fat layer is the standard thickness ($t = 2.5$ mm) used for all other results. The small fat layer is about half the thickness of the medium layer, while the large fat layer is about twice the thickness of the medium layer. The large fat layer encompasses the artery, meaning there is no abrupt fat-to-muscle transition before the current reaches the artery.

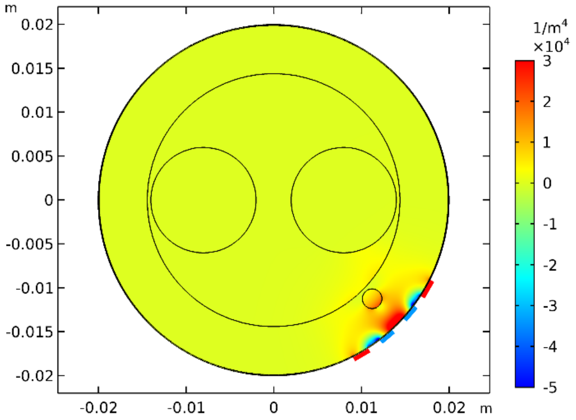

Fig. 4-12. Sensitivity field with large fat layer when electrodes are centered under the artery. The magnitude of the sensitivity field is lower in the artery compared to Fig. 4-13.

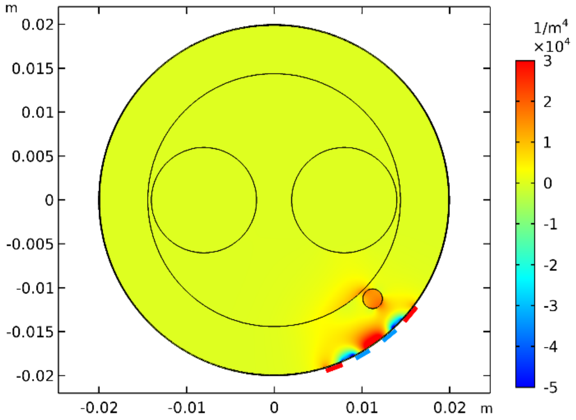

Fig. 4-13. Sensitivity field with large fat layer when the current carrying electrode is under the artery. The magnitude of the sensitivity field is higher in the artery compared to Fig. 4-12.

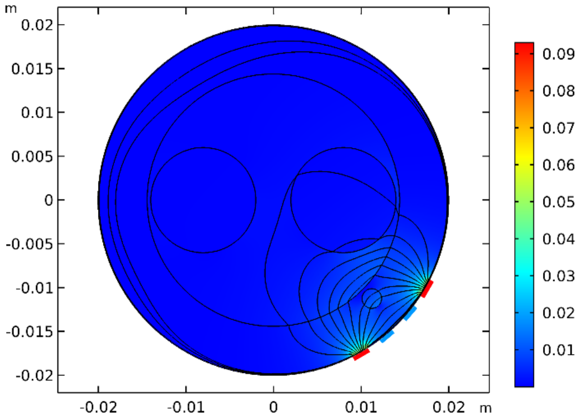

Fig. 4-14. Current density with large fat layer when electrodes are centered under the artery. Fewer current field lines pass through the artery compared to Fig. 4-15.

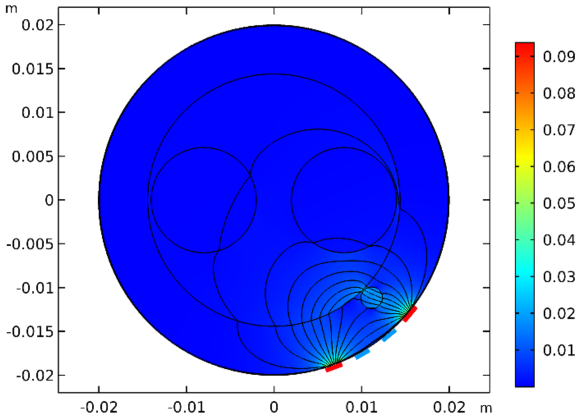

Fig. 4-15. Current density with large fat layer when the current carrying electrode is under the artery. Notice how there are many more current field lines through the artery than in Fig. 4-14.

4.4 Discussion

The current density field and sensitivity field results highlight a major difficulty in using small electrodes. As the electrode area decreases, the current density at the skin-electrode interface increases (assuming current stays the same). Because sensitivity is highest when current density is highest, this means that the sensitivity near the electrodes increases. This is especially relevant for two-electrode bioimpedance measurements, but is only partially alleviated with a four-electrode measurement (and less so for four-electrode systems with tightly packed electrodes).

The large fat layer has a different sensitivity profile compared to the small and medium fat layers (see Fig. 4-11). For the models with the large fat layer, the highest sensitivity occurs when the current carrying electrodes are under the artery (see Fig. 4-13 and Fig. 4-15 compared to Fig. 4-12 and Fig. 4-14). This gives two distinct peaks in Fig. 4-11. For the models with the small and medium fat layers, the highest sensitivity occurs when the electrode array is centered under the artery (see Fig. 4-8). The single centralized peak that results can be seen in Fig. 4-10. The reason two distinct peaks arise in the sensitivity profile for the large fat layer can be seen by comparing Fig. 4-14 and Fig. 4-6. The conductivity of muscle is much higher than the conductivity of fat, which means that the current density does not tend to spread in the fat layer, “preferring” the shorter electrical path of the muscle layer. A physical wrist is much more complicated than either model. The transition between biological material is not as sharp, but the artery is surrounded by a heterogeneous assortment of muscle fibers, ligaments, fat, interstitial fluid, etc. It is reasonable to assume that the actual sensitivity would be a mixture of the two behaviors seen here.

The modeled pulsatile transimpedance for the best-case scenario in Fig. 4-10 is approximately 20 mΩ. This is on top of the static transimpedance of about 20 Ω. A practical measurement system would need the ability to measure 20 Ω with enough resolution to distinguish changes smaller than 20 mΩ. The situation is compounded when considering skin-electrode impedance. Skin-electrode impedance can add hundreds to thousands of ohms to the static transimpedance. For example, see Fig. 5-11 for the acclimated two-electrode skin-electrode impedance as a function of frequency and electrode area. In short, measuring the pulsatile transimpedance in reality (with enough resolution to distinguish cardiac features) is not trivial, but is feasible with a well-designed system.

This modeling was performed in anticipation of a human subjects study at Brigham Young University (IRB #F2020-268). We predicted that the largest pulsatile signal would be seen when the two pickup electrodes in the electrode array were centered over the radial artery. If instead the results of the human subjects study showed peaks in the pulsatile signal when the current carrying electrodes were over the artery, then that would indicate a closer affinity to the "larger fat layer" in Fig. 4-11. The results of the human subjects study are reported by Diego Leon [20]. Unfortunately, the measurement system was not able to record a pulsatile signal for the majority of participants and therefore no conclusions could be drawn to support or reject this model. However, the results of this modeling could still be used to guide future experiments. For example, a two-electrode system would have the highest sensitivity near the electrodes, since (4.1) would just become $S = |J|^2$. We have also seen from Fig. 4-10 that the sensitivity decreases with frequency and, therefore, higher frequency systems may be less sensitive to changes in the artery.

Another application of this modeling work is in the utility of a multi-electrode array in combination with other sensors on a wrist-based wearable. It would be impractical to have multiple copies of expensive sensors (such as a short-wave infrared spectrometer). A user might have difficulty aligning other sensors over the artery, where their sensitivity is greatest. The electrode array could be used to guide a user, telling them to rotate the band (using feedback from the impedance system) until the other sensors aligned with the artery.

4.5 Conclusion and Future Work

The modeling presented in this chapter showed how it is possible to use finite element analysis to model a simplified wrist and make predictions about how real electrodes might behave on an actual wrist. The model consisted of a circular 2-dimensional wrist, with simplified layers of skin, fat, muscle, bone, and blood. The electrodes were modeled after an electrode array that was used in a human subjects study. The electrodes were shifted relative to the radial artery and the pulsatile pickup voltage (ΔV_{PU}) was recorded. We also examined the sensitivity field, which showed increased sensitivity near the artery. We predicted that the pulsatile signal would be higher when centered over the artery. Unfortunately, the human subject study was inconclusive. Despite this, the model gives insight into how sensitivity depends on electrode positions. This insight can be used to guide both future modeling and experimental work.

Future work is needed on both the model and the measurement system. The model's simplified stacking of skin, fat, and muscle layers has led to confusion about whether the sensitivity is highest near the current carrying electrodes or in the center of the pickup electrodes. A more complicated, anatomically correct model could be built from MRI or CT data[63]. This model should also be 3-dimensional, which would allow for an exploration of different electrode areas and alternative orientations. The measurement system current was limited to 100 μA, when in reality higher frequency systems can safely use up to 10 mA. A new measurement system should be designed to respect the frequency-weighted current limit.

Chapter 5: Bioimpedance Human Subjects Acclimation Study

Authors: Kyle G. Larsen, Diego A. Leon, Nicholas E. Allen, Evan Dodson, Richard R. Vanfleet, Brian D. Jensen, and Robert C. Davis

5.1 Abstract

Bioimpedance measurements are often performed using relatively large electrodes with a wet electrolyte. However, dry electrodes are more feasible than wet electrodes for long-term wearable applications. One of the major difficulties with dry electrodes is that the skin-electrode impedance changes as the skin-electrode interface changes (e.g. due to skin hydration), which leads to an acclimation period when electrodes are first placed on the skin. In this work, we used microfabricated carbon infiltrated-carbon nanotube electrodes to measure the change in skin-electrode impedance for millimeter-scale dry electrodes, and identical electrodes with a wet electrolyte, on five human subjects in the range of 1 kHz to 100 kHz. We found that the skin-electrode impedance of the dry electrodes approached that of the wet electrodes after a period of acclimation, especially for electrodes with larger areas. We fit the time dependent skin-electrode impedance to a power law and defined acclimation time as the time needed for the skin-electrode impedance's rate of change to drop to 1% of the original rate. The average acclimation time was 32 minutes. We found that the acclimation time does not appear to depend on electrode area or frequency. The skin-electrode impedance after acclimation does depend on electrode area and frequency, decreasing with both. After acclimation, the skin-electrode impedance magnitude at 10 kHz ranged from 110 kΩ for the smallest electrodes (2 mm x 2 mm) to 10 kΩ for the largest (2 mm x 16 mm).

5.2 Introduction

Wearable bioimpedance-based devices can be used to continuously and non-invasively monitor human physiological parameters including heart rate, respiration rate, skin hydration, blood pressure, and blood glucose[15], [19], [61], [66]–[69]. The bioelectrical impedance (or simply bioimpedance) of tissue can be measured by passing current into the tissue and measuring the resulting voltage drop. Such a system requires at least two electrodes. Wet contact electrodes (those with a wet electrolytic gel) are commonly used in clinical and research settings; however, for a wrist-based wearable device, the electrodes must remain in contact with the skin for extended periods of time. Bioimpedance measurements with dry contact electrodes are often dominated by the skin-electrode impedance, which includes the electrode resistance, the contact impedance, and the impedance of the skin[70]. A large skin-electrode impedance will tend to decrease the quality of the measured signal[71], [72]. Various techniques exist for decreasing skin-electrode impedance, including increasing electrode area, increasing the skin-electrode pressure[73], and abrasive skin preparation[74], [75]. Each technique has its limits in a wearable application: electrode area is constrained by the band size, excessive band pressure is uncomfortable[76], and long-term repeated skin abrasion is infeasible. Additionally, changes to the skin-electrode interface (e.g. from skin deformation, hydration variation, or movement) will cause corresponding changes to the skin-electrode impedance. Of particular interest is the initial skin-electrode impedance variation that occurs when dry contact electrodes are first placed on the skin.

After dry contact electrodes are first placed on the skin, there is an acclimation period during which the skin-electrode impedance changes rapidly [62], [70], [77], [78]. The skin-electrode impedance is greatly affected by the skin condition (particularly moisture/sweat) for electrodes that do not provide an electrolyte[70]. In many studies using dry electrodes, the measurements are performed after the acclimation period. However, in a wearable application, the device may shift at any time causing the electrodes to relocate to a new region of skin. Understanding this acclimation behavior may allow the device to record meaningful data even during the acclimation period. In order to study this effect for small electrodes suitable for long-term wearable applications, we measured the skin-electrode impedance for one hour using two sets of electrodes. The electrodes were identical except that one set had an electrolyte gel applied at the skin-electrode interface. We designed a multiplexer that would allow for electronic switching of the active electrodes, in order to facilitate measurements of both dry and wet electrodes concurrently. We found that the skin-electrode impedance typically dropped by a factor of 3 to 5 during the acclimation period, which lasted for about 30 minutes. Skin-electrode impedance decreases with increasing electrode area and is significantly lower and more stable for electrodes with a wet electrolyte, as expected. After acclimation, the skin-electrode impedance magnitude at 10 kHz ranged from 110 kΩ for the smallest electrodes (2 mm x 2 mm) to 10 kΩ for the largest (2 mm x 16 mm).

5.3 Methods

5.3.1 Measurement of Skin-electrode impedance

We used a multi-frequency impedance analyzer (MFIA, Zurich Instruments, Zurich, Switzerland) in a two-terminal setup for measuring bioimpedance from 1 kHz to 5 MHz. A two-terminal system measures the skin-electrode impedance in addition to the impedance of the internal tissue (see Fig. 5-1). For low frequencies, the two-terminal impedance is dominated by the skin-electrode impedance. For this reason, we will ignore the internal tissue impedance and refer to the two-terminal impedance as the skin-electrode impedance. Skin-electrode impedance was measured over time for several pairs of electrodes in a 16 electrode array. The impedance analyzer also has two auxiliary inputs that were used for two pressure sensors.

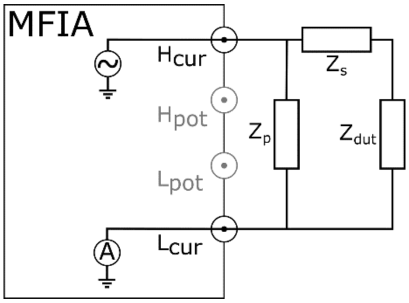

Fig. 5-1. The impedance analyzer was used in a two-terminal configuration. The measured impedance included both the series (Z_s) and parallel (Z_p) system impedances (e.g. from cabling, safety resistors, and PCB trace capacitance). These would later be removed via compensation to yield the impedance of the device (or tissue) under test, Z_{dut}.

The impedance analyzer can only be connected to one set of electrodes at a time. However, our experiment required the system to rapidly switch between the different pairs of electrodes to measure the skin-electrode impedance of the wet and dry electrodes concurrently. We accomplished this with two separate 16:2 channel multiplexers (MAX14661, Maxim Integrated, San Jose, CA, USA) integrated in parallel on a printed circuit board. The multiplexers allowed us to connect any of the 16 electrodes on our electrode array to any of the four channels of the impedance analyzer. The multiplexers were controlled via I2C from a WiFi-enabled microcontroller (ESP-01, Espressif Systems, Shanghai, China). Because the multiplexer is capable of selecting different electrodes, it is possible to shift which electrodes are active. In this way, it is possible to measure different parts of the wrist without removing the electrodes from the skin. See Appendix D for additional details on the multiplexer board. The impedance analyzer and multiplexer board were controlled using a laptop running MATLAB R2019a. The system was able to capture a complete spectrum of 100 points spaced logarithmically from 1 kHz to 5 MHz in approximately 300 ms.

5.3.2 Electrode Arrays

Bioimpedance measurements are typically facilitated by larger electrodes; however, our goal of integrating into a wearable with other sensors limits the size of electrodes we can use. In this study, we used electrode sizes that would fit in a typical watchband: 2 mm x 2 mm, 2 mm x 4 mm, and 2 mm x 16 mm rectangular electrodes (see Fig. 5-2). The width of the electrode array was designed to be narrow enough so that the majority of the electrodes fit on the wrist in between the tendon and radial bone. Each electrode array consists of two rows of eight electrodes. In order to study the difference between wet contact and dry contact electrodes, one row was prepared with an electrolyte (Spectra 360 Electrode Gel, Parker Laboratories, Fairfield, NJ, USA) while the other was left dry (see Fig. 5-3). Only two of the electrodes in either row are used at a time. The multiplexer allows for switching which electrodes are active without displacing the electrode array.

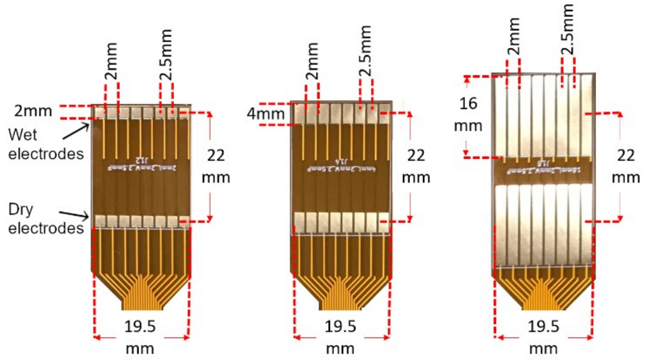

Fig. 5-2. The bare flexible printed circuit boards of the three differently-sized electrode arrays. The sizes of the electrodes in each array are (from left to right) 2 mm x 2 mm, 2 mm x 4 mm, and 2 mm x 16 mm.

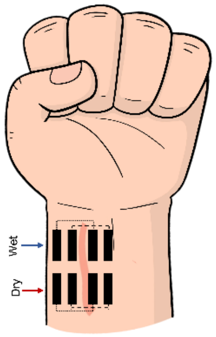

Fig. 5-3. The wet contact electrodes (top) and dry contact electrodes (bottom). In reality, each row has 8 electrodes, all connected to a multiplexer that can select any two electrodes to be active at once. One row was measured at a time, with the multiplexer rapidly alternating between rows to give the appearance of simultaneous measurement.

The electrodes were made using carbon-nanotube-templated microfabrication (CNT-M)[19], [20], which allows for precision fabrication of conductive and chemically stable carbon material. The CNT-M process consists of growing forests of vertically aligned carbon nanotubes that act as a framework for a carbon infiltrant, thereby creating a solid carbon composite. The electrodes can be fabricated with a lateral precision of a few microns and a vertical height of several hundred microns. This height allows the electrodes to apply local pressure to the skin and therefore helps ensure good contact. The electrodes used in this research had a height of approximately 500 µm and were grown in 2 mm x 2 mm square segments that were assembled to create the larger electrode sizes (see Fig. 5-4). Carbon electrodes are conductive and chemically inert[81], [82]. They can easily be cleaned with isopropyl alcohol. After fabrication, the electrodes were transferred to a flexible printed circuit board (FPCB) with exposed gold pads in the desired electrode array pattern. The electrodes were attached to the gold pads with an anisotropic conductive film (3M 7303, Saint Paul, MN, USA). Fig. 5-4 shows the final CNT electrodes attached to the FPCB used in this study.

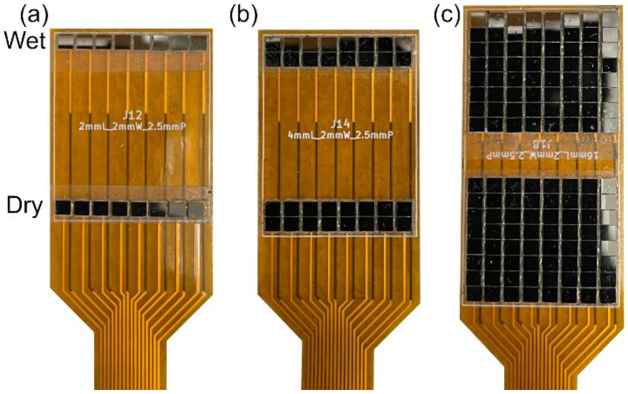

Fig. 5-4. Carbon nanotube electrode arrays. The sizes of the electrodes in each array are (from left to right) 2 mm x 2 mm, 2 mm x 4 mm, and 2 mm x 16 mm. Each flexible circuit board contains two electrode arrays (top and bottom), where one had an electrolyte gel applied, and the other did not.

An additional benefit of having multiple electrodes in each array is that we can use the multiplexer to electronically shift electrodes to measure adjacent regions. In this way it is possible to record the skin-electrode impedance of multiple electrodes or switch between two-terminal and four-terminal measurements. Although the system (impedance analyzer and multiplexer) are capable of measuring both two- and four-terminal setups, only the two-terminal configuration is used in this study.

5.3.3 Wristband

The electrode arrays were mounted in an electrode array holder (EAH). The EAH was held against the wrist using a ratcheting strap with dimples for a post on the top of the EAH. The EAH had two integrated force sensors (S8-10N, SingleTact, Glasgow, UK) capable of measuring the pressure under each row of the electrode array in order to compare pressure between the wet and dry electrodes. See Appendix D for more information on the wristband and EAH.

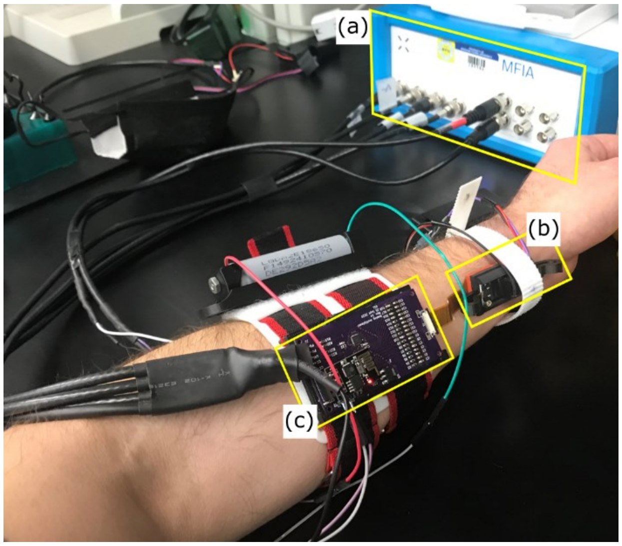

Fig. 5-5. Measurement setup with electrode array and multiplexer board on the wrist/forearm. The impedance analyzer (a) and the multiplexer board (c) are capable of measuring impedance with either two or four electrodes, though in this experiment only the two-electrode configuration was used. The electrode array holder and the wristband (b) secure the electrodes to the wrist.

5.3.4 Human Subject Testing and Experimental Procedures

Five individuals participated in this study with approval from the institutional review board at Brigham Young University (IRB #F2020-268). The participant information is shown in Table 5-1. Each participant came in for three two-hour sessions. The same procedure was performed during each session, with a different electrode array size used each time. The procedure followed for each session is explained below and has been divided into three subsections: pressure setting, acclimation study, and variation study.

Table 5-1
Participant information

ID	Sex	Age	Weight (kg)	Height (m)	BMI
1	Male	22	58.5	1.75	19.0
2	Female	21	76.0	1.67	27.1
3	Male	27	122.5	1.95	32.0
4	Male	19	73.5	1.80	22.6
5	Female	22	58.9	1.60	23.0

5.3.4.1 Pressure Setting

At the beginning of each session, before starting to record the impedance data, we placed the EAH on the wrist of the participant centered on their radial artery. The band was placed around the wrist, with the buckle on the front of the wrist. We fit the EAH post to one of the dimples on the inner face of the band and tightened the band until we reached a pressure from 10 kPa to 15 kPa for both pressure sensors. The notch to which the band was tightened was marked for reference, so that the band could be restored to the same position. The band and EAH were then removed from the wrist and a thin layer of electrolyte gel was applied to the wrist to correspond to the position of the top row of electrodes. The EAH was then replaced in the same position, with care taken to ensure the bottom row of electrodes (dry electrodes) did not come in contact with the gel on wrist. The band was tightened to the previously selected notch. The participant then found a comfortable position they could maintain with minimum movement for up to 90 minutes.

5.3.4.2 Acclimation Study

The acclimation study consisted of recording the skin-electrode impedance spectra of the wet and dry electrodes over a period of approximately 60 minutes to determine how skin-electrode impedance changes with time. The impedance was measured using the aforementioned impedance analyzer and multiplexer board, and then saved for later processing. Impedance spectra were alternately recorded for two electrodes from the dry array and then two different electrodes from the wet array, a process that was repeated for approximately 60 minutes. These same pairs of electrodes were used through the acclimation study.

5.3.4.3 Variation Study

The variation study started after recording the skin-electrode impedance acclimation for 60 minutes. The purpose of this section of the procedure was to determine how skin-electrode impedance differs for electrodes that were not carrying current during the acclimation study (but were in contact with the skin) and to measure the skin-electrode impedance variation after removing and replacing the electrode array. After the acclimation portion of the study, the multiplexer was used to electronically switch the active electrodes (in both wet and dry rows) to an adjacent set of electrodes 2.5 mm to the right. Impedance spectra were recorded for both wet and dry electrodes. The process was repeated for a set of electrodes 2.5 mm to the left of the original electrodes and then again using the original set of electrodes (called middle). Fig. 5-6 shows the three electrode positions: left, right, and middle (original). The wristband was then removed from the participant. After five minutes it was replaced (to the same position) and impedance spectra were recorded for the right, left, and middle, positions again (for both wet and dry electrodes). The process of removing, waiting five minutes, replacing the band, and recording the impedance spectra was repeated once more. The instrumentation was removed from the participant and the session was concluded.

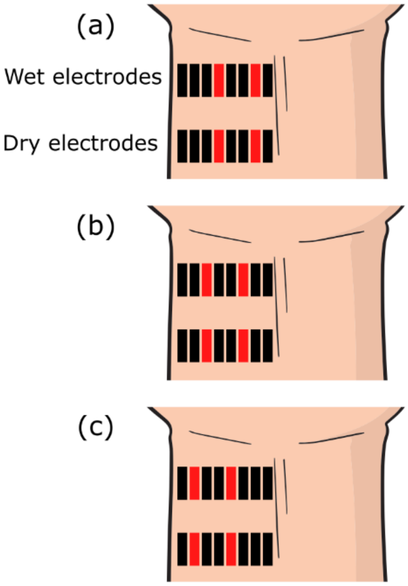

Fig. 5-6. Active electrodes (in red) for both the wet (top row) and dry (bottom row) electrodes. (a) Active electrodes are one position to the right of the original (middle) electrodes. (b) The (middle) electrodes used during the acclimation study. (c) Active electrodes are one position to the left of the original (middle) electrodes.

5.3.5 Compensation

The measured impedance values must be compensated in order to remove the effects of the measurement system. An open/short compensation was performed by calculating the open and short circuit impedances and removing their effects with (5.1).

$$Z_{dut} = \frac{(Z_{meas} - Z_{short})\, Z_{open}^2}{(Z_{open} - Z_{meas})(Z_{open} - Z_{short})} \tag{5.1}$$

Eq. (5.1) was derived using the model shown in Fig. 5-1. Because the impedance analyzer is attached to the body using cables and a multiplexer, the measured impedance (Z_{meas}) is not just the body/tissue impedance. The model contains series impedance (Z_s) and parallel impedance (Z_p), in addition to the impedance of the device or under test (Z_{dut}). By replacing Z_{dut} with either a short or open, we can measure Z_{short} and Z_{open}. With our model, $Z_{short} = Z_p || Z_s$ (Z_p in parallel with Z_s) while $Z_{open} = Z_p$. The series impedance (Z_s) is almost exclusively from a series safety resistor on the multiplexer board (20 kΩ). The parallel impedance (Z_p) is primarily due to parasitic capacitance on the multiplexer board (about 40 pF). This capacitance limits the high frequency results from the impedance analyzer, which allows us to use the data above 500 kHz to estimate Z_{open} (by fitting Z_{meas} above 500 kHz to a capacitor). Because we can estimate $Z_{open} = 40\text{ pF}$ and $Z_{short} = 40\text{ pF}||20\text{ k}\Omega$, we did not perform separate open and short circuit measures on the study participants.

5.3.6 Acclimation Time

Acclimation time is the time for the skin-electrode impedance to stop changing rapidly. It is possibly affected by electrode area, frequency, skin hydration, and band pressure, among other factors. To determine acclimation time, we fit the compensated skin-electrode impedance magnitude to a power law,

$$Z = a * t^b + c. \tag{5.2}$$

Acclimation time was then defined as the time for the change in impedance to be 1% of the change at the initial time.

$$\frac{dZ}{dt} = a * b * t^{b-1} \tag{5.3}$$

$$\frac{dZ/dt|_{t=t_f}}{dZ/dt|_{t=t_i}} = 0.01 = \frac{t_f^{b-1}}{t_i^{b-1}} \tag{5.4}$$

$$t_f = \left(0.01 * t_i^{b-1}\right)^{1/(b-1)} \tag{5.5}$$

Eq. (5.5), gives the acclimation time ($t_{acc} = t_f$) as a function of the initial time (t_i) and b, the exponent of the power law in Eq. (5.2).

5.4 Results

5.4.1 Pressure

Pressure was recorded at the beginning of each session in order to properly tension the wristband. Table 5-2 contains the pressure (in kPa) for each participant and electrode array size. A pressure sensor was integrated behind both the wet and dry electrode rows in order to ensure an even pressure across the band. Participant 1 had a small wrist with predominant bones and tendons. In order to make sufficient contact between the electrodes and the skin, the band was tightened more than for the other participants but still within the tolerance level of participant 1. The pressure was not always consistent between the wet and dry electrodes. This is most likely due to participants flexing their wrist or the band exerting a lateral force on the electrode array holder. All pressures were within a safe and comfortable range. The pressure sensor under the wet electrode row became disconnected during the session where participant 4 was using the 2 mm x 16 mm electrode array, and so no data was recorded.

Table 5-2
Electrode array pressure (in kPa)

	2 mm x 2 mm		2 mm x 4 mm		2 mm x 16 mm	
Participant	Dry	Wet	Dry	Wet	Dry	Wet
1	27.7	24.0	28.8	33.8	25.2	28.9
2	13.0	14.2	12.4	6.8	6.6	10.3
3	10.5	11.7	8.9	10.7	15.7	15.4
4	11.3	9.1	9.7	10.9	13.9	—
5	11.0	6.1	15.0	4.1	9.8	11.4

The effects of electrode size and electrolyte presence on the skin-electrode impedance were found to be more significant than the effects of pressure. Fig. 5-7 shows the measured skin-electrode impedance over time for four different cases. The blue and orange data is the skin-electrode impedance for the same electrode size (2 mm x 4 mm), but with drastically different pressures (29 kPa and 9 kPa). Very little difference in skin-electrode impedance can be observed, especially compared to the increased impedance from the smaller electrode size (2 mm x 2 mm) and the lower impedance from the presence of the electrolyte gel.

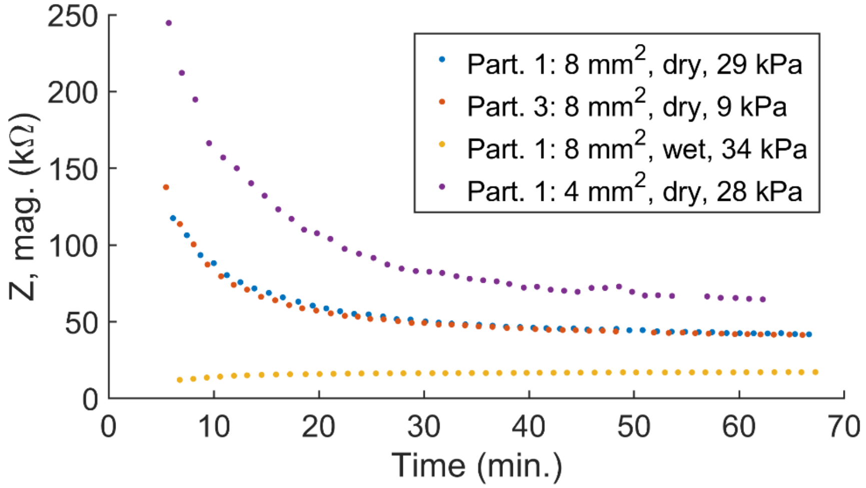

Fig. 5-7. Comparison of skin-electrode impedance over time for different pressures, electrode sizes, and electrolyte presence. The skin-electrode impedance for the 8 mm^2 dry electrodes is very similar between participant 1 and participant 3, despite the drastically different pressures (28.8 kPa and 8.9 kPa). The presence of an electrolyte or using a different electrode area (4 mm^2) has a much larger effect on skin-electrode impedance.

5.4.2 Compensation

The measured impedance, Z_{meas}, includes contributions from the measurement system that must be removed with compensation according to (1). Fig. 5-8 shows the measured impedance (yellow) and the compensated impedance (purple) of a single participant for three different sizes of electrodes: 4 mm^2 (solid), 8 mm^2 (dashed), and 32 mm^2 (dash-dotted). The system open impedance (dash-dotted orange) and short impedance (dashed blue) are also shown. As described previously, Z_{open} is found by fitting a capacitor to the measured impedance above 500 kHz and Z_{short} is the parallel addition of Z_{open} and the 20 kΩ safety resistor. The compensated impedance above about 100 kHz makes little physical sense, due to the rapidly converging values of Z_{short} and Z_{open} and the nature of the poles and zeros in (1). For this reason, the remaining analysis will be done using compensated data up to 100 kHz. The actual high frequency limit of reliability depends on the size of the electrode array. The larger area electrodes have a lower impedance magnitude, which will run into the lower limit (Z_{short}) imposed by the safety resistor at a lower frequency. The compensation is able to partially remove the effect of the safety resistor (compare the yellow lines to the purple lines in Fig. 5-8). A more definite upper limit occurs when $Z_{open} - Z_{short}$ or $Z_{open} - Z_{meas}$ approaches zero, as can be seen in (1). We will still use 100 kHz as the cutoff and highlight, where necessary, when results might have run into this upper frequency limit of reliability.

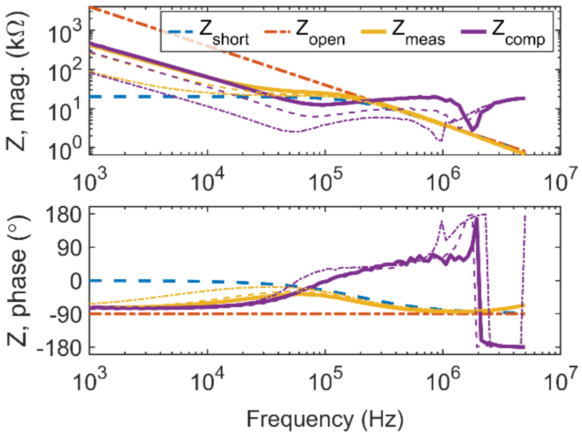

Fig. 5-8. The magnitude and phase of the as-measured and compensated impedance. The system open and short circuit impedances are also shown.

5.4.3 Acclimation Time

Acclimation time was estimated according to Eq. (5.5) for each participant and electrode array size from 1 kHz to 100 kHz. Fig. 5-9 shows the time-dependence of the compensated impedance at 10 kHz for the 2 mm x 16 mm electrode array on participant 2. In this particular case, the acclimation time is about 45 minutes and the impedance magnitude at acclimation is approximately 12 kΩ. In most cases (as pictured here), the impedance continues to change after the acclimation time but at a rate 100 times less than when the electrodes were first placed on the wrist.

The results of one electrode area for two different participants (32 mm^2 for participant 1 and 4 mm^2 for participant 3) have been excluded due to a poor fit to Eq. (5.2), as determined by an R^2 below 0.8. The poor fit occurred due to movement or other artifacts that were plainly visible in the skin-electrode impedance.

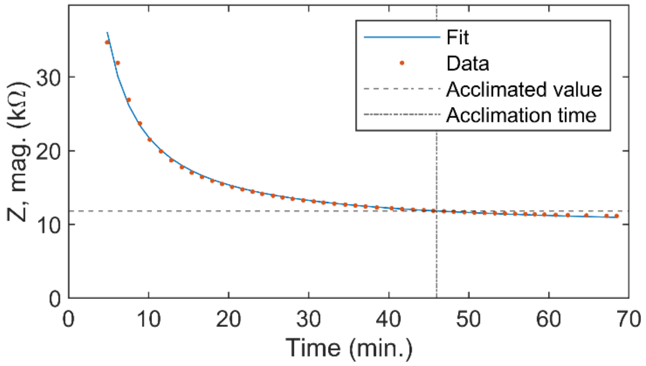

Fig. 5-9. The acclimation profile of the skin-electrode impedance at 10 kHz for the 2 mm x 16 mm electrode array on participant 2.

Table 5-3 lists the acclimation time (in minutes) for each participant and electrode area. The mean acclimation time for each subject is listed in the rightmost column, while the mean acclimation time for each area is listed in the bottom row. The half-range of the averaged data is used as the uncertainty due to the limited number of averaged data points. The average (mean) across all participants and electrode areas is 26 ± 2 minutes, where the standard error was used instead.

Table 5-3
Acclimation time (in minutes)

	CNT Area			
Subject	4 mm^2	8 mm^2	32 mm^2	Mean
1	44	41	----	42±2
2	22	32	49	34±13
3	----	28	27	27±0.5
4	25	22	30	26±4
5	25	29	41	31±8
Mean	29±11	30±10	37±11	32±3

The only fit parameter needed to estimate acclimation time is b (see Eq. (5.5)). The b parameter did not appear to depend on frequency, indicating a constant acclimation time over frequency as seen in Fig. 5-10. The average b from 1 kHz to 10 kHz was -1.8 ± 0.7, -1.8 ± 0.5, and -1.5 ± 0.2, for the electrode areas of 4 mm^2, 8 mm^2, and 32 mm^2, respectively. Fig. 5-10 also shows that the acclimation time as a function of frequency is relatively flat. Additionally, there does not appear to be any dependence on electrode area, according to Fig. 5-10, Table 5-3, and the average values of b.

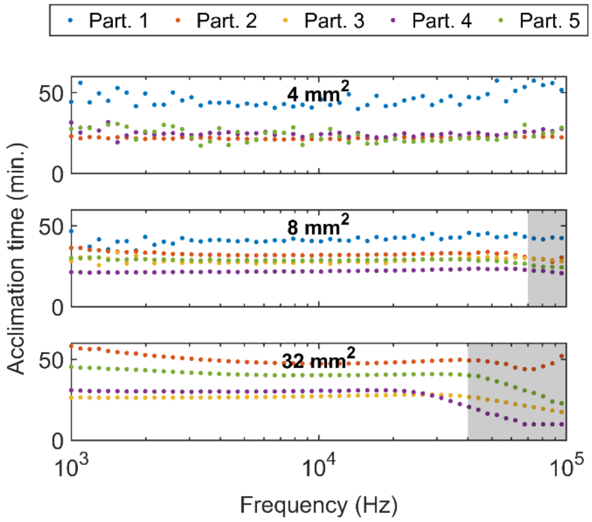

Fig. 5-10. Acclimation time for each participant and electrode size. The acclimation time does not appear to depend on frequency.

5.4.4 *Acclimated Impedance*

The skin-electrode impedance after acclimation depends on frequency and the electrode area. Fig. 5-11 shows the acclimated skin-electrode impedance magnitude averaged over all participants for each electrode size. The skin-electrode impedance decreases with area and also decreases with frequency (see also Fig. 5-8). The frequency dependence (at lower frequencies) is similar to what would be expected from a purely capacitive element. However, Fig. 5-8 shows that the impedance magnitude slope is not quite that of a capacitor and that the phase is not -90°. A better model is a constant phase element [18, p. 344]. The upper frequency limit of reliability (caused by the measurement system's short circuit impedance Z_{short}) occurs at about 70 kHz for the 8 mm^2 electrodes and 30 to 50 kHz for the 32 mm^2 electrodes, as can be seen with the upturns in the impedance data in Fig. 5-11.

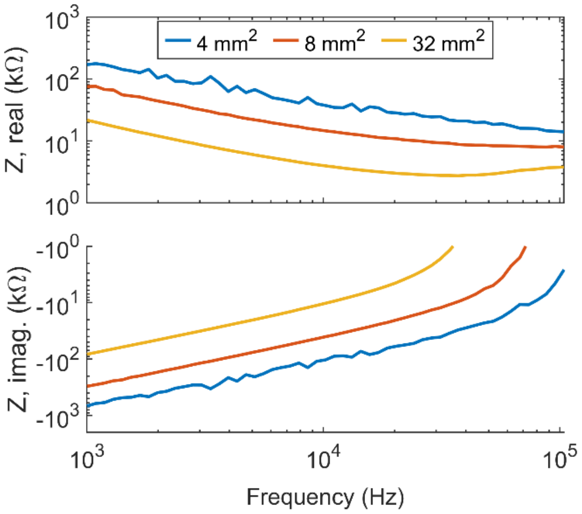

Fig. 5-11. The acclimated skin-electrode impedance magnitude for each electrode size, averaged over all participants. Skin-electrode impedance decreases with frequency and electrode area. The frequency dependence is also seen in Fig. 5-8.

5.4.5 Wet vs. Dry Electrodes

There is a significant difference in skin-electrode impedance between electrodes that have a wet electrolyte and those that do not (see Fig. 5-7). The skin-electrode impedance for wet electrodes tends to slightly increase during the acclimation period, while the skin-electrode impedance for dry electrodes significantly decreases during the same time. The acclimated skin-electrode impedance for dry electrodes never quite falls to the level of the wet electrode impedance. However, electrodes with larger areas have more similar wet and dry skin-electrode impedances. Fig. 5-12 shows the compensated impedance over the duration of the acclimation study for wet and dry electrodes. The difference between dry and wet electrodes for the 32 mm^2 electrodes is much less than for the 4 mm^2 electrodes, indicating that the dry version of the larger electrode behaves similarly to its wet counterpart. The relative difference between the dry and wet impedance magnitudes ($Z_{rel} = (|Z|_{dry} - |Z|_{wet})/|Z|_{wet}$) also decreases as electrode area increases. At 10 kHz, Z_{rel} is 55% for the 4 mm^2, 20% for the 4 mm^2, and 10% for the 32 mm^2 electrodes.

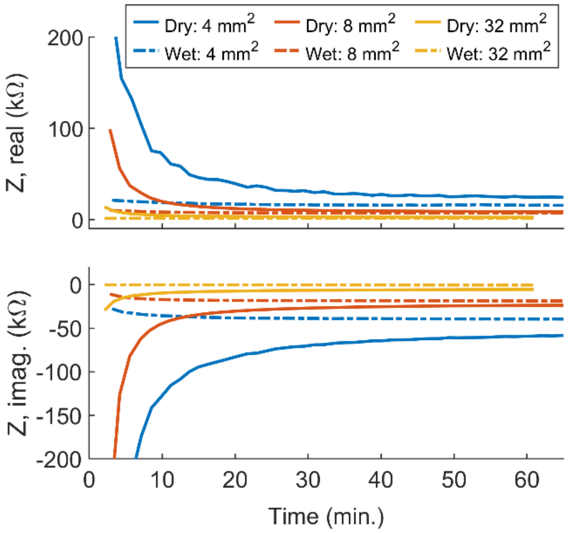

Fig. 5-12. The compensated impedance at 10 kHz over the acclimation study for wet and dry electrodes. As the skin-electrode interface acclimates, the difference between wet and dry electrodes decreases.

5.4.6 Placement Variation

A small variation study was performed after the acclimation study. In the first part of the variation study, the active electrodes were electronically shifted by one electrode (about 2.5 mm) to the right, to the left, and then back to the middle (see Fig. 5-6). Full impedance spectra for the wet and dry electrodes were recorded, though we only performed this analysis at 10 kHz. For dry electrodes, we found that the left electrode configuration had a higher skin-electrode impedance magnitude than the middle configuration by an average of 9% (across all participants and electrode areas). The right set of electrodes was higher by an average of 1% (see Fig. 5-13 for a breakdown by electrode area). In both cases, the difference is less than the difference from one electrode size to another. For example, the skin-electrode impedance drops by 30% from 4 mm^2 to 8 mm^2, and by another 45% from 8 mm^2 to 32 mm^2. For wet electrodes, the difference was even smaller. In other words, the electrodes that had not previously carried current (but were on the wrist for the entire acclimation study) had essentially the same skin-electrode impedance as the current carrying (or middle) electrodes.

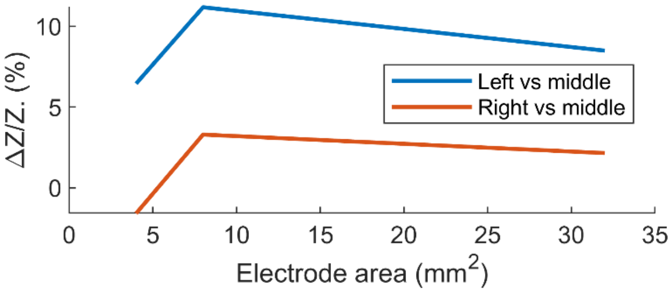

Fig. 5-13. Relative difference in skin-electrode impedance after acclimation of nearby electrodes.

The second part of the variation study involved removing the electrode array and replacing it after 5 minutes. Full impedance spectra were then recorded for both wet and dry electrodes. This process was repeated once more. We found that the skin-electrode impedance increased after both 5 minute intervals and that the increase appeared to depend on the size of the electrodes (see Fig. 5-14). The skin-electrode impedance increased by an average of 74%, 60%, and 70% after the first interval for the 4 mm^2, 8 mm^2, and 32 mm^2 dry electrodes, respectively. It changed by 50%, 36%, and -10% after the second interval for the same respective electrodes. For the wet electrodes, the skin-electrode impedance increased by an average of 15%, 11%, and 5% after the first interval for the 4 mm^2, 8 mm^2, and 32 mm^2 electrodes, respectively. It increased by 48%, 16%, and 2% after the second interval for the same respective electrodes.

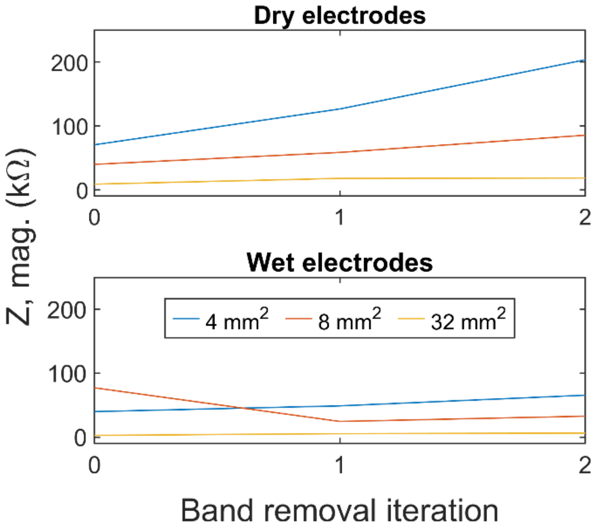

Fig. 5-14. Skin-electrode impedance magnitude for dry and wet electrodes averaged over all participants.

5.5 Discussion

We measured the skin-electrode impedance of small carbon composite electrodes with and without a wet electrolyte. We showed that the skin-electrode impedance of dry electrodes changes rapidly during what we termed the acclimation period. The acclimation period is most likely caused by hydration at the skin-electrode interface, since we do not observe the same acclimation with wet electrodes. Fig. 5-7 shows how the skin-electrode impedance for dry electrodes decreases by a factor of 3 to 5 during the first 30 minutes. During the same period, the skin-electrode impedance for wet electrodes actually increases slightly. Wet contact electrodes are infeasible for a long-term wearable application, so understanding skin-electrode impedance acclimation – especially of small electrodes – is vital.

The longer the electrodes are on the skin, the more the skin-electrode impedance of the dry electrodes resembles that of the wet electrodes (see Fig. 5-12). This is especially true for the larger electrode areas. This may mean that dry electrodes are suitable for bioimpedance measurements after a sufficient acclimation period.

In Eq. (5.5), we defined acclimation time in terms of the time derivative of the skin-electrode impedance; however, other definitions are equally valid. For example, an application may require that the skin-electrode impedance drop below a certain threshold before measurement can begin. In such a case, the acclimation time would depend on the skin-electrode impedance and therefore on electrode area and frequency. With our definition, we found that the acclimation time does not appear to depend on electrode area (see Table 5-3) nor on frequency (Fig. 5-10). However, we measured a large variation in acclimation time from participant to participant and even for different electrode areas for the same participant, which makes it difficult to conclusively state whether acclimation time depends on area. Skin-electrode impedance in general does depend on electrode area, and so too does the skin-electrode impedance at acclimation. Fig. 5-11 shows how the acclimated skin-electrode impedance decreases with area and frequency.

Two limitations of our measurement system can be seen in Fig. 5-8. First, the short circuit impedance is very high. We added a series 20 kΩ resistor to limit current to 100 μA in order to comply with the IEC 60601-1 electrical safety standard. However, the current limit in the standard is frequency weighted, meaning the current at higher frequencies can safely be increased (up to a maximum of 10 mA). A properly designed frequency weighted current limiter would decrease Z_{short}, thereby increasing the frequency at which the system could accurately measure impedance. The second limitation was in the excessive trace capacitance on the multiplexer board. By decreasing this parasitic capacitance, it would be possible to increase Z_{open}. This would also increase the frequency at which impedance could be measured.

5.6 Conclusion

This work shows that it is possible to use microfabricated carbon composite electrodes to measure bioimpedance in a wrist-based application. We showed that after acclimation, the skin-electrode impedance of dry electrodes approach that of wet electrodes – especially for larger electrode areas. The acclimation period ranges from 20 minutes to 50 minutes, with a mean of about 30 minutes. During this time, the rate of change of skin-electrode impedance dropped by a factor of 100. The skin-electrode impedance magnitude typically drops by a factor of 3 to 5 during acclimation. This work gives insight into the skin-electrode impedance behavior of small carbon composite electrodes and shows that these electrodes can be used for wrist-based bioimpedance measurements, which is a first step in enabling a bioimpedance wearable device with miniature electrodes.

Chapter 6: Conclusions

Each preceding chapter was written in a self-contained manner with relevant conclusions presented therein. Here I will discuss the principal conclusions of each chapter and tie together any overarching themes.

X-ray detector windows suffer from two competing challenges: they must be strong enough to withstand 1 atm of differential pressure and thin enough to transmit sufficient low-energy x-rays. Through numerical analysis, I showed that this competition can be partially alleviated by the addition of a hierarchical support. This is a support that bridges the gap between the thick primary support and the very thin pressure membrane. It allows for greater open area and thinner pressure membranes. The software I developed for this analysis is available for others to use in their own analyses[21]. Next steps in this research may involve modeling different support geometries and materials, or fabricating an x-ray window with a hierarchical support structure.

Another way to improve x-ray detector window transmission is to use stronger and thinner pressure membranes. We had previously attempted to use many-layer graphene (MLG) as a pressure barrier[4]. In order to better understand the materials properties of MLG, we performed bulge testing. Ideally, bulge testing would yield the Young's modulus and strength; however, bulge testing analysis cannot cope with wrinkled film. This dissertation reported on a new method of measuring the properties of suspended films called multi-point force-deflection (MFD). Using this method, it is possible to measure the local properties of heterogeneous films by analyzing the force-deflection of microcantilevers in the film. I developed software for analyzing the atomic force microscope force-volume results, which can be found in Appendix C. Future work in this topic might focus on using MFD with different materials or expanded finite element modeling to show when MFD is applicable and when it is not.

Bioimpedance can be used to measure the cardiac pulse. In order to understand how electrode position can affect the sensitivity of the pulsatile measurement, I used finite element modeling to analyze several electrode positions. I made predictions that were tested in a human subjects study. (Unfortunately, that trial was inconclusive.) The finite element modeling results indicated that the highest sensitivity occurred when the electrodes were centered on the artery, but this depended on the underlying tissue. Next steps in this research might include a repeated human subjects study or using an anatomically improved wrist model.

In a second human subjects study, we examined how the skin-electrode skin-electrode impedance changes with time. We fabricated carbon nanotube electrodes that were infiltrated with carbon, created a solid carbon composite electrode. These electrodes were placed on the skin with two groups: one with a wet electrolyte and one without. We found that acclimation time does not depend on frequency or electrode area, but the value of the acclimated impedance does. After acclimating, the skin-electrode impedance of dry electrodes approached that of wet electrodes. This was especially true for the larger electrode areas. This experiment was performed using a frequency-limited measurement system. In order to understand how these carbon composite electrodes behave a higher frequencies (on the path towards non-invasive glucose detection), this experiment should be repeated using a more capable system.

The final two chapters of this dissertation may seem vastly different from the first two, but they are tied together in both the methods and the multiscale nature of the analysis. The computational modeling of x-ray windows involved length scales from 20 nm to 10 mm, while the analysis of the microcantilever deflection data involved scales ranging from 50 nm to 10 µm. The bioimpedance modeling had length scales from 40 µm to 6 cm. The electrodes used in the acclimation study were approximately 500 μm thick, with an overall length of up to 16 mm. In all cases, I employed multiscale modeling and analysis to solve these disparate problems.

References

[1] M. Ohring, *Material Science of Thin Films*, 2nd ed. Academic Press, 2002.

[2] A. C. Thompson, D. Vaughan, and Center for X-ray optics and advanced light source, *X-ray Data Booklet*. Lawrence Berkeley Laboratory, 2009. [Online]. Available: http://xdb.lbl.gov/

[3] C. Lee, X. Wei, J. W. Kysar, and J. Hone, “Measurement of the Elastic Properties and Intrinsic Strength of Monolayer Graphene,” *Science*, vol. 321, no. 5887, pp. 385–388, Jul. 2008, doi: 10.1126/science.1157996.

[4] J. Rowley, “Sp2 Bonded Carbon for Soft X-Ray Detector Windows,” PhD dissertation, Brigham Young University, Provo, UT, 2021. [Online]. Available: https://scholarsarchive.byu.edu/etd/9365

[5] X. Liang *et al.*, “Toward Clean and Crackless Transfer of Graphene,” *ACS Nano*, vol. 5, no. 11, pp. 9144–9153, Nov. 2011, doi: 10.1021/nn203377t.

[6] Q. Zhou and A. Zettl, “Electrostatic graphene loudspeaker,” *Appl. Phys. Lett.*, vol. 102, no. 22, p. 223109, Jun. 2013, doi: 10.1063/1.4806974.

[7] M. K. Small and W. D. Nix, “Analysis of the accuracy of the bulge test in determining the mechanical properties of thin films,” *J. Mater. Res.*, vol. 7, no. 06, pp. 1553–1563, Jun. 1992, doi: 10.1557/JMR.1992.1553.

[8] T. Tsuchiya and O. Tabata, Eds., *Reliability of MEMS, Ch. 3*. Weinheim: Wiley-VCH, 2008.

[9] R. Rasuli, A. I. zad, and M. M. Ahadian, “Mechanical properties of graphene cantilever from atomic force microscopy and density functional theory,” *Nanotechnology*, vol. 21, no. 18, p. 185503, 2010, doi: 10.1088/0957-4484/21/18/185503.

[10] Z. H. Lewis, L. Pritting, A.-L. Picazo, and M. JeanMarie-Tucker, “The utility of wearable fitness trackers and implications for increased engagement: An exploratory, mixed methods observational study,” *Digit. Health*, vol. 6, p. 2055207619900059, Jan. 2020, doi: 10.1177/2055207619900059.

[11] S. R. Abbas, F. Zhu, and N. W. Levin, “Bioimpedance can solve problems of fluid overload,” *J. Ren. Nutr. Off. J. Counc. Ren. Nutr. Natl. Kidney Found.*, vol. 25, no. 2, pp. 234–237, Mar. 2015, doi: 10.1053/j.jrn.2014.10.014.

[12] Guofeng Qiao, Wei Wang, Wei Duan, Fan Zheng, A. J. Sinclair, and C. R. Chatwin, “Bioimpedance analysis for the characterization of breast cancer cells in suspension,” *IEEE Trans. Biomed. Eng.*, vol. 59, no. 8, pp. 2321–2329, Aug. 2012, doi: 10.1109/TBME.2012.2202904.

[13] N. Andreasen *et al.*, “Skin Electrical Resistance as a Diagnostic and Therapeutic Biomarker of Breast Cancer Measuring Lymphatic Regions,” *IEEE Access*, vol. 9, pp. 152322–152332, 2021, doi: 10.1109/ACCESS.2021.3123569.

[14] R. C. Yung, M. Y. Zeng, G. J. Stoddard, M. Garff, and K. Callahan, “Transcutaneous Computed Bioconductance Measurement in Lung Cancer: A Treatment Enabling Technology Useful for Adjunctive Risk Stratification in the Evaluation of Suspicious Pulmonary Lesions,” *J. Thorac. Oncol.*, vol. 7, no. 4, pp. 681–689, Apr. 2012, doi: 10.1097/JTO.0b013e31824a8dcd.

[15] J. Ferreira, F. Seoane, and K. Lindecrantz, “Portable bioimpedance monitor evaluation for continuous impedance measurements. Towards wearable plethysmography applications,” in *2013 35th Annual International Conference of the IEEE Engineering in Medicine and Biology Society (EMBC)*, Jul. 2013, pp. 559–562. doi: 10.1109/EMBC.2013.6609561.

[16] A. Caduff and Y. Feldman, “Method and a device for measuring glucose,” US7184810B2, Feb. 27, 2007 Accessed: Feb. 11, 2019. [Online]. Available: https://patents.google.com/patent/US7184810B2/en

[17] A. Caduff *et al.*, “Multisensor Concept for non-invasive Physiological Monitoring,” in *2007 IEEE Instrumentation Measurement Technology Conference IMTC 2007*, May 2007, pp. 1–4. doi: 10.1109/IMTC.2007.379070.

[18] A. Caduff *et al.*, “Non-invasive glucose monitoring in patients with Type 1 diabetes: A Multisensor system combining sensors for dielectric and optical characterisation of skin,” *Biosens. Bioelectron.*, vol. 24, no. 9, pp. 2778–2784, May 2009, doi: 10.1016/j.bios.2009.02.001.

[19] A. Caduff, P. Ben Ishai, and Y. Feldman, “Continuous noninvasive glucose monitoring; water as a relevant marker of glucose uptake in vivo,” *Biophys. Rev.*, vol. 11, no. 6, pp. 1017–1035, Dec. 2019, doi: 10.1007/s12551-019-00601-7.

[20] Diego A. Leon, “Acclimation of Skin-electrode impedance and Wrist-Based Pulsatile Signal Measurements Through Electrical Bioimpedance,” M.S. Thesis, Brigham Young University, Provo, UT, 2021.

[21] K. G. Larsen, “xray_window: strength and transmission.” Jun. 2022. Accessed: Jun. 17, 2022. [Online]. Available: https://github.com/larsenkg/xray_window

[22] B. L. Henke, E. M. Gullikson, and J. C. Davis, “X-Ray Interactions: Photoabsorption, Scattering, Transmission, and Reflection at E = 50-30,000 eV, Z = 1-92,” *At. Data Nucl. Data Tables*, vol. 54, no. 2, pp. 181–342, Jul. 1993, doi: 10.1006/adnd.1993.1013.

[23] J. H. Hubbell, Wm. J. Veigele, E. A. Briggs, R. T. Brown, D. T. Cromer, and R. J. Howerton, “Atomic form factors, incoherent scattering functions, and photon scattering cross sections,” *J. Phys. Chem. Ref. Data*, vol. 4, no. 3, pp. 471–538, Jul. 1975, doi: 10.1063/1.555523.

[24] P. T. Torma *et al.*, “Ultra-Thin Silicon Nitride X-Ray Windows,” *IEEE Trans. Nucl. Sci.*, vol. 60, no. 2, pp. 1311–1314, Apr. 2013, doi: 10.1109/TNS.2013.2243754.

[25] P.-H. Chen, C.-H. Yang, C.-Y. Tsai, T.-L. Chang, W.-C. Hsu, and T.-C. Chen, “Young’s Modulus of High Aspect Ratio Si 3 N 4 Nano-thickness Membrane,” in *Nanotechnology, 2007. IEEE-NANO 2007. 7th IEEE Conference on*, 2007, pp. 1341–1344. Accessed: Feb. 27, 2017. [Online]. Available: http://ieeexplore.ieee.org/abstract/document/4601367/

[26] I. Yanagi, T. Ishida, K. Fujisaki, and K. Takeda, “Fabrication of 3-nm-thick Si3N4 membranes for solid-state nanopores using the poly-Si sacrificial layer process,” *Sci. Rep.*, vol. 5, p. 14656, Oct. 2015, doi: 10.1038/srep14656.

[27] V. P. Adiga, B. Ilic, R. A. Barton, I. Wilson-Rae, H. G. Craighead, and J. M. Parpia, “Approaching intrinsic performance in ultra-thin silicon nitride drum resonators,” *J. Appl. Phys.*, vol. 112, no. 6, p. 064323, 2012, doi: 10.1063/1.4754576.

[28] R. Perkins, D. Allred, L. Knight, and J. Thorne, “Design of High Performance Soft X-Ray Windows,” *Adv. X-Ray Anal.*, vol. 33, pp. 615–622, 1989.

[29] R. C. Davis, R. Vanfleet, K. Zufeldt, A. L. Davis, and S. D. Liddiard, “High strength carbon fiber composite wafers for microfabrication,” US9174412B2, Nov. 03, 2015 Accessed: May 26, 2022. [Online]. Available: https://patents.google.com/patent/US9174412B2/en

[30] S. Huebner, N. Miyakawa, A. Pahlke, and F. Kreupl, “Design and properties of low-energy X-ray transmission windows based on graphenic carbon: Low-energy X-ray transmission windows based on graphenic carbon,” *Phys. Status Solidi B*, vol. 252, no. 11, pp. 2564–2573, Nov. 2015, doi: 10.1002/pssb.201552216.

[31] Moxtek, “Ultra-thin AP3 X-ray Windows.” Accessed: Apr. 14, 2022. [Online]. Available: https://moxtek.com/wp-content/uploads/pdfs/WIN-DATA-1001-AP3-Ultra-thin-Windows-Rev-G.pdf

[32] Amptek, “Patented C-Series Low Energy X-Ray Windows – Amptek – X-Ray Detectors and Electronics.” https://www.amptek.com/products/x-ray-detectors/fastsdd-x-ray-detectors-for-xrf-eds/c-series-low-energy-x-ray-windows (accessed Jun. 17, 2022).

[33] P. T. Torma *et al.*, “Performance and Properties of Ultra-Thin Silicon Nitride X-ray Windows,” *IEEE Trans. Nucl. Sci.*, vol. 61, no. 1, pp. 695–699, Feb. 2014, doi: 10.1109/TNS.2014.2298434.

[34] A. S. da Silva Sobrinho, M. Latrèche, G. Czeremuszkin, J. E. Klemberg-Sapieha, and M. R. Wertheimer, “Transparent barrier coatings on polyethylene terephthalate by single- and dual-frequency plasma-enhanced chemical vapor deposition,” *J. Vac. Sci. Technol. A*, vol. 16, no. 6, pp. 3190–3198, Nov. 1998, doi: 10.1116/1.581519.

[35] J. J. Vlassak, “New experimental techniques and analysis methods for the study of the mechanical properties of materials in small volumes,” Stanford University, 1994.

[36] L. L. Howell, *Compliant Mechanisms*. John Wiley & Sons, 2001.

[37] D. F. Swinehart, “The beer-lambert law,” *J Chem Educ*, vol. 39, no. 7, p. 333, 1962.

[38] R. Storn and K. Price, “Differential Evolution – A Simple and Efficient Heuristic for global Optimization over Continuous Spaces,” *J. Glob. Optim.*, vol. 11, no. 4, pp. 341–359, Dec. 1997, doi: 10.1023/A:1008202821328.

[39] P. Virtanen *et al.*, “SciPy 1.0: fundamental algorithms for scientific computing in Python,” *Nat. Methods*, vol. 17, no. 3, Art. no. 3, Mar. 2020, doi: 10.1038/s41592-019-0686-2.

[40] R. T. Creighton, S. Liddiard, and S. Cornaby, “Measurements of the X-ray Transmission Characteristics of Moxtek’s AP3 X-Ray Windows,” *Microsc. Microanal.*, vol. 19, no. S2, pp. 1350–1351, Aug. 2013, doi: 10.1017/S143192761300874X.

[41] J. J. Vlassak and W. D. Nix, “A new bulge test technique for the determination of Young’s modulus and Poisson’s ratio of thin films,” *J. Mater. Res.*, vol. 7, no. 12, pp. 3242–3249, 1992.

[42] T. P. Weihs, S. Hong, J. C. Bravman, and W. D. Nix, “Mechanical deflection of cantilever microbeams: A new technique for testing the mechanical properties of thin films,” *J. Mater. Res.*, vol. 3, no. 5, pp. 931–942, Oct. 1988, doi: 10.1557/JMR.1988.0931.

[43] P. Li, Z. You, and T. Cui, “Graphene cantilever beams for nano switches,” *Appl. Phys. Lett.*, vol. 101, no. 9, p. 093111, Aug. 2012, doi: 10.1063/1.4738891.

[44] M. Poot and H. S. J. van der Zant, “Nanomechanical properties of few-layer graphene membranes,” *Appl. Phys. Lett.*, vol. 92, no. 6, p. 063111, Feb. 2008, doi: 10.1063/1.2857472.

[45] G.-H. Lee *et al.*, “High-Strength Chemical-Vapor–Deposited Graphene and Grain Boundaries,” *Science*, vol. 340, no. 6136, pp. 1073–1076, May 2013, doi: 10.1126/science.1235126.

[46] K. K. Al-Quraishi, Q. He, W. Kauppila, M. Wang, and Y. Yang, “Mechanical testing of two-dimensional materials: a brief review,” *Int. J. Smart Nano Mater.*, vol. 11, no. 3, pp. 207–246, Jul. 2020, doi: 10.1080/19475411.2020.1791276.

[47] G. Guhados, W. Wan, and J. L. Hutter, “Measurement of the Elastic Modulus of Single Bacterial Cellulose Fibers Using Atomic Force Microscopy,” *Langmuir*, vol. 21, no. 14, pp. 6642–6646, Jul. 2005, doi: 10.1021/la0504311.

[48] G. Guhados, W. Wan, X. Sun, and J. L. Hutter, "Simultaneous measurement of Young's and shear moduli of multiwalled carbon nanotubes using atomic force microscopy," *J. Appl. Phys.*, vol. 101, no. 3, p. 033514, Feb. 2007, doi: 10.1063/1.2433125.

[49] O. L. Blakslee, D. G. Proctor, E. J. Seldin, G. B. Spence, and T. Weng, "Elastic Constants of Compression-Annealed Pyrolytic Graphite," *J. Appl. Phys.*, vol. 41, no. 8, pp. 3373–3382, Jul. 1970, doi: 10.1063/1.1659428.

[50] H. I. Rasool, C. Ophus, W. S. Klug, A. Zettl, and J. K. Gimzewski, "Measurement of the intrinsic strength of crystalline and polycrystalline graphene," *Nat. Commun.*, vol. 4, no. 1, Art. no. 1, Nov. 2013, doi: 10.1038/ncomms3811.

[51] S. Huebner, N. Miyakawa, S. Kapser, A. Pahlke, and F. Kreupl, "High Performance X-Ray Transmission Windows Based on Graphenic Carbon," *IEEE Trans. Nucl. Sci.*, vol. 62, no. 2, pp. 588–593, Apr. 2015, doi: 10.1109/TNS.2015.2396116.

[52] S. Huebner, N. Miyakawa, A. Pahlke, and F. Kreupl, "Performance Improvement of Graphenic Carbon X-ray Transmission Windows," *MRS Adv.*, vol. 1, no. 20, pp. 1441–1446, 2016, doi: 10.1557/adv.2016.194.

[53] H. Min and A. H. MacDonald, "Origin of Universal Optical Conductivity and Optical Stacking Sequence Identification in Multilayer Graphene," *Phys. Rev. Lett.*, vol. 103, no. 6, p. 067402, Aug. 2009, doi: 10.1103/PhysRevLett.103.067402.

[54] S.-E. Zhu, S. Yuan, and G. C. A. M. Janssen, "Optical transmittance of multilayer graphene," *EPL Europhys. Lett.*, vol. 108, no. 1, p. 17007, 2014, doi: 10.1209/0295-5075/108/17007.

[55] J. E. Sader *et al.*, "Spring constant calibration of atomic force microscope cantilevers of arbitrary shape," *Rev. Sci. Instrum.*, vol. 83, no. 10, p. 103705, Oct. 2012, doi: 10.1063/1.4757398.

[56] A. C. Ferrari and D. M. Basko, "Raman spectroscopy as a versatile tool for studying the properties of graphene," *Nat. Nanotechnol.*, vol. 8, no. 4, pp. 235–246, Apr. 2013, doi: 10.1038/nnano.2013.46.

[57] D. G. Papageorgiou, I. A. Kinloch, and R. J. Young, "Mechanical properties of graphene and graphene-based nanocomposites," *Prog. Mater. Sci.*, vol. 90, pp. 75–127, Oct. 2017, doi: 10.1016/j.pmatsci.2017.07.004.

[58] F. Traversi *et al.*, "Elastic properties of graphene suspended on a polymer substrate by e-beam exposure," *New J. Phys.*, vol. 12, no. 2, p. 023034, Feb. 2010, doi: 10.1088/1367-2630/12/2/023034.

[59] E. Sandoz-Rosado, E. D. Wetzel, J. T. Smith, S. Oida, and J. Bai, "The mechanical characterization of stacked, multilayer graphene cantilevers and plates," in *2015 IEEE 15th International Conference on Nanotechnology (IEEE-NANO)*, Jul. 2015, pp. 37–40. doi: 10.1109/NANO.2015.7388631.

[60] A. Henriksen *et al.*, "Using Fitness Trackers and Smartwatches to Measure Physical Activity in Research: Analysis of Consumer Wrist-Worn Wearables," *J. Med. Internet Res.*, vol. 20, no. 3, p. e9157, Mar. 2018, doi: 10.2196/jmir.9157.

[61] T. H. Huynh, R. Jafari, and W. Chung, "Noninvasive Cuffless Blood Pressure Estimation Using Pulse Transit Time and Impedance Plethysmography," *IEEE Trans. Biomed. Eng.*, vol. 66, no. 4, pp. 967–976, Apr. 2019, doi: 10.1109/TBME.2018.2865751.

[62] J. Schneider, M. Schroth, M. Holzhey, T. Blöcher, and W. Stork, "An approach to improve impedance plethysmography on the wrist by using adaptive feedback control," in *2017 IEEE*

Sensors Applications Symposium (SAS), Mar. 2017, pp. 1–6. doi: 10.1109/SAS.2017.7894063.

[63] K. Pesti, M. Metshein, P. Annus, H. Kõiv, and M. Min, "Electrode Placement Strategies for the Measurement of Radial Artery Bioimpedance: Simulations and Experiments," *IEEE Trans. Instrum. Meas.*, vol. 70, pp. 1–10, 2021, doi: 10.1109/TIM.2020.3011784.

[64] S. Grimnes and Martinsen Ørjan G., *Bioimpedance and Bioelectricity Basics*, 3rd ed. Elsevier, 2015. doi: 10.1016/C2012-0-06951-7.

[65] D. Andreuccetti, R. Fossi, and C. Petrucci, "An Internet resource for the calculation of the dielectric properties of body tissues in the frequency range 10 Hz - 100 GHz," *Dielectric Properties of Body Tissues: Home page*, 1997. http://niremf.ifac.cnr.it/tissprop/ (accessed Jun. 30, 2022).

[66] A. Kamišalić, I. Fister, M. Turkanović, and S. Karakatič, "Sensors and Functionalities of Non-Invasive Wrist-Wearable Devices: A Review," *Sensors*, vol. 18, no. 6, p. 1714, Jun. 2018, doi: 10.3390/s18061714.

[67] T. H. Huynh, R. Jafari, and W. Y. Chung, "An Accurate Bioimpedance Measurement System for Blood Pressure Monitoring," *Sensors*, vol. 18, no. 7, Jul. 2018, doi: 10.3390/s18072095.

[68] T. Dai and A. Adler, "In Vivo Blood Characterization From Bioimpedance Spectroscopy of Blood Pooling," *IEEE Trans. Instrum. Meas.*, vol. 58, no. 11, pp. 3831–3838, Nov. 2009, doi: 10.1109/TIM.2009.2020836.

[69] X. Huang, W.-H. Yeo, Y. Liu, and J. A. Rogers, "Epidermal Differential Impedance Sensor for Conformal Skin Hydration Monitoring," *Biointerphases*, vol. 7, no. 1, p. 52, Aug. 2012, doi: 10.1007/s13758-012-0052-8.

[70] R. Kusche, S. Kaufmann, and M. Ryschka, "Dry electrodes for bioimpedance measurements—design, characterization and comparison," *Biomed. Phys. Ampmathsemicolon Eng. Express*, vol. 5, no. 1, p. 015001, Nov. 2018, doi: 10.1088/2057-1976/aaea59.

[71] Y. M. Chi, T.-P. Jung, and G. Cauwenberghs, "Dry-Contact and Noncontact Biopotential Electrodes: Methodological Review," *IEEE Rev. Biomed. Eng.*, vol. 3, pp. 106–119, 2010, doi: 10.1109/RBME.2010.2084078.

[72] W. Sae-lim, P. Phukpattaranont, and K. Thongpull, "Effect of Electrode Skin Impedance on Electromyography Signal Quality," in *2018 15th International Conference on Electrical Engineering/Electronics, Computer, Telecommunications and Information Technology (ECTI-CON)*, Jul. 2018, pp. 748–751. doi: 10.1109/ECTICon.2018.8619967.

[73] B. Taji, A. D. C. Chan, and S. Shirmohammadi, "Effect of Pressure on Skin-Electrode Impedance in Wearable Biomedical Measurement Devices," *IEEE Trans. Instrum. Meas.*, vol. 67, no. 8, pp. 1900–1912, Aug. 2018, doi: 10.1109/TIM.2018.2806950.

[74] D. P. Burbank and J. G. Webster, "Reducing skin potential motion artefact by skin abrasion," *Med. Biol. Eng. Comput.*, vol. 16, no. 1, pp. 31–38, Jan. 1978, doi: 10.1007/BF02442929.

[75] P. Cattarello and R. Merletti, "Characterization of dry and wet Electrode-Skin interfaces on different skin treatments for HDsEMG," in *2016 IEEE International Symposium on Medical Measurements and Applications (MeMeA)*, May 2016, pp. 1–6. doi: 10.1109/MeMeA.2016.7533808.

[76] T. A. Naylor, "Exploration of Constant-Force Wristbands for a Wearable Health Device," M.Sc., Brigham Young University, United States -- Utah, 2021. Accessed: Jun. 22, 2022.

[Online]. Available: https://www.proquest.com/docview/2606850130/abstract/FC0522EBF62A41A1PQ/1

[77] M. M. Puurtinen, S. M. Komulainen, P. K. Kauppinen, J. A. V. Malmivuo, and J. A. K. Hyttinen, “Measurement of noise and impedance of dry and wet textile electrodes, and textile electrodes with hydrogel,” in *2006 International Conference of the IEEE Engineering in Medicine and Biology Society*, Aug. 2006, pp. 6012–6015. doi: 10.1109/IEMBS.2006.260155.

[78] A. Searle and L. Kirkup, “A direct comparison of wet, dry and insulating bioelectric recording electrodes,” *Physiol. Meas.*, vol. 21, no. 2, pp. 271–283, May 2000, doi: 10.1088/0967-3334/21/2/307.

[79] D. N. Hutchison *et al.*, “High aspect ratio microelectromechanical systems: A versatile approach using carbon nanotubes as a framework,” in *TRANSDUCERS 2009 - 2009 International Solid-State Sensors, Actuators and Microsystems Conference*, Jun. 2009, pp. 1604–1607. doi: 10.1109/SENSOR.2009.5285766.

[80] D. N. Hutchison *et al.*, “Carbon Nanotubes as a Framework for High-Aspect-Ratio MEMS Fabrication,” *J. Microelectromechanical Syst.*, vol. 19, no. 1, pp. 75–82, Feb. 2010, doi: 10.1109/JMEMS.2009.2035639.

[81] N. Yang, G. M. Swain, and X. Jiang, “Nanocarbon Electrochemistry and Electroanalysis: Current Status and Future Perspectives,” *Electroanalysis*, vol. 28, no. 1, pp. 27–34, 2016, doi: 10.1002/elan.201500577.

[82] R. L. McCreery, “Advanced Carbon Electrode Materials for Molecular Electrochemistry,” *Chem. Rev.*, vol. 108, no. 7, pp. 2646–2687, Jul. 2008, doi: 10.1021/cr068076m.

[83] MicroChem NANO PMMA and Copolymer Datasheet, “NANO PMMA and Copolymer Datasheet.” 2001. Accessed: Jun. 23, 2021. [Online]. Available: https://kayakuam.com/wp-content/uploads/2019/09/PMMA_Data_Sheet.pdf

[84] J. W. Suk *et al.*, “Transfer of CVD-Grown Monolayer Graphene onto Arbitrary Substrates,” *ACS Nano*, vol. 5, no. 9, pp. 6916–6924, Sep. 2011, doi: 10.1021/nn201207c.

Appendix A: Chapter 3 Supplemental Information

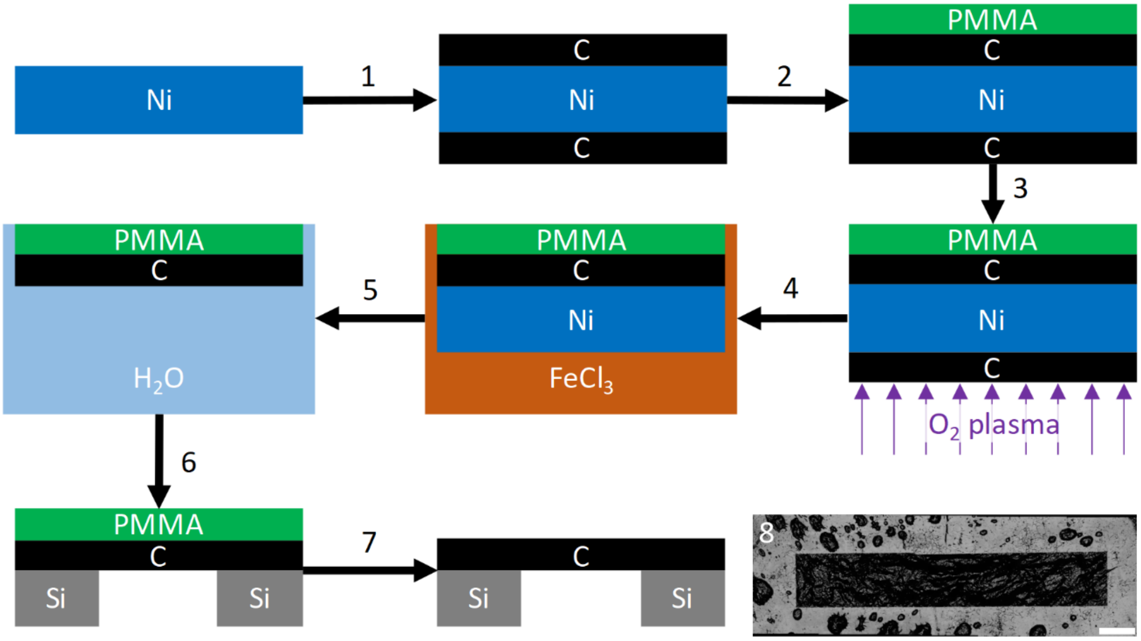

Fig. A-1. Process diagram for many-layer graphene growth and transfer. (1) Chemical vapor deposition on nickel foil. (2) PMMA spin cast on nickel/graphene stack for transfer assistance. (3) Oxygen plasma etch to remove unwanted backside carbon. (4) Ferric chloride etch to remove nickel foil. (5) Water bath for cleaning graphene/PMMA stack. (6) Graphene/PMMA stack placed on silicon support chip. (7) PMMA volatized and removed in furnace with hydrogen/argon atmosphere. (8) Top-down optical reflectance micrograph of suspended many-layer graphene on silicon support. The scale bar is 500 µm long.

Many-layer graphene fabrication

The MLG films were fabricated using a low-pressure chemical vapor deposition (LPCVD) process on a nickel substrate[4], [6]. Nickel foils with lateral dimensions of about 1 cm x 1 cm and thicknesses of 100 µm were polished on a lapping wheel with 3 µm diamond grit lapping films until highly reflective. Several foils were placed on a 1 inch by 3 inch quartz slide and the slide was inserted into a 1 inch quartz tube furnace. Argon and hydrogen were used as process gases and methane served as the carbon source. The nickel was first annealed for 15 minutes at 1050 °C with an argon flow rate of 10 sccm and a hydrogen flow rate of 50 sccm. Methane was then introduced with a flow rate of 50 sccm for 13 minutes followed by an increase to 200 sccm for 2 minutes. The furnace was then turned off, opened, and the quartz tube was rapidly cooled with a spray of compressed air for 6 minutes or until reaching about 100 °C.

The nickel foil was removed and the MLG film was prepared for transfer to a silicon substrate. The top surface of the nickel and MLG stack was spin-coated with 6% poly(methyl methacrylate) (PMMA) in anisole (MicroChem 950 PMMA A6) at 2000 rpm. This gives an estimated PMMA thickness of 600 nm according to the spin speed curves in the PMMA datasheet[83]. The sample with PMMA was then baked on a hotplate at 220 °C for 90 seconds in order to drive off the solvent. A 10 minute backside oxygen plasma etch at 250 W was used to remove the unwanted backside carbon that would otherwise inhibit the etching of the nickel. If backside carbon was still visible, additional etches were performed. An aqueous $FeCl_3$ solution was prepared by placing 0.1 g of $FeCl_3$ per mL of deionized water in a glass dish and heating at 50 °C for 15 minutes while mixing with a glass stir rod. The nickel was etched by gently placing the foil with the PMMA side up on the surface of the room temperature $FeCl_3$ etchant such that it floated. The nickel took approximately 4 hours to etch, after which it was gently transferred to a bath of deionized water by slowly scooping it up with a small petri dish and then lowering the dish into the water. Care was taken to keep the MLG with PMMA film floating on the surface. The process of transferring the film to clean water baths was repeated several times in order to sufficiently dilute the $FeCl_3$.

The MLG was then transferred from the surface of the clean water bath to a 1 cm x 1 cm silicon substrate with an etched rectangular slit. The width of the slit varied from 100 µm to 500 µm, with the length being six times greater than the width. The substrate was held with forceps, gently lowered into the water, and then lifted out of the water while directly below the floating film. If done slowly the film would adhere to the substrate. A long bake step was used to promote better adhesion, drive off the remaining water, and allow the PMMA to flow and smooth some of the wrinkles in the MLG film. In this step, the sample was annealed in atmosphere at 150 °C for 12 hours[84]. The PMMA was then volatized and removed in a 1-inch quartz tube furnace at 350 °C for 3 hours flowing 500 sccm of argon and 500 sccm of hydrogen.

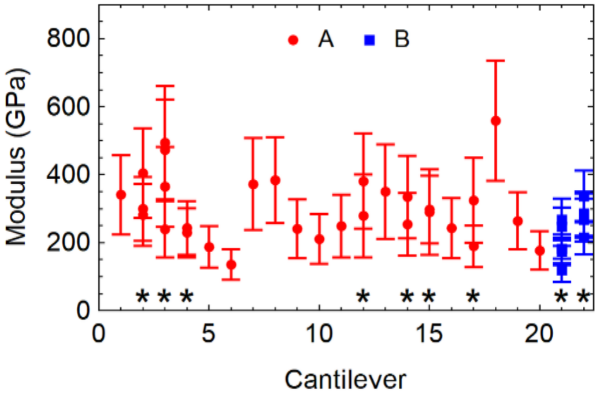

Fig. A-2. Young's modulus for all measured cantilevers. Samples with repeated measurements are marked with an asterisk. The error bars are dominated by thickness uncertainty.

Repeatability of measurements

Seven cantilevers from Sample A and two cantilevers from Sample B were measured multiple times. From Sample A, one cantilever was measured four times, one was measured three times, and the other five were each measured twice. Both cantilevers from Sample B were measured five times. Fig. A-2 shows the results for all measured cantilevers, with cantilevers measured multiple times marked with an asterisk. Measurement error was propagated through to the modulus, with the largest error contribution coming from thickness. Measurement repeatability was characterized by comparing the half-range uncertainty ($[E_{max} - E_{min}]/2$) to the measurement uncertainty. For all cantilevers with repeated measurements (except one from Sample B), the half-range uncertainty was less than the average measurement uncertainty. This means that the variability in repeated measurements was less than that expected from the measurement uncertainty. Repeated measurements of cantilevers typically used different AFM tips (each with their own tip stiffness and tapping mode deflection sensitivity). From this we conclude that the AFM measurement uncertainties were not the dominate uncertainties in these measurements.

Exporting force-volume data

The force-volume data were exported to ASCII text from NanoScope Analysis 2.0 (NA). This multistep process is not well documented and is prone to bugs and limitations of the software. A single force-volume scan was loaded in NA. After ensuring that the deflection sensitivity and spring constant were correct, all of the force curves were selected (by pressing "Select All") and saved (by pressing "Save Curves"). This created one binary file for each force curve in the force-volume scan. For a scan of 64x64 pixels, this was 4096 files. The next step was to convert these exported force curves into ASCII text. Before proceeding, it was necessary to separate the force curve files into directories with no more than 2000 files (a limit of the NA software). The force curves were converted from the binary NanoScope format to a generic ASCII format by using the "Browse Files" tab (on the right hand side) in NA. After navigating to one of the directories containing the force curves, all of the force curves were selected (by pressing CTRL+A). Finally, to export as ASCII it was necessary to right click on the gray background of the "Browse Files" tab and choose "Export > ASCII…", ensuring that "Ramp" was selected under "Force Curve Options" before pressing "Save As…".

Appendix B: Dielectric Properties of Tissue

Conductivity

Conductivity units in S/m:

```
Freq (Hz),Blood,Fat,Muscle,SkinDry,SkinWet,Bone
1.00E+01,7.00E-01,1.22E-02,2.02E-01,2.00E-04,4.02E-04,7.56E-02
1.26E+01,7.00E-01,1.31E-02,2.03E-01,2.00E-04,4.03E-04,7.68E-02
1.59E+01,7.00E-01,1.42E-02,2.05E-01,2.00E-04,4.05E-04,7.80E-02
2.00E+01,7.00E-01,1.55E-02,2.07E-01,2.00E-04,4.07E-04,7.89E-02
2.51E+01,7.00E-01,1.67E-02,2.11E-01,2.00E-04,4.10E-04,7.96E-02
3.16E+01,7.00E-01,1.79E-02,2.17E-01,2.00E-04,4.14E-04,8.01E-02
3.98E+01,7.00E-01,1.88E-02,2.24E-01,2.00E-04,4.20E-04,8.05E-02
5.01E+01,7.00E-01,1.96E-02,2.33E-01,2.00E-04,4.27E-04,8.07E-02
6.31E+01,7.00E-01,2.01E-02,2.44E-01,2.00E-04,4.37E-04,8.09E-02
7.94E+01,7.00E-01,2.05E-02,2.56E-01,2.00E-04,4.48E-04,8.10E-02
1.00E+02,7.00E-01,2.08E-02,2.67E-01,2.00E-04,4.61E-04,8.10E-02
1.26E+02,7.00E-01,2.10E-02,2.76E-01,2.00E-04,4.76E-04,8.11E-02
1.59E+02,7.00E-01,2.12E-02,2.85E-01,2.00E-04,4.92E-04,8.11E-02
2.00E+02,7.00E-01,2.13E-02,2.91E-01,2.00E-04,5.10E-04,8.11E-02
2.51E+02,7.00E-01,2.14E-02,2.96E-01,2.00E-04,5.28E-04,8.12E-02
3.16E+02,7.00E-01,2.15E-02,3.01E-01,2.00E-04,5.46E-04,8.12E-02
3.98E+02,7.00E-01,2.17E-02,3.06E-01,2.00E-04,5.65E-04,8.13E-02
5.01E+02,7.00E-01,2.18E-02,3.10E-01,2.00E-04,5.85E-04,8.13E-02
6.31E+02,7.00E-01,2.20E-02,3.14E-01,2.00E-04,6.07E-04,8.14E-02
7.94E+02,7.00E-01,2.22E-02,3.18E-01,2.00E-04,6.30E-04,8.14E-02
1.00E+03,7.00E-01,2.24E-02,3.21E-01,2.00E-04,6.57E-04,8.15E-02
1.26E+03,7.00E-01,2.26E-02,3.24E-01,2.00E-04,6.91E-04,8.16E-02
1.59E+03,7.00E-01,2.29E-02,3.27E-01,2.00E-04,7.33E-04,8.17E-02
2.00E+03,7.00E-01,2.31E-02,3.30E-01,2.00E-04,7.89E-04,8.19E-02
2.51E+03,7.00E-01,2.32E-02,3.32E-01,2.00E-04,8.67E-04,8.20E-02
3.16E+03,7.00E-01,2.34E-02,3.34E-01,2.01E-04,9.76E-04,8.21E-02
3.98E+03,7.00E-01,2.35E-02,3.35E-01,2.01E-04,1.13E-03,8.22E-02
5.01E+03,7.00E-01,2.36E-02,3.37E-01,2.01E-04,1.36E-03,8.23E-02
6.31E+03,7.00E-01,2.37E-02,3.38E-01,2.02E-04,1.70E-03,8.24E-02
7.94E+03,7.00E-01,2.38E-02,3.40E-01,2.03E-04,2.20E-03,8.25E-02
1.00E+04,7.00E-01,2.38E-02,3.41E-01,2.04E-04,2.93E-03,8.26E-02
1.26E+04,7.00E-01,2.39E-02,3.42E-01,2.06E-04,4.01E-03,8.27E-02
1.59E+04,7.00E-01,2.40E-02,3.44E-01,2.09E-04,5.57E-03,8.28E-02
2.00E+04,7.00E-01,2.40E-02,3.45E-01,2.14E-04,7.83E-03,8.29E-02
2.51E+04,7.00E-01,2.41E-02,3.46E-01,2.21E-04,1.10E-02,8.31E-02
3.16E+04,7.00E-01,2.41E-02,3.48E-01,2.32E-04,1.55E-02,8.32E-02
3.98E+04,7.01E-01,2.42E-02,3.50E-01,2.49E-04,2.15E-02,8.33E-02
5.01E+04,7.01E-01,2.43E-02,3.52E-01,2.73E-04,2.95E-02,8.34E-02
6.31E+04,7.01E-01,2.43E-02,3.54E-01,3.11E-04,3.95E-02,8.36E-02
7.94E+04,7.02E-01,2.44E-02,3.58E-01,3.67E-04,5.17E-02,8.37E-02
1.00E+05,7.03E-01,2.44E-02,3.62E-01,4.51E-04,6.58E-02,8.39E-02
1.26E+05,7.05E-01,2.45E-02,3.67E-01,5.78E-04,8.15E-02,8.41E-02
1.59E+05,7.07E-01,2.45E-02,3.75E-01,7.68E-04,9.80E-02,8.43E-02
2.00E+05,7.10E-01,2.46E-02,3.84E-01,1.05E-03,1.15E-01,8.46E-02
2.51E+05,7.16E-01,2.46E-02,3.96E-01,1.47E-03,1.32E-01,8.50E-02
3.16E+05,7.23E-01,2.47E-02,4.11E-01,2.10E-03,1.48E-01,8.54E-02
3.98E+05,7.34E-01,2.48E-02,4.27E-01,3.03E-03,1.63E-01,8.60E-02
5.01E+05,7.48E-01,2.48E-02,4.46E-01,4.38E-03,1.78E-01,8.67E-02
6.31E+05,7.68E-01,2.49E-02,4.66E-01,6.36E-03,1.93E-01,8.77E-02
7.94E+05,7.93E-01,2.50E-02,4.85E-01,9.20E-03,2.07E-01,8.89E-02
1.00E+06,8.22E-01,2.51E-02,5.03E-01,1.32E-02,2.21E-01,9.04E-02
1.26E+06,8.55E-01,2.52E-02,5.19E-01,1.89E-02,2.36E-01,9.23E-02
1.59E+06,8.91E-01,2.53E-02,5.34E-01,2.66E-02,2.51E-01,9.45E-02
2.00E+06,9.26E-01,2.55E-02,5.48E-01,3.70E-02,2.66E-01,9.71E-02
2.51E+06,9.59E-01,2.57E-02,5.60E-01,5.04E-02,2.82E-01,1.00E-01
3.16E+06,9.89E-01,2.60E-02,5.71E-01,6.73E-02,2.97E-01,1.03E-01
3.98E+06,1.02E+00,2.64E-02,5.81E-01,8.78E-02,3.11E-01,1.07E-01
5.01E+06,1.04E+00,2.69E-02,5.90E-01,1.12E-01,3.25E-01,1.11E-01
6.31E+06,1.06E+00,2.76E-02,5.99E-01,1.38E-01,3.39E-01,1.15E-01
```

```
7.94E+06,1.08E+00,2.83E-02,6.08E-01,1.67E-01,3.52E-01,1.19E-01
1.00E+07,1.10E+00,2.92E-02,6.17E-01,1.97E-01,3.66E-01,1.23E-01
1.26E+07,1.11E+00,3.01E-02,6.25E-01,2.28E-01,3.80E-01,1.27E-01
1.59E+07,1.13E+00,3.10E-02,6.34E-01,2.59E-01,3.94E-01,1.31E-01
2.00E+07,1.14E+00,3.19E-02,6.43E-01,2.89E-01,4.08E-01,1.36E-01
2.51E+07,1.15E+00,3.27E-02,6.51E-01,3.19E-01,4.23E-01,1.40E-01
3.16E+07,1.17E+00,3.34E-02,6.60E-01,3.48E-01,4.38E-01,1.45E-01
3.98E+07,1.18E+00,3.41E-02,6.69E-01,3.77E-01,4.54E-01,1.50E-01
5.01E+07,1.19E+00,3.47E-02,6.78E-01,4.06E-01,4.70E-01,1.55E-01
6.31E+07,1.21E+00,3.52E-02,6.88E-01,4.34E-01,4.87E-01,1.61E-01
7.94E+07,1.22E+00,3.58E-02,6.97E-01,4.63E-01,5.05E-01,1.66E-01
1.00E+08,1.23E+00,3.63E-02,7.08E-01,4.91E-01,5.23E-01,1.73E-01
1.26E+08,1.25E+00,3.68E-02,7.18E-01,5.21E-01,5.43E-01,1.79E-01
1.59E+08,1.26E+00,3.74E-02,7.30E-01,5.51E-01,5.64E-01,1.87E-01
2.00E+08,1.28E+00,3.81E-02,7.43E-01,5.82E-01,5.86E-01,1.96E-01
2.51E+08,1.30E+00,3.88E-02,7.58E-01,6.15E-01,6.10E-01,2.06E-01
3.16E+08,1.32E+00,3.98E-02,7.75E-01,6.50E-01,6.37E-01,2.19E-01
3.98E+08,1.35E+00,4.11E-02,7.96E-01,6.87E-01,6.68E-01,2.34E-01
5.01E+08,1.38E+00,4.28E-02,8.23E-01,7.29E-01,7.05E-01,2.54E-01
6.31E+08,1.43E+00,4.52E-02,8.59E-01,7.76E-01,7.50E-01,2.81E-01
7.94E+08,1.49E+00,4.86E-02,9.08E-01,8.32E-01,8.07E-01,3.16E-01
1.00E+09,1.58E+00,5.35E-02,9.78E-01,9.00E-01,8.82E-01,3.64E-01
1.26E+09,1.71E+00,6.06E-02,1.08E+00,9.87E-01,9.84E-01,4.31E-01
1.59E+09,1.90E+00,7.08E-02,1.23E+00,1.10E+00,1.13E+00,5.23E-01
2.00E+09,2.18E+00,8.57E-02,1.45E+00,1.26E+00,1.33E+00,6.51E-01
2.51E+09,2.60E+00,1.07E-01,1.78E+00,1.49E+00,1.63E+00,8.27E-01
3.16E+09,3.21E+00,1.38E-01,2.27E+00,1.83E+00,2.06E+00,1.07E+00
3.98E+09,4.11E+00,1.82E-01,3.00E+00,2.33E+00,2.69E+00,1.39E+00
5.01E+09,5.41E+00,2.43E-01,4.06E+00,3.07E+00,3.59E+00,1.82E+00
6.31E+09,7.25E+00,3.27E-01,5.58E+00,4.17E+00,4.86E+00,2.36E+00
7.94E+09,9.78E+00,4.39E-01,7.72E+00,5.77E+00,6.61E+00,3.04E+00
1.00E+10,1.31E+01,5.85E-01,1.06E+01,8.01E+00,8.95E+00,3.86E+00
```

Relative Permittivity

```
Freq (Hz),Blood,Fat,Muscle,SkinDry,SkinWet,Bone
1.00E+01,5.26E+03,7.97E+06,2.57E+07,1.14E+03,5.83E+04,1.00E+07
1.26E+01,5.26E+03,7.15E+06,2.54E+07,1.14E+03,5.78E+04,7.76E+06
1.59E+01,5.26E+03,6.15E+06,2.50E+07,1.14E+03,5.72E+04,5.72E+06
2.00E+01,5.26E+03,5.04E+06,2.43E+07,1.14E+03,5.64E+04,4.04E+06
2.51E+01,5.26E+03,3.94E+06,2.33E+07,1.14E+03,5.55E+04,2.76E+06
3.16E+01,5.26E+03,2.94E+06,2.20E+07,1.14E+03,5.43E+04,1.84E+06
3.98E+01,5.26E+03,2.11E+06,2.01E+07,1.14E+03,5.29E+04,1.21E+06
5.01E+01,5.26E+03,1.47E+06,1.77E+07,1.14E+03,5.13E+04,7.85E+05
6.31E+01,5.26E+03,1.00E+06,1.49E+07,1.14E+03,4.94E+04,5.10E+05
7.94E+01,5.26E+03,6.77E+05,1.21E+07,1.14E+03,4.74E+04,3.31E+05
1.00E+02,5.26E+03,4.57E+05,9.33E+06,1.14E+03,4.53E+04,2.17E+05
1.26E+02,5.26E+03,3.11E+05,6.98E+06,1.14E+03,4.32E+04,1.44E+05
1.59E+02,5.26E+03,2.14E+05,5.11E+06,1.14E+03,4.12E+04,9.76E+04
2.00E+02,5.26E+03,1.51E+05,3.71E+06,1.14E+03,3.93E+04,6.79E+04
2.51E+02,5.26E+03,1.09E+05,2.70E+06,1.14E+03,3.77E+04,4.87E+04
3.16E+02,5.26E+03,8.13E+04,1.98E+06,1.14E+03,3.63E+04,3.63E+04
3.98E+02,5.26E+03,6.23E+04,1.46E+06,1.14E+03,3.51E+04,2.80E+04
5.01E+02,5.26E+03,4.88E+04,1.08E+06,1.14E+03,3.41E+04,2.23E+04
6.31E+02,5.26E+03,3.87E+04,8.04E+05,1.14E+03,3.33E+04,1.81E+04
7.94E+02,5.26E+03,3.07E+04,5.93E+05,1.14E+03,3.27E+04,1.49E+04
1.00E+03,5.26E+03,2.41E+04,4.35E+05,1.14E+03,3.21E+04,1.23E+04
1.26E+03,5.26E+03,1.86E+04,3.18E+05,1.14E+03,3.17E+04,1.02E+04
1.59E+03,5.26E+03,1.40E+04,2.31E+05,1.14E+03,3.13E+04,8.38E+03
2.00E+03,5.26E+03,1.03E+04,1.69E+05,1.14E+03,3.10E+04,6.86E+03
2.51E+03,5.26E+03,7.53E+03,1.24E+05,1.14E+03,3.08E+04,5.58E+03
3.16E+03,5.26E+03,5.43E+03,9.15E+04,1.14E+03,3.05E+04,4.53E+03
3.98E+03,5.26E+03,3.90E+03,6.86E+04,1.14E+03,3.03E+04,3.67E+03
5.01E+03,5.25E+03,2.81E+03,5.22E+04,1.14E+03,3.00E+04,2.98E+03
6.31E+03,5.25E+03,2.03E+03,4.05E+04,1.13E+03,2.97E+04,2.43E+03
7.94E+03,5.25E+03,1.48E+03,3.21E+04,1.13E+03,2.94E+04,2.00E+03
1.00E+04,5.25E+03,1.09E+03,2.59E+04,1.13E+03,2.90E+04,1.66E+03
1.26E+04,5.25E+03,8.06E+02,2.14E+04,1.13E+03,2.85E+04,1.39E+03
1.59E+04,5.24E+03,6.05E+02,1.81E+04,1.13E+03,2.79E+04,1.18E+03
```

```
2.00E+04,5.24E+03,4.60E+02,1.55E+04,1.13E+03,2.72E+04,1.01E+03
2.51E+04,5.23E+03,3.54E+02,1.36E+04,1.13E+03,2.62E+04,8.74E+02
3.16E+04,5.22E+03,2.75E+02,1.22E+04,1.13E+03,2.50E+04,7.67E+02
3.98E+04,5.21E+03,2.16E+02,1.10E+04,1.13E+03,2.36E+04,6.82E+02
5.01E+04,5.20E+03,1.72E+02,1.01E+04,1.13E+03,2.19E+04,6.13E+02
6.31E+04,5.18E+03,1.38E+02,9.32E+03,1.13E+03,1.99E+04,5.56E+02
7.94E+04,5.15E+03,1.13E+02,8.67E+03,1.12E+03,1.77E+04,5.10E+02
1.00E+05,5.12E+03,9.29E+01,8.09E+03,1.12E+03,1.54E+04,4.72E+02
1.26E+05,5.07E+03,7.75E+01,7.53E+03,1.12E+03,1.31E+04,4.39E+02
1.59E+05,5.01E+03,6.55E+01,6.97E+03,1.11E+03,1.09E+04,4.12E+02
2.00E+05,4.93E+03,5.61E+01,6.38E+03,1.11E+03,8.87E+03,3.88E+02
2.51E+05,4.81E+03,4.87E+01,5.75E+03,1.10E+03,7.15E+03,3.66E+02
3.16E+05,4.66E+03,4.29E+01,5.07E+03,1.09E+03,5.71E+03,3.46E+02
3.98E+05,4.45E+03,3.82E+01,4.35E+03,1.08E+03,4.54E+03,3.27E+02
5.01E+05,4.19E+03,3.45E+01,3.64E+03,1.06E+03,3.60E+03,3.08E+02
6.31E+05,3.86E+03,3.16E+01,2.96E+03,1.04E+03,2.87E+03,2.89E+02
7.94E+05,3.47E+03,2.92E+01,2.35E+03,1.02E+03,2.29E+03,2.69E+02
1.00E+06,3.03E+03,2.72E+01,1.84E+03,9.91E+02,1.83E+03,2.49E+02
1.26E+06,2.56E+03,2.56E+01,1.42E+03,9.55E+02,1.47E+03,2.28E+02
1.59E+06,2.11E+03,2.42E+01,1.08E+03,9.11E+02,1.18E+03,2.07E+02
2.00E+06,1.69E+03,2.30E+01,8.28E+02,8.59E+02,9.51E+02,1.85E+02
2.51E+06,1.32E+03,2.18E+01,6.36E+02,7.98E+02,7.62E+02,1.64E+02
3.16E+06,1.02E+03,2.07E+01,4.93E+02,7.29E+02,6.11E+02,1.44E+02
3.98E+06,7.78E+02,1.95E+01,3.87E+02,6.55E+02,4.91E+02,1.25E+02
5.01E+06,5.95E+02,1.82E+01,3.08E+02,5.78E+02,3.97E+02,1.09E+02
6.31E+06,4.57E+02,1.68E+01,2.49E+02,5.02E+02,3.24E+02,9.41E+01
7.94E+06,3.55E+02,1.53E+01,2.04E+02,4.29E+02,2.66E+02,8.15E+01
1.00E+07,2.80E+02,1.38E+01,1.71E+02,3.62E+02,2.22E+02,7.08E+01
1.26E+07,2.25E+02,1.23E+01,1.45E+02,3.03E+02,1.87E+02,6.19E+01
1.59E+07,1.85E+02,1.09E+01,1.26E+02,2.52E+02,1.59E+02,5.45E+01
2.00E+07,1.55E+02,9.73E+00,1.11E+02,2.10E+02,1.37E+02,4.84E+01
2.51E+07,1.33E+02,8.74E+00,9.91E+01,1.75E+02,1.20E+02,4.34E+01
3.16E+07,1.16E+02,7.95E+00,8.99E+01,1.47E+02,1.05E+02,3.93E+01
3.98E+07,1.04E+02,7.34E+00,8.27E+01,1.25E+02,9.39E+01,3.60E+01
5.01E+07,9.41E+01,6.87E+00,7.70E+01,1.07E+02,8.47E+01,3.32E+01
6.31E+07,8.68E+01,6.53E+00,7.25E+01,9.29E+01,7.71E+01,3.10E+01
7.94E+07,8.12E+01,6.27E+00,6.89E+01,8.18E+01,7.10E+01,2.92E+01
1.00E+08,7.68E+01,6.07E+00,6.60E+01,7.29E+01,6.60E+01,2.76E+01
1.26E+08,7.34E+01,5.93E+00,6.36E+01,6.59E+01,6.19E+01,2.64E+01
1.59E+08,7.07E+01,5.82E+00,6.18E+01,6.03E+01,5.85E+01,2.53E+01
2.00E+08,6.85E+01,5.74E+00,6.02E+01,5.58E+01,5.57E+01,2.44E+01
2.51E+08,6.68E+01,5.68E+00,5.90E+01,5.21E+01,5.34E+01,2.37E+01
3.16E+08,6.54E+01,5.62E+00,5.80E+01,4.92E+01,5.15E+01,2.30E+01
3.98E+08,6.42E+01,5.58E+00,5.71E+01,4.68E+01,4.99E+01,2.25E+01
5.01E+08,6.33E+01,5.54E+00,5.64E+01,4.49E+01,4.86E+01,2.20E+01
6.31E+08,6.24E+01,5.51E+00,5.58E+01,4.33E+01,4.75E+01,2.15E+01
7.94E+08,6.17E+01,5.48E+00,5.53E+01,4.20E+01,4.66E+01,2.10E+01
1.00E+09,6.11E+01,5.45E+00,5.48E+01,4.09E+01,4.57E+01,2.06E+01
1.26E+09,6.04E+01,5.41E+00,5.43E+01,4.00E+01,4.50E+01,2.01E+01
1.59E+09,5.98E+01,5.37E+00,5.38E+01,3.93E+01,4.42E+01,1.96E+01
2.00E+09,5.90E+01,5.33E+00,5.33E+01,3.86E+01,4.35E+01,1.91E+01
2.51E+09,5.82E+01,5.27E+00,5.27E+01,3.79E+01,4.28E+01,1.85E+01
3.16E+09,5.71E+01,5.21E+00,5.19E+01,3.73E+01,4.19E+01,1.78E+01
3.98E+09,5.57E+01,5.13E+00,5.08E+01,3.66E+01,4.09E+01,1.70E+01
5.01E+09,5.39E+01,5.03E+00,4.95E+01,3.58E+01,3.96E+01,1.60E+01
6.31E+09,5.16E+01,4.91E+00,4.78E+01,3.47E+01,3.80E+01,1.50E+01
7.94E+09,4.87E+01,4.77E+00,4.56E+01,3.32E+01,3.60E+01,1.39E+01
1.00E+10,4.51E+01,4.60E+00,4.28E+01,3.13E+01,3.35E+01,1.27E+01
```

Appendix C: Software

X-ray Window Transmission and Optimization

https://github.com/larsenkg/xray_window

With this software it is possible to model the transmission of x-ray windows consisting of multiple layers. Optimizations can be performed on the x-ray window models to find which parameters (e.g. support spacing, support width, film thickness, etc.) give the highest transmission at one or more energies.

Multipoint Force-Deflection Analysis

https://github.com/larsenkg/pyMFD

This software, pyMFD, can be used to read AFM force-volume data (from a NanoScope v7.2 file format), summarize the 3-D data into a 2-D compliance map, and analyze microcantilever compliance data. The software is written in an extensible way, so that support for other file formats can be added in the future.

Appendix D: Bioimpedance Instrumentation

Multiplexer

A printed circuit board was designed to connect the microcontroller, both multiplexers, the impedance analyzer, and the electrode arrays. It also contained other necessary components such as reverse current protection diodes, voltage regulators, current limiting resistors and decoupling capacitors to prevent high amplitude currents and DC currents from going into the body. A wireless-capable microcontroller (Espressif ESP-01) was selected to minimize the number of wired connections between the subject and the PC. This simplified the subject safety compliance and helped reduce noise, since wired serial communication often happens in our band of interest (1 kHz to 5 MHz). The ESP-01 controls the two multiplexers over I2C. We call this board the MUX board. A simplified schematic of the MUX Board connected to the impedance analyzer is shown in Fig. D-1 and the actual MUX board is shown in Fig. D-2.

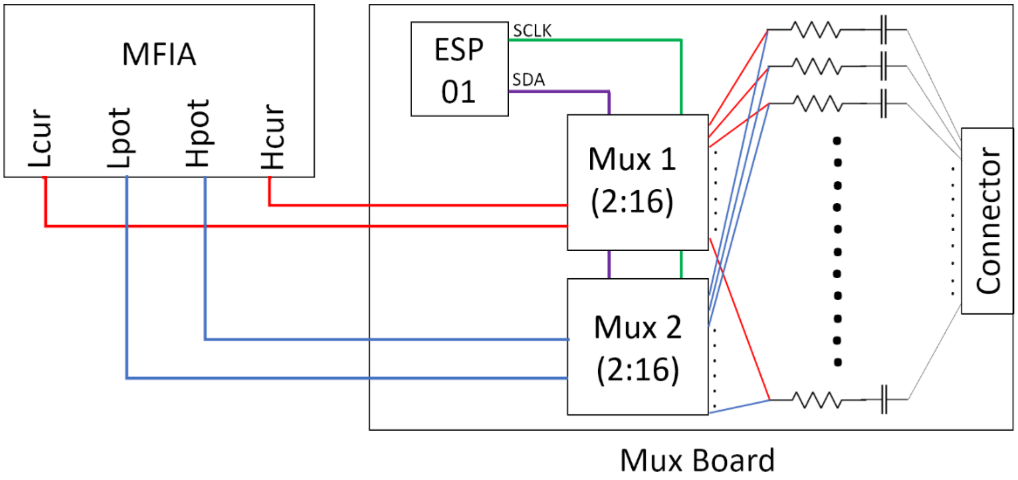

Fig. D-1. Simplified schematic of the multiplexer board.

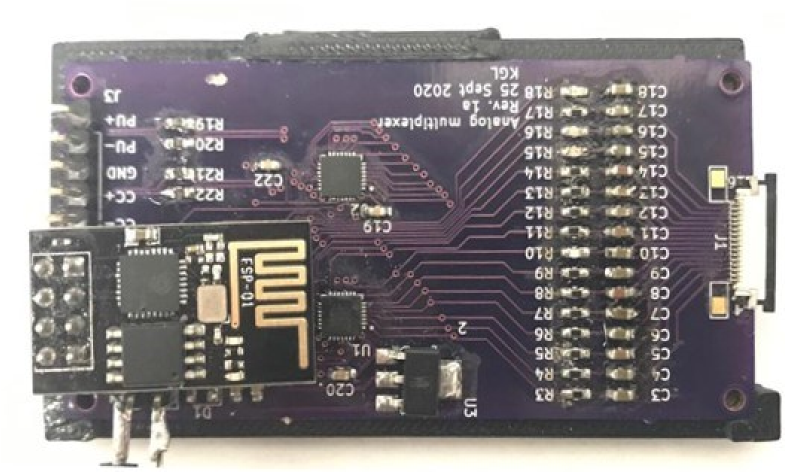

Fig. D-2. Photograph of the multiplexer board.

Electrode Array Holder

The design of electrode array holder (EAH) consists of a rectangular area of the same size as the flexible printed circuit board (FPCB) electrode array with the largest electrodes (2 mm x 16 mm). A reference corner was added to the rectangular area so that when attaching the other two smaller FPCB arrays, the center of the arrays would always line up with the center of the rectangular area. The profile of the pressure sensors were cut into the rectangular area so that the pressure sensors would fit tightly inside (see Fig. D-3c). The cut out for both sensors lined up with the respective center of either electrode array. Pucks that had a loose fit with the circular cut out for the sensor were used to secure the sensor in place and to make sure the sensors uniformly experienced the applied force. On the other side of the cut out face, the housing secured the pressure sensor interface board (see Fig. D-3b for the interface board and Fig. D-3d for the housing design). Housing for keeping the sensor leads from moving was designed as a separate part that would attach to the side of the interface board housing (see Fig. D-3e). On the same side of the interface board housing, there is a conical post in the center of the rectangular area and ends in a rounded point (see Fig. D-3d). This post serves as a fulcrum between the two rows of electrodes. A 2.4 mm thick sheet of polydimethylsiloxane (PDMS; silicone) was placed between the pressure sensors and the FPCB. The purpose of the silicone layer is to help distribute the pressure forces applied to the pucks, since the pucks raise a little from surface of the rectangular area. See Fig. D-4 for the final assembly of the EAH.

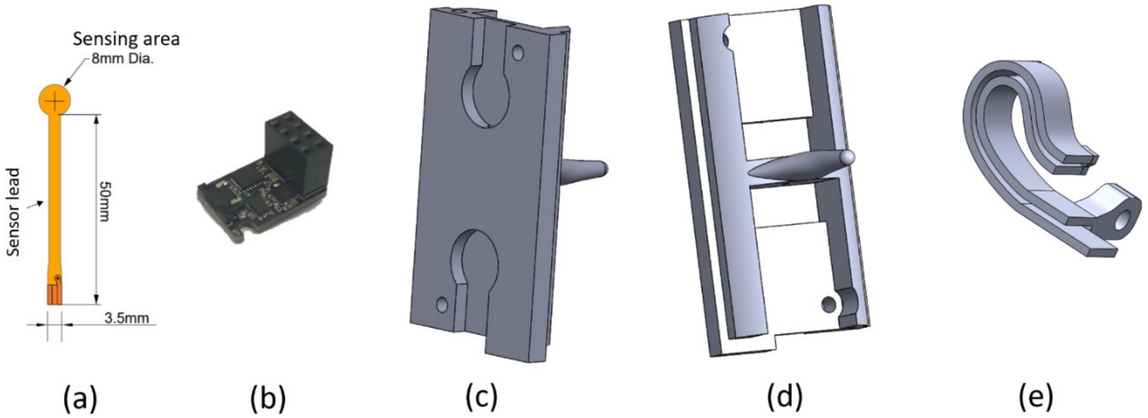

Fig. D-3. The electrode array holder components. (a) SingleTact pressure sensor. (b) Pressure sensor interface board. (c) View of EAH showing cut outs for pressure sensors. (d) View of EAH showing where the interface board sits and the post. (e) Housing for the pressure sensor leads.

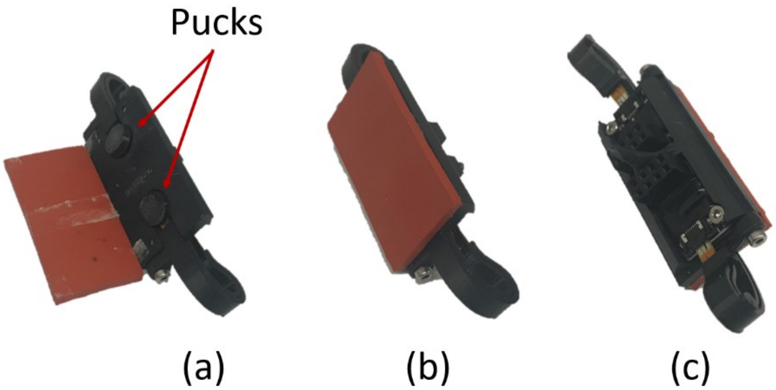

Fig. D-4. Assembled electrode array holder with silicone sheet. (a) Pucks attached to the pressure sensor serve as a rigid surface to keep the sensing part from bending and help transfer the applied forces directly to the sensor. (b) Silicone attached to the EAH. (c) Final assembly of the EAH.

Wristband

The band is designed as a watch band with a ratcheting tightening mechanism. On the outer face of the band there is a rack-like section on which the ratchet buckle locks as the band tightens (see top of Fig. D-5). On the inner face of the band there are "dimples" that fit the rounded point of the EAH post (see bottom of Fig. D-5). The dimples serve as pivot points for the EAH post. The EAH post fits into one of the band dimples, and as the band tightens the EAH gets pressed into the wrist. The pivot point allows for the EAH to rotate about that point so that when there is movement, such as flexion of the wrist, the EAH can remain parallel to the wrist instead of having one side of the EAH digging more into the wrist than the other side. This allows for approximately equal pressures on both the wet and dry electrode arrays. Fig. 5-5 illustrates the overall measurement system setup for this study.

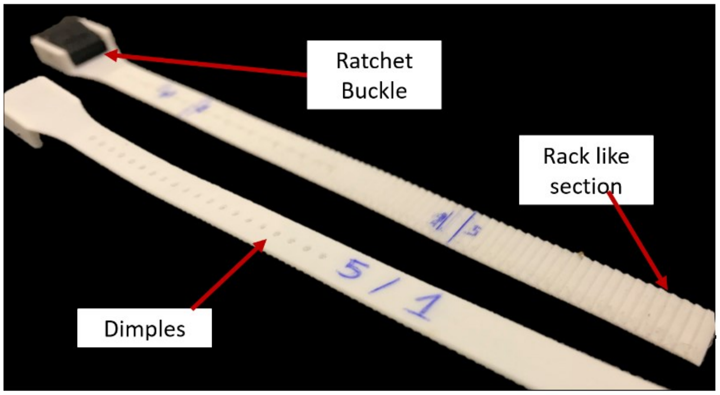

Fig. D-5. Wristband for securing electrodes to wrist. Top: Outer face of band showing the rack like section of the band. Bottom: Inner face of band showing the dimples into which the post of the EAH fits.